DOCTORAL THESIS NO. 30

Study on the Earth's Surface Mass Variations using Satellite Gravimetry Observations

Hadi Amin

Gävle University Press

Dissertation for the Degree of Doctor of Philosophy in Geospatial Information Science to be publicly defended on Friday, 23rd September 2022 at 10:00 in 13:111, University of Gävle.

External reviewer: Professor Martin Horwath, Dresden University of Technology

Cover illustration: My NASA Data (https://mynasadata.larc.nasa.gov/)

Gävle University Press
ISBN 978-91-88145-91-8
ISBN 978-91-88145-92-5 (pdf)
urn:nbn:se:hig:diva-39412

Distribution:
University of Gävle
Faculty of Engineering and Sustainable Development
Department of Computer and Geospatial Sciences
SE-801 76 Gävle, Sweden
+46 26 64 85 00
www.hig.se

To my family

Abstract

Our complex planet is continuously undergoing temporal and spatial changes. In this context, ongoing processes in the Earth subsystems (geosphere, biosphere, cryosphere, hydrosphere, and atmosphere) cause changes in the gravity field of the Earth across a wide range of temporal and spatial scales. Accordingly, by both spatially and temporally tracing our planet's ever-changing gravity field, scientists can better constrain the underlying processes contributing to such dynamic changes of mass distribution within the Earth system.

Monitoring the Earth's gravity field and its temporal variations is essential, among others, for tracking disasters and specifying land areas with a high risk of flooding, earthquakes, and droughts, movements of tectonic plates, and providing accurate positioning through satellite positioning technology. On short-term timescales, temporal variations in the Earth's gravity field are mainly caused by the movement of water in its various forms. Accordingly, sea-level variations and ice-sheet and glacier changes, which are known as critical indicators of global warming and climate change, can be accurately monitored by tracking the Earth's gravity field changes. Since there is a close link between water redistribution and the Earth's energy cycle, climate system, food security, human and ecosystem health, energy generation, economic and societal development, and climate extremes (droughts and floods), it is essential to accurately monitor water mass exchange between the Earth system components.

Among all observational techniques, satellite gravimetry has provided an integrated global view of ongoing processes within the Earth system. The current generation of satellite gravimetry missions (the Gravity Recovery and Climate Experiment (GRACE) mission and its successor, GRACE Follow-On) has dramatically revolutionized our understanding of dynamic processes in the Earth's surface and, consequently, has significantly improved our understanding of the Earth's climate system. By considering different aspects of studying the Earth's gravity field, this thesis brings new insights to the determination and analysis of the mass change in the Earth system.

First, by studying the shortcomings of the common techniques of estimating the geoid potential, a new approach is examined that simultaneously estimates the geoid potential, W_0, and the geometrical parameters of the reference Mean Earth Ellipsoid (MEE). In this regard, as the geoid needs to be considered as a static equipotential surface, the sensitivity of the estimations to the time-dependent Earth's gravity field changes is studied.

Secondly, relying on the GRACE monthly gravity fields and the

complementary observational techniques, and by pushing the limit of GRACE, mass redistribution over land and ocean is investigated. Within the ocean, satellite altimetry and Argo products are utilized along with the GRACE monthly solutions for quantifying the global barystatic sea-level change and assessing the closure of the global mean sea level budget. Over land, a region with relatively high temporal mass change (oil and water extraction) is chosen in which by taking advantage of having in-situ observations and hydrological models, the ability of GRACE products in quantifying the changes in groundwater storage is studied. In this frame, for both the ocean and land studies, different aspects of the processing of GRACE monthly gravity fields are investigated and GRACE inherent errors are addressed appropriately to arrive at reliable and accurate estimates of the Earth's surface mass change.

As the final contribution in this thesis, a rigorous analytical model for detecting surface mass change from the time-variable gravity solutions is proposed and examined in different case studies of surface mass change. Since the launch of the GRACE twin satellites, the GRACE(-FO) time-varying gravity fields are conventionally converted into the surface mass change using a spherical analytical model that approximates the Earth by a sphere. More recently, the analytical mass change detection model has been improved by considering an ellipsoid as the shape of the Earth, which improved the previous estimations of surface mass change, especially over high latitudes with relatively large mass change signals. However, by taking into account the real shape of the Earth and considering more realistic assumptions, a new analytical solution for the problem of surface mass change detection from the time-varying gravity fields is proposed in this thesis. It is shown that the simplistic spherical and ellipsoidal geometries are no longer tenable and the new model surpasses the common spherical approach and its ellipsoidal version.

Keywords: geodetic reference system, geoid potential, global vertical datum, climate change, global warming, mass change, ice melting, sea-level change, remote sensing, satellite gravimetry

Sammanfattning

Pågående processer i jordens olika delar (geosfären, biosfären, kryosfären, hydrosfären och atmosfären) orsakar massförändringar som bland annat ger sig till känna i form av variationer i jordens tyngdkrafts-/gravitationsfält över ett brett spektrum av tidsmässiga och rumsliga skalor. Följaktligen, genom att studera detta ständigt föränderliga fält i tid och rum, kan forskare utröna de underliggande orsakerna till de dynamiska förändringarna av massfördelningarna i dessa processer.

Övervakning av jordens gravitationsfält och dess tidsmässiga variationer är nödvändig bland annat för att spåra katastrofer och specificera landområden med hög risk för översvämningar, jordbävningar och torka, rörelser av tektoniska plattor och tillhandahålla exakt positionering genom satellitpositioneringsteknik. På kortsiktiga tidsskalor orsakas tidsmässiga variationer i jordens gravitationsfält främst av vattenrörelser i dess olika former. Följaktligen kan havsnivå-, istäcke- och glaciärförändringar, som är kända som kritiska indikatorer på global uppvärmning och klimatförändringar, övervakas exakt genom övervakning av tyngdkraftfältets förändringar. Eftersom det finns en intim koppling mellan omfördelningen av jordens vattenmassor och energicykel, klimatsystem, livsmedelssäkerhet, människors och ekosystems hälsa, energiproduktion, ekonomisk och samhällelig utveckling och extremer i klimatet (torka och översvämningar), är det viktigt att noggrant övervaka vattnets massutbyte mellan jordsystemets olika komponenter.

Bland alla observationstekniker ger satellitgravimetri en global integrerad översikt av pågående massförändringar. De nuvarande satellitsystemen, dedikerade för gravimetri-uppdrag (Gravity Recovery and Climate Experiment (GRACE) satellitprojektet och dess efterträdare, GRACE Follow-On), har dramatiskt revolutionerat vår förståelse av de dynamiska processerna på jordytan, och de har följaktligen avsevärt förbättrat vår förståelse av jordens klimatsystem. Genom att pröva olika aspekter av att studera jordens gravitationsfält ger denna avhandling nya möjligheter att studera jordsystemets massvariationer.

Först, genom att studera bristerna i de vanliga teknikerna för att uppskatta ett potentialvärde för geoiden, undersöks ett nytt tillvägagångssätt som samtidigt uppskattar ett värde på geopotentialen, W0, och de geometriska parametrarna för en global referensellipsoid (Mean Earth Ellipsoid,MEE). Eftersom geoiden i detta sammanhang måste betraktas som en statisk ekvipotentialyta, så beräknar vi även noggranheten hos uppskattningarna för de tidsberoende förändringar av jordens gravitationsfält.

För det andra, att förlita sig på GRACE månatliga gravitationsfält och de kompletterande observationsteknikerna, och genom att tänja på gränsen för GRACE, undersöks massutbytet mellan land och hav. I havsområden används satellitaltimetri- och Argo-data tillsammans med GRACE månatliga gravitationsfält för att kvantifiera den globala havsnivåförändringen och bedöma slutningsfelet i den globala medelhavsnivå-budgeten. I en annan studie väljer vi en region på land med relativt stor massförändring i tiden p.g.a. olje- och vattenutvinning, där vi drar fördel av in-situ observationer och hydrologiska modeller, för att analysera förmågan hos GRACE att kvantifiera förändringar i grundvattennivån. För både havs- och landstudierna undersöks olika aspekter att bearbeta GRACE månatliga data , samt lämpliga åtgärder att korrigera fel för att ernå tillförlitliga och noggranna uppskattningar av massförändringar vid jordytan.

Som det sista bidraget i denna avhandling föreslås en rigorös analytisk modell för detektering av massförändringarna i tiden, som undersöks i olika fallstudier av massförändringar. Data från GRACE(-FO) som varierar i tiden omvandlas konventionellt till ytmass-förändringar med hjälp av en sfärisk analytisk modell, som approximerar jorden med en sfär. Nyligen har den analytiska modellen för detektering av massförändringar förbättrats genom att approximera jordens form med en ellipsoid, vilket förbättrade de tidigare uppskattningarna av massförändringar, särskilt för höga latituder med relativt stora massförändringar. Men genom att gå ännu längre och ta hänsyn till jordens verkliga form och överväga mer realistiska antaganden, föreslås i denna avhandling en ny analytisk lösning för problemet. Det har visat sig att de förenklade sfäriska och ellipsoida geometrierna inte längre är försvarbara och den nya modellen överträffar det vanliga sfäriska tillvägagångssättet och dess ellipsoida version.

Nyckelord: geodetiska referenssystem, geopotential, globala vertikala datum, klimatförändring, global uppvärmning, massförändring, issmältning, havsnivåförändring, fjärranalys, satellitgravimetri

Acknowledgments

During the past five years, I have learned a lot and been inspired and supported by many great people. This thesis would have never seen the light without their support and guidance, to all of whom I would like to express my gratitude in the coming few lines.

First of all, I would like to express my sincere gratitude to my supervisors Prof. Mohammad Bagherbandi, Prof. Lars E. Sjöberg, and Dr. Faramarz Nilfouroushan for their continuous support, encouragement, and constructive criticism throughout this journey. I am so grateful to you for always believing in me, for allowing me to pursue the topic that I was passionate about, and for constantly providing wise observations and guidance. Thank you for pushing me to my limits, while always having the door open for me. You gave me the freedom to create my own path, yet ensuring that I am never lost. I truly appreciate all your support and advice.

I would like to extend my deep gratitude to a person who unconditionally provided his support during my PhD journey, Dr. Jonas Boustedt, head of the Department of Computer and Geospatial Sciences at the University of Gävle. Dear Jonas, I am very grateful to you for all the discussions and encouragement, and for your mental and financial support that made me never have to worry about attending a conference or a school. Thank you for helping me out with my personal life that made my stay in Gävle more pleasant. I would also like to thank Prof. Stefan Seipel, the responsible for the scientific discipline within the subject Geospatial Information Science, for his support.

Aside from the official supervision team, I have additionally benefited from support and guidance from external co-authors and colleagues who have shaped my way of thinking and from whom I have learned a great deal. I would like to thank Dr. Yahya AllahTavakoli and Dr. Hamidreza Bagheri for their insightful discussions, encouragement, and support. Your knowledge, genius, and hard-work have always inspired me, and it was a great pleasure for me to collaborate with you. I am thankful to Dr. Nureldin Gido for the valuable discussions and support. I would further like to thank Dr. Saeid Farzaneh for all his mental support, insightful and inspiring discussions, and encouragement.

I dedicate my particular thanks to Dr. Jonas Ågren and Prof. Artu Ellmann for providing me with constructive feedback and comments, and useful tips for future work in my half-time seminar. I would also like to thank Prof. Hossein Nahavandchi for reviewing my work and for his thoughtful comments in my final seminar. My work has further been shaped by insightful comments from journal editors and anonymous reviewers. My gratitude goes to all of them.

Not to forget to thank all my colleagues at the University of Gävle, especially colleagues at the Department of Computer and Geospatial Sciences, for providing me with a positive, friendly and supportive atmosphere. The time as a PhD student would not have been as fun without PhD student colleagues and friends at the University of Gävle. My gratitude goes down to Mohammad J., Lea, Daniel, Ali, Anders, Oscar, Gasper, Vipin, Lei, Zheng, Mohammad A., Sandra, Sana, Kuhelee, Arash, Amir, Jamila, Melis, Hossein, Jennie, Lucas, and all other PhD students and friends from the Faculty of Engineering and Sustainable Development for nice fika talks, PhD lunch seminars, after-work outings and much more.

Last but surely not least, to my family, without whom none of this would have been possible. I would like to attribute my countless thanks to all of you for your endless love, support, unwavering belief in me, and for your always being by my side.

List of Papers

This thesis is based on the following papers, which are referred to in the text by Roman numerals.

Paper I

Amin, H., Sjöberg, L. E., and Bagherbandi, M. (2019). A global vertical datum defined by the conventional geoid potential and the Earth ellipsoid parameters. *Journal of Geodesy*, 93(10): 1943-1961. `https://doi.org/10.1007/s00190-019-01293-3`

Paper II

Amin, H., Bagherbandi, M., and Sjöberg, L. E. (2020). Quantifying barystatic sea-level change from satellite altimetry, GRACE and Argo observations over 2005–2016. *Advances in Space Research*, 65(8): 1922-1940. `https://doi.org/10.1016/j.asr.2020.01.029`

Paper III

Gido, N.A., Amin, H., Bagherbandi, M., and Nilfouroushan, F. (2020). Satellite monitoring of mass changes and ground subsidence in Sudan's oil fields using GRACE and Sentinel-1 data. *Remote Sensing*, 12(11): 1792. `https://doi.org/10.3390/rs12111792`

Paper IV

AllahTavakoli, Y., Amin, H., Bagheri, H.R., and Bagherbandi, M. (2022). On an approach to surface mass change detection from satellite gravimetry, a case study of barystatic sea-level, ice-sheet mass and basin mass changes. Under review in *Journal of Geodesy*

Paper V

Amin, H., and Bagherbandi, M. (2022). Mass balance of the Greenland ice sheet and its recent contribution to sea-level rise from the GRACE and GRACE Follow-On time-variable gravity data. *Submitted for publication*

Paper VI

Amin, H., and Bagherbandi, M. (2022). The efficiency of global hydrological and land surface models against GRACE data in quantifying land total water storage variability. *Submitted for publication*

Additional Journal Papers (not included in the thesis):

Paper 7

Bagherbandi, M., Amin, H., Wang, L., and Shirazian, M. (2022). Mantle viscosity derived from geoid and different land uplift data in Greenland. *Journal of Geophysical Research: Solid Earth*, In press. `https://doi.org/10.1029/2021JB023351`

International Conferences and Meetings:

Bagherbandi, M., Amin, H., Gido, N.A., and Sjöberg, L. E. (2017). A novel approach to study ice mass change using satellite data in Greenland and Antarctica. *IAG-IASPEI 39th Joint Scientific Assembly, July 30–August 04, 2017, Kobe, Japan*

Bagherbandi, M., Sjöberg, L. E., and Amin, H. (2018). Towards a world vertical datum defined by the geoid potential and Earth's ellipsoidal parameters (Preliminary results). *IX Hotine-Marussi Symposium, 18–22 June, 2018, Rome, Italy*

Amin, H., Bagherbandi, M., and Sjöberg, L. E. (2018). Global mean sea level budget closure over January 2005 to December 2014. *Nordic Geodetic Commission General Assembly, 03–06 September, 2018, Helsinki, Finland*

Amin, H., Bagherbandi, M., and Sjöberg, L. E. (2019). Evaluation of the closure of global mean sea level budget over January 2005 to August 2016. *27th IUGG General Assembly, 08–19 July, 2019, Montréal, Québec, Canada*

Gido, N.A., Amin, H., Bagherbandi, M., and Nilfouroushan, F. (2020). Satellite monitoring of mass changes and ground subsidence in Sudan's oil fields using GRACE and Sentinel-1 data. *EGU General Assembly 2020, 04–08 May, 2020, Online*

AllahTavakoli, Y., Amin, H., Bagheri, H.R., and Bagherbandi, M. (2022). A new model for surface mass change detection from GRACE(-FO) gravity fields. *NKG Working Group of Geodynamics and Earth Observation (WGGEO), 14–15 March, 2022, Gävle, Sweden*

Bagherbandi, M., Amin, H., Wang, L., and Shirazian, M. (2022). Mantle viscosity derived from geoid and different land uplift data in Greenland. *EGU General Assembly 2022, 23–27 May, 2022, Vienna, Austria*

Author's Contribution to the Papers

In the following, the author's contribution to the appended papers is summarized.

Paper I

- Performing all the numerical experiments and calculations, and preparing all the results,
- analyzing and discussing the results jointly with the co-authors,
- writing the draft of the paper, and
- based on the comments of the other authors, finalizing the paper.

Paper II

- Performing all the numerical experiments and calculations, and preparing all the results,
- analyzing and discussing the results jointly with the co-authors,
- writing the draft of the paper, and
- based on the comments of the other authors, finalizing the paper.

Paper III

- Processing the GRACE data, hydrological models, and in-situ records, and producing the related results based on satellite gravimetry observations, models, and in-situ data,
- analyzing and discussing the results jointly with the other authors,
- contributing to the preparation of the draft of the paper, and
- contributing to finalizing the paper.

Paper IV

- Performing all the calculations and numerical experiments for different case studies, and preparing all the results,
- analyzing and discussing the results jointly with the other authors,
- finalizing the research and writing the draft of the paper jointly with the first author, and
- Reading the prepared draft and contributing to finalizing the paper.

Paper V

- Initiating and conceptualizing the study,
- performing all the numerical experiments and calculations, and preparing all the results,

- analyzing and discussing the results jointly with the co-author of the paper,
- finalizing the research and writing the draft of the paper, and
- finalizing the paper.

Paper VI

- Initiating and conceptualizing the study,
- performing all the numerical experiments and calculations, and preparing all the results,
- analyzing and discussing the results jointly with the co-author of the paper,
- finalizing the research and writing the draft of the paper, and
- finalizing the paper.

Nomenclature

$\bar{P}_{nm}$	Fully-normalized associated Legendre functions
β	Reduced latitude
γ_1	Normal gravity on the surface of the reference ellipsoid
λ	Longitude
ω	The Earth's angular velocity
ϕ	Latitude
ψ	Spherical distance
ρ_{ave}	The Earth's average mass density
ρ_w	Mass density of water
σ	Surface mass density
θ	Spherical co-latitude
a	Semi-major axis of the reference ellipsoid
b	Semi-minor axis of the reference ellipsoid
C_{nm}, S_{nm}	Spherical harmonic coefficients
e	Eccentricity
G	Gravitational constant
GM	Standard gravitational parameter of the Earth
H	Orthometric height
h	Ellipsoidal height
k_n	Load Love number of degree n
M	The Earth's mass
m	Spherical/ellipsoidal harmonic order
N	Geoid height
n	Spherical/ellipsoidal harmonic degree
R	Mean radius of the Earth
r	Geocentric radius
T	Disturbing potential
U_1	Normal potential of the reference ellipsoid
V	Gravitational potential
W_0	Geoid potential

Abbreviation

AOD1B	Atmosphere and Ocean De-Aliasing Level-1B
CSR	Center for Space Research
D	Discharge Mass Flow
DLR	Deutsche Forschungsanstalt für Luft- und Raumfahrt

DOT	Dynamic Ocean Topography
ECMWF	European Centre for Medium-Range Weather Forecasts
EGSIEM	European Gravity Service for Improved Emergency Management
EHC	Ellipsoidal Harmonic Coefficient
EOF	Empirical Orthogonal Functions
EOP	Earth Orientation Parameters
ESA	European Space Agency
ESSP	Earth System Science Pathfinder
EWH	Equivalent Water Height
GBVP	Geodetic Boundary Value Problem
GFZ	Deutsches GeoForschungsZentrum
GGM	Global Gravity field Model
GGRF	Global Geodetic Reference Frame
GHM	Global Hydrological Model
GIA	Glacial Isostatic Adjustment
GMSL	Global Mean Sea Level
GNSS	Global Navigation Satellite System
GRACE	Gravity Recovery and Climate Experiment
GRACE-FO	Gravity Recovery and Climate Experiment Follow-On
GrIS	Greenland Ice Sheet
GRS80	Geodetic Reference System 1980
GSFC	Goddard Space Flight Center
GWS	Groundwater Storage
IAG	International Association of Geodesy
ICA	Independent Component Analysis
ICGEM	International Centre for Global Earth Models
IGG	Institute of Geodesy and Geoinformation
IHRF	International Height Reference Frame
IHRS	International Height Reference System
ITSG	Institute of Geodesy at Graz University of Technology
JPL	Jet Propulsion Laboratory
KBR	K-Band microwave Ranging
KeFIn	Kernel Fourier Integration
LRI	Laser Ranging Interferometry
LSM	Land Surface Model
LUH	Leibniz Universität Hannover
Mascon	Mass concentration
MB	Mass Balance

MDT	Mean Dynamic Topography
MEE	Mean Earth Ellipsoid
MPIOM	Max-Planck-Institute Ocean Model
MSS	Mean Sea Surface
NAP	Normaal Amsterdams Peil
NASA	National Aeronautics and Space Administration
NWP	Numerical Weather Prediction
OBP	Ocean Bottom Pressure
SAR	Synthetic Aperture Radar
SDS	Science Data System
SEC	Surface Elevation Change
SHC	Spherical Harmonic Coefficient
SLR	Satellite Laser Ranging
SMB	Surface Mass Balance
SSA	Singular Spectrum Analysis
TRMM	Tropical Rainfall Measuring Mission
TWS	Total Water Storage

Table of Contents

1 Introduction

1.1 Background

The Earth's gravity field is defined as an attraction force that the Earth applies on any mass component normal to the equipotential surface (Tiwari and Hinderer, 2011). According to Newton's law of gravitation, the force exerted by the Earth on any unit mass depends on the distribution of mass and how it is spatially located in the Earth system. Accordingly, ongoing processes in the Earth subsystems (geosphere, biosphere, cryosphere, hydrosphere, and atmosphere) and the fluid envelopes of our planet induce changes in the gravity field of the Earth across a wide range of temporal and spatial scales (Tiwari and Hinderer, 2011). Among all processes that redistribute the mass within the Earth system, Earth's polar motion, solid and ocean tides, oceanic and atmospheric circulation, hydrological and cryospheric changes, volcanic, seismic and tectonic activities, and Earth's inner and fluid core motions can be mentioned, in which the majority of mass redistribution is attributed to the water movement (in various states of solid, liquid, and vapor) within the Earth system.

Mass redistribution on the Earth's surface alters the shape of the Earth's gravity field. According to the classical Gauss–Listing definition, the geoid is an equipotential surface of the Earth's gravity field that in a least-squares sense best approximates the undisturbed mean sea level (Gauss, 1828; Listing, 1872). Therefore, since the Earth's gravity field is subject to temporal changes, one may not consider the geoid as a static surface. We essentially need two factors for geoid determination, namely (a) knowledge of the Earth's gravity potential and (b) a method to show the geometry of the geoid surface, in which the latter can be achieved by defining a known reference ellipsoid and representing the geoid surface with respect to the surface of that reference ellipsoid (Sideris, 2011). In this context, due to the fact that the geoid is the physically meaningful reference datum for the orthometric heights and considering that it can be used for the global unification of regional height systems (Sideris, 2011), the geometric representation of the geoid is of specific importance. Hence, accepting the geoid as the global vertical datum signifies that the datum is determined by the potential (W_0) of this particular reference surface of the Earth's gravity field (Sjöberg, 2013).

Although mass redistribution, due to the activities that form the Earth's surface, over periods of thousands to millions of years lead to changes in the Earth's gravity field, however, as these variations do not take place on the human timescale, the Earth's gravity field can be considered as *static* over such long periods (Tiwari and Hinderer, 2011). However, Wahr et al. (1998) discussed

that on timescales less than several hundred years, temporal variations in the Earth's gravity field are mainly caused by the movement of water (in its various forms) through the Earth's relatively thin fluid envelope that can be detected by space geodetic techniques. Therefore, mass redistribution and transport between various subsystems (e.g., ice sheets and oceans) affect the equipotential surfaces in the Earth's gravity field. Accordingly, as the data have significantly improved, the geoid potential (W_0) have to be updated in such a way that it meets the classical Gauss–Listing definition. This means that according to the Gauss–Listing definition, the geopotential at the geoid surface, W_0, may not be equal to the normal potential at the surface of the chosen reference ellipsoid (Sjöberg, 2013).

As mentioned before, over periods of decades, the Earth's gravity field undergoes temporal variations mainly because of the movement of water mass on, above, and below the surface of the Earth. The global water cycle, also referred to as the hydrological cycle, presents the ongoing redistribution of water through the land, ocean, and atmosphere. As the energy exchange between the Earth's subsystems characterizes its climate, and since the hydrological cycle is directly associated with the Earth's energy exchange, therefore, a major part of the natural climate variability on the planet is attributed to the water mass redistribution between land, ocean, and atmosphere. Apart from the natural climate variability that is dominated by the water cycle, water mass redistribution can be a vital sign of ongoing climate change and global warming processes. More specifically, the present-day sea-level rise and cryospheric ice-mass change are two critical indicators of climate change and global warming. Figure 1 shows physical processes included in the hydrological cycle.

Accurate estimations of the Earth's gravity field variations provide the opportunity to constrain the fundamental reasons for dynamic changes of mass distribution within the Earth system processes. However, as the changes, and more specifically within the global water cycle, occur over a very large spatial scale over land, ocean, and atmosphere, it is challenging to observe and measure the ongoing variations. Over the last few decades, different observing systems and approaches have been designed, developed, and used to improve the possibility and accuracy of mass change monitoring. For many years, and prior to the advent of satellite-based monitoring approaches, traditional in-situ gauge-based observations of, for instance, sea-level change, precipitation, evapotranspiration, soil moisture, and groundwater storage changes were the only way of discussing variations in the Earth subsystems. Subsequently, the advent of satellite-based missions, each aimed at monitoring a particular mass change process, supported the traditional observing systems over regional and

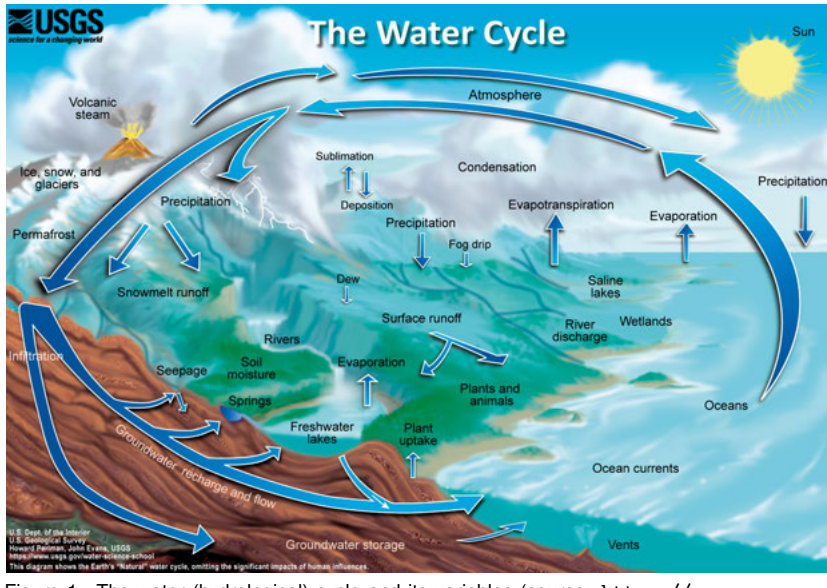

Figure 1. The water (hydrological) cycle and its variables (source: `https://www.usgs.gov/media/images/natural-water-cycle-0`)

global scales. Starting in the early 90s, different satellite altimetry missions aimed at nearly globally monitoring of sea-level changes (e.g., Shum et al., 1995). Focusing on the cryosphere, for instance, ICESat (Ice, Cloud, and Land Elevation Satellite) mission was utilized for monitoring topography and elevation of the Earth's ice sheets (Zwally et al., 2002). Moreover, one can, for instance, name TRMM (the Tropical Rainfall Measuring Mission) that had been launched in 1997 for improving our understanding of the distribution and variability of precipitation (Theon, 1994). However, among all, satellite gravimetry missions have provided an integrated global view of ongoing mass variation processes within the Earth system.

The current generation of satellite gravimetry missions has immensely revolutionized the way we look at dynamic processes in the Earth's surface and, consequently, has considerably improved our understanding of the Earth's climate system. By observing the Earth's gravity field in terms of the contributors to temporal changes, since 2002, the Gravity Recovery and Climate Experiment (GRACE) mission and its successor, GRACE Follow-On (FO), have enabled us to determine, with valuable spatial and temporal resolutions, variations in the Earth's gravity field due to mass transport and redistribution within all components of the Earth system, namely the cryosphere, hydrosphere, oceans, and solid Earth (Tapley et al., 2004a; Kornfeld et al., 2019). By enabling researchers to estimate changes in total

integrated water mass over a period of time, GRACE(-FO) monthly observations offer, along with the other sources of observations in the Earth system, the unique possibility to study the closure of terrestrial water/sea-level budget.

1.2 Problem Definition and Research Objectives

The need for an accurate Global Geodetic Reference Frame (GGRF) is essential to satisfy the ever-rising demand for reliable decision-making in a location-based society. In this frame, the GGRF is required to track changes in different subsystems of the Earth system. For example, it plays a vital role in disaster monitoring and specifying zones with a high risk of flooding, earthquakes, and droughts. Moreover, the GGRF is required for tracking sea-level, ice-sheet, and glacier changes, movement of tectonic plates, land subsidence and uplift, universal timing, positioning and navigation through satellite positioning technology, and mapping.

The vertical datum of a global unified height reference system with respect to the Earth's body is defined by the potential of the geoid, W_0. Furthermore, an estimation of the geopotential value W_0 of the global geoid, as a parameter of the Earth's gravity field, is essential to quantitatively estimate the reference Mean Earth Ellipsoid (MEE) parameters, which is characterized as the globally best-fitting ellipsoid to the geoid surface (Heiskanen and Moritz, 1967, p. 214). However, as Sánchez et al. (2016) explained, a discrepancy up to $-2.6\ \mathrm{m^2\,s^{-2}}$ has been reported in the W_0 value based on the computations performed since 2005, equivalent to a height difference of about 27 cm. This level of disagreement in the W_0 estimations over such a short period of time is mainly attributed to the differences in the characteristics of input data. Accordingly, as the Earth's Global Gravity field Models (GGM), Mean Sea Surface (MSS), and Mean Dynamic Topography (MDT) models have been greatly improved, utilizing standardized datasets and novel computational strategies results in a new estimate of W_0.

By employing various methods and a large range of datasets, the estimation of a global value for geoid potential, W_0, has been addressed in many studies. Among all, some studies aimed at equating W_0 with the normal potential (U_1) at the surface of a new-defined level ellipsoid (e.g., Rapp et al., 1991; Rapp, 1995; Moritz, 2000; Dayoub et al., 2012). Some other studies quantified a global value for W_0 related to a level surface that minimizes the square sum of the Dynamic Ocean Topography (DOT) estimated over the entire ocean (e.g., Burša et al., 1992; Nesvornỳ and Šíma, 1994; Burša et al., 1998a, 2007b; Sanchez, 2007; Dayoub et al., 2012). Čunderlík and Mikula (2009) applied the

boundary element method to the linear altimetry–gravimetry boundary value problem, with employing the collocation technique with linear basis functions for discretization of boundary element method over both land and ocean areas, and reported a value for W_0 as a numerical result of utilizing that approach. In a more recent study, Sánchez et al. (2016) took the advantage of newly released GGMs and MSS models and utilized standardized data and techniques to estimate a new global value for W_0.

However, all the previous studies are based on a pre-defined level ellipsoid and/or on equating W_0 with the normal potential (U_1) at the surface of level ellipsoid. Furthermore, most of the reported values for W_0 have been estimated based only on considering ocean areas and continents have been neglected. Accordingly, in this study, a new technique that simultaneously estimates the global value for the geoid potential, W_0, and the geometrical parameters of the MEE is examined. In this regard, we achieve the best fits of geoid potential, W_0, and geometrical parameters of the MEE, which match each other pursuant to the definitions of the geoid and the MEE. In addition, to evaluate the sensitivity of estimations to the input data, the effect of various aspects of input data on the estimated value for the geoid potential is studied, including the effect of time-dependent Earth's gravity field changes.

The Earth's gravity field consists of a static part and a time-varying part. Changing level of water in ocean, losing or gaining ice over the Earth's ice sheets and glaciers, movement of water between different hydrological reservoirs, circulation in the atmosphere and ocean, the Earth's mantle convection, and many other processes result in a continuous transport and redistribution of mass within the Earth system, forming the time-varying part of the Earth's gravity field. Accordingly, the Earth's gravity field and its time-dependent changes are intimately interconnected with mass redistribution. Therefore, a more detailed and accurate estimation of mass transport and redistribution between the Earth subsystems enables us to model the Earth's gravity field and its variations more accurately. In this context, temporal changes of the Earth's gravity field are quantified by measurements of the Earth's attraction force at the same point in space with time. The GRACE, and then GRACE-FO, have been providing the Earth's time-variable gravity field with unprecedented accuracy at monthly intervals.

GRACE(-FO) mission consists of two almost similar satellites, in which one follows the other one in a single orbital plane. As both the lead and the trailing spacecrafts are equipped with a microwave ranging system, they regularly measure the inter-satellite range. In addition, three-axis electrostatic accelerometers are installed at the center of gravity of each spacecraft to measure

the effect of non-gravitational forces so that it can be differentiated between gravity effects and those arising from non-gravitational forces. Moreover, the spacecrafts are equipped with geodetic Global Positioning System (GPS) receivers for positioning purposes. The changes in the measured inter-satellite separation are then converted to the time-variable gravity fields and provided in the form of monthly Spherical Harmonic Coefficients (SHCs).

GRACE- and GRACE-FO-derived time-variable monthly gravity solutions, however, are subject to inherent errors that have to be addressed appropriately to arrive at dependable and accurate estimates of the Earth's surface mass change. Among all, the measurements cannot resolve mass changes of high spatial resolutions because of the attenuation of small-scale gravity variations at the altitude of spacecrafts. Accordingly, as the spatial resolution of the GRACE- and GRACE-FO-based solutions is limited, it is challenging to distinguish between mass change signals in contiguous regions, for instance, adjacent terrestrial water storages or between the ocean and ice-covered land areas. This limited spatial resolution is known as the primary reason for the so-called "leakage error". Besides, GRACE and GRACE-FO time-variable gravity fields reveal high correlated errors, which are mainly caused by the mission geometry, and need to be properly filtered out to be able to infer mass changes at the surface of the Earth from monthly solutions (e.g., Swenson and Wahr, 2006; Kusche, 2007). However, applying filtering strategies for signal-noise separation mostly results in an additional signal attenuation leading to increased leakage. Therefore, it is essential to use an appropriate filtering approach that offers a suitable trade-off to minimize both correlated and leakage errors. In addition to the selection of an appropriate filtering approach, a proper leakage correction method is required to be selected as well to counteract the signal attenuation caused by the filtering procedure and, thereby, to infer unbiased changes in mass (e.g., Chambers and Bonin, 2012; Chen et al., 2015). Accordingly, in this contribution, different destriping and smoothing filters as well as various leakage correction techniques are utilized to estimate surface mass change within both ocean and land areas.

Besides the problems associated with the GRACE and GRACE-FO time-variable gravity products, the fundamental problem of inferring the Earth's surface mass variations from the time-varying gravity fields is also of interest. The analytical model of Wahr et al. (1998) has conventionally been employed as a common solution to convert the GRACE(-FO) SHCs into the Earth's surface mass change. A set of assumptions has been considered to formulate this common analytical model, including: (1): the mass redistribution is concentrated in the Earth's surface, (2): the Earth's topography is negligible, and (3): the Earth has a spherical shape. On the other hand, due to

ever-improving processing techniques as well as background models, the accuracy of GRACE(-FO) monthly solutions is enhancing over time, and also a longer time series of GRACE(-FO) data is available, which provides the possibility of quantifying seasonal and interannual variations with greatly higher accuracy than single monthly fields. Therefore, the spherical approximation considered by Wahr et al. (1998) to formulate their model is no longer tenable for estimating the Earth's surface mass change. In this study, a new model of surface mass change detection from the satellite gravimetry-based Earth's gravity field variations is developed and utilized in which the underpinning assumptions are closer to the reality of the Earth.

Specific research objectives that will be addressed in relation to the presented problems are as follows:

1. Study on unbiased value of the geoid potential and evaluating the impact of time-dependent Earth's gravity field changes on the estimation of geoid potential.
2. Evaluating the impact of filtering approaches on estimating surface mass change from time-variable satellite gravimetry observations and proposing optimal filtering method for inferring surface mass change from satellite gravimetry monthly solutions.
3. Assessment the efficiency of leakage correction strategies in estimating surface mass changes from time-variable satellite gravimetry observations.
4. Developing and proposing an improved analytical model of surface mass change detection from time-varying gravity fields and studying the accuracy of GRACE(-FO)-derived mass change estimates based on the proposed model with respect to the previous analytical models.

1.3 Scope of the Study and Target Areas in Focus

The importance of studying the Earth's gravity field change lies in its application in revealing the most critical indicators of climate change, climate variability, and global warming. Quantifying the redistribution and transport of mass between the Earth subsystems (e.g., the Global Mean Sea-Level (GMSL) rise and cryospheric mass change) is of great importance for understanding the effect of climate change and global warming on our planet. In this regard, time-variable satellite gravity data are frequently used to quantify the Earth's surface mass change. Different aspects of analyzing satellite-based time-variable gravity data are considered in this study so that the accuracy of the Earth's surface mass change estimations is enhanced. Accordingly, the application of GRACE

and GRACE-FO in the estimation of barystatic sea-level change, cryospheric mass change, and mass variations in continents is studied so that the research objectives are addressed. In addition, as the data have considerably improved and GMSL change has increased to about 3.7 $\mathrm{mm\,yr^{-1}}$ today (Chen et al., 2018), the estimation of geopotential at the geoid is considered as well in this study.

In accounting for the validation of results in this study, other datasets derived from techniques other than satellite gravimetry are analyzed. Static global gravity models, altimetry-based mean sea surface models, mean dynamic topography models, altimetry-based monthly global mean sea level, Argo-based monthly salinity and temperature observations over the ocean, hydrological models, in-situ oil wells production data, altimetry-based surface elevation change data, and climate models are the models and datasets analyzed in this study.

The entire PhD work is centered on three areas of study: (1) estimation of fundamental parameters of physical and geodetic reference frames and evaluation of the sensitivity of estimations to the input data, (2) surface mass change studies based on the conventional spherical model, and (3) surface mass change studies based on the new proposed model in which the real shape of the Earth's surface is taken into account rather than simply approximating it by a sphere or an ellipsoid. In each of the studies, different results are generated, and in some new techniques are developed, which can serve as basic methods in other studies. For instance, the method developed for surface mass change detection is used (in Paper V) to quantify the Greenland ice-sheet mass balance and its contribution to the present-day sea-level rise.

Each of these focus areas involves different methods relevant to producing the expected results, which addresses the study aims and the specific research objectives. With W_0 quantification, the main aim is to fulfill research objective #1, and in producing the outputs, relying on a novel method, the newest gravity field, mean sea surface, and mean dynamic topography models are analyzed. In the estimation of regional and global scale mass changes to succeed in research objectives #2, #3, and #4, this does not only include processing the satellite gravimetry-based data but also data from other techniques like satellite altimetry. In this regard, results are achieved based on both the conventional spherical model and a new proposed model.

1.4 Thesis Outline

The main goal of this contribution is to use satellite gravimetry observations to study the Earth's gravity field, estimate its parameters and variations by time, and thereby accurately estimate the Earth's surface mass variations. The study

is mainly focused on analyzing GRACE and GRACE-FO time-variable gravity fields. Accordingly, the theoretical background is presented in Chapter 2. In Section 2.1, the theory of the geoid reference geopotential is reviewed and an overview of different methods of estimating W_0 is provided. Following, Section 2.2 is devoted to different aspects of studying the Earth's gravity field change using GRACE(-FO) observations. Section 2.2.1 gives a detailed overview of the GRACE and GRACE-FO missions. Next, different data products of the GRACE and GRACE-FO missions are explained in Section 2.2.2. In Section 2.2.3, a comprehensive view of how time-variable geopotential coefficients are converted to the surface mass changes based on the common spherical model, is presented. In this way, different sources of uncertainty and the required corrections is discussed. Finally, Chapter 2 is closed by presenting the intermission gap between GRACE and GRACE-FO satellite missions in Section 2.2.4.

In Chapter 3, data and research methodology is presented. Section 3.1 provides a detailed introduction to the new method that is examined in this study to estimate the geoid reference potential. In Section 3.2, a novel model of surface mass change detection based on time-varying satellite gravimetry observations is presented. Section 3.3 closes this chapter by providing information about different datasets that are used in this study.

Chapter 4 presents a summary of each scientific article that has been published/submitted under this PhD project. In Chapter 5, the major findings of this thesis are summarized and discussed, remaining problems are reported, and recommendations for further research are made. Finally, all the published and submitted scientific papers are enclosed in this thesis.

2 Theoretical Background

2.1 The Geoid Reference Potential, W_0

There is an infinite number of equipotential surfaces (the surfaces of constant gravity potential) in the Earth's gravity field of which one serves as the conventional zero datum for all topographical features and is termed "geoid". The geoid is defined as the shape of the sea surface in the absence of non-gravitational influences and only under those caused by the Earth's gravity field. Pursuant to the classical Gauss–Listing definition, the geoid is described as an equipotential surface of the Earth's gravity field that in a least-squares sense best approximates the mean sea level at rest (Gauss, 1828; Listing, 1872). However, as the ocean is not completely at rest, owing to the ocean currents, and also changes in temperature, salinity, and air pressure within the ocean and other perturbing phenomena, there is a separation between the geoid and time-averaged sea surface or Mean Sea Level (MSL), called Mean Dynamic Topography (MDT). Accordingly, as the geoid best fits the Earth's surface only over the ocean, the geoid is the Earth's shape abstracted from its topographic features (Hessler, 2009).

In recent decades, with impressive progress in satellite-based observing systems (Global Navigation Satellite System (GNSS), satellite altimetry, and satellite gravimetry) and other geodetic techniques, as well as developments in processing strategies, the need for a precise definition and realization of a unified global vertical reference system was considered more than ever. In 2015, the International Association of Geodesy (IAG) released a new resolution (Drewes et al., 2016, resolution No. 1) emphasizing the definition of the International Height Reference System (IHRS) as the conventional gravity field-related global height system. The realization of the IHRS requires, in geopotential space, the adoption of a global potential value to define the reference level (zero-height) of a height system (e.g., Sánchez, 2009; Sjöberg, 2013; Sánchez et al., 2021). In this context, as a fundamental parameter of the Earth's gravity field, W_0 defines the Gauss-Listing geoid that serves as a conventional reference level for the determination of vertical coordinates. Consequently, the height values of a local coordinate system can be unambiguously presented by geopotential numbers referred to W_0, and in this way, all points in local datums can be transferred to the global vertical system.

Moreover, the global estimation of geoid potential, W_0, characterizes the reference MEE (e.g., Sjöberg, 2013) that is defined as the globally best-fitting ellipsoid to the geoid surface (Heiskanen and Moritz, 1967, p. 214), whose mass is the same as that of the real Earth and serves as the mathematical

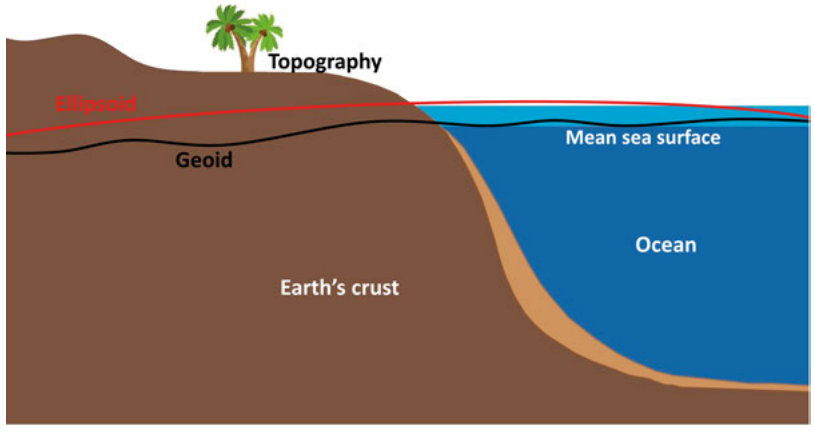

Figure 2. Geodetic descriptions of the Earth's surface

reference frame of the Earth for computations. The gravity field generated by the reference ellipsoid is called the normal gravity field and U_1 represents the normal potential of the MEE. Figure 2 shows geodetic descriptions of the Earth's surface, including the Earth's physical surface, the geoid, and a reference ellipsoid.

In the process of estimating a value for the geoid potential, W_0, to fulfill the Gauss-Listing definition, it is required to consider conventions other than removing disturbing forces from sea level (e.g., oceanic currents). As the MSS is defined over a time span, the estimation of W_0 should also be attributed to the corresponding time period. In addition, MSS can be defined locally based on in-situ observations or globally based on satellite-based products. Accordingly, W_0 can be estimated at a specific location, or an average of several locations, or over the entire ocean globally (Sánchez et al., 2016). Furthermore, since the sea level changes and mass continuously redistributes in the Earth system, one may not consider the geoid as an invariant surface. Therefore, as the sea-level change and mass redistribution can be quantified using space geodetic techniques, special considerations should be given to the time variations of W_0.

Based on employing different processing strategies and also considering a huge variety of datasets, many studies have addressed the estimation of a value for W_0. For instance, some studies were set up based on the strategy of equating the geoid potential, W_0, with the normal potential, U_1, generated by a new-defined mean Earth ellipsoid (e.g., Rapp et al., 1991; Rapp, 1995; Moritz, 2000; Dayoub et al., 2012). However, since in this method, the reliability of the estimation of W_0 depends largely on how precise the MEE is defined, therefore, this strategy of estimating W_0 does not always fulfill the requirements for various geodetic applications.

Some studies suggested W_0 correspond to an equipotential surface coinciding with the MSL measured at the location (for instance p) of an arbitrarily chosen tide gauge ($W_0 = W_0^p$). In this regard, as W_0^p cannot be accurately estimated, and since the vertical datum can arbitrarily be adopted, other geopotential values were assigned. For instance, Ihde et al. (2002) set the geopotential value of equipotential surface passing through the datum of "Normaal Amsterdams Peil" (NAP) to be the normal potential of the Geodetic Reference System 1980 (GRS80). In other study, for instance, Ardalan and Safari (2005) utilized a GGM to compute the gravity potential and equated W_0 with the computed gravity potential at the location of a reference tide gauge (for instance W_0^p) where the Earth's gravity potential, outside the topographic masses, is given by (Torge, 1989, p. 70 and 72):

$$\begin{aligned} W(r,\theta,\lambda) = \frac{\mathrm{GM}}{R}\sum_{n=0}^{\infty}\sum_{m=0}^{n}\left(\frac{R}{r}\right)^{(n+1)}\bar{P}_{nm}(\cos\theta) \\ \times\left(C_{nm}\cos m\lambda + S_{nm}\sin m\lambda\right) + \frac{1}{2}\omega^2 r^2\sin^2\theta, \end{aligned} \tag{2.1}$$

where (r,θ,λ) are the geocentric radius, spherical co-latitude, and longitude of the computational point, respectively, GM is the standard gravitational parameter (the product of the gravitational constant G and the Earth's mass M), $\bar{P}_{nm}$ denotes the fully-normalized associated Legendre functions of degree n and order m, C_{nm} and S_{nm} are the fully-normalized SHCs from a GGM, and ω is the Earth's angular velocity. The first term on the right side of Eq. 2.1 is the Earth's gravitational potential and the second term represents its rotational potential (e.g., Sjöberg and Bagherbandi, 2017, p. 84). One can directly use Eq. 2.1 to estimate the geoid potential as the Earth's gravity potential at the radius vector r_g of the geoid, i.e. $W_g = W_0 = W(r_g,\theta,\lambda)$ (cf. Dayoub et al., 2012; Sjöberg and Bagherbandi, 2017). However, in this processing strategy ($W_0 = W_0^p$), the DOT at the location of tide gauge is not taken into account and W_0^p does not represent a globally-defined geoid.

By considering the MDT, and following the direct estimation of W_0 using Eq. 2.1 with r_g as the radius of geoid surface, one can define $r_g = r_g(\theta,\lambda) = r_1(\theta) + N(\theta,\lambda)$, where $r_1(\theta)$ is the geocentric radius vector of the reference ellipsoid and $N(\theta,\lambda)$ is the geoid height. Over the oceans, the geoid height can be geometrically determined as the discrepancy between satellite altimetry-derived MSS and DOT, where the latter can be obtained either through oceanographic approaches or by satellite altimetry observations and a pre-defined geoid model.

As a different approach, one can base the estimation of W_0 on Bruns' formula (Bruns, 1878). As such , the disturbing potential at any location (r,θ,λ) can

be estimated as $T(r,\theta,\lambda) = W(r,\theta,\lambda) - U_1(r,\theta,\lambda)$ (refer to , e.g., Sjöberg and Bagherbandi (2017, p. 222) to see how U_1 is computed using a GGM). Accordingly, on the surface of geoid:

$$T_g = W_0 - U_g = W_0 - (U_1 - \gamma_1 N), \tag{2.2}$$

where γ_1 is the normal gravity on the surface of the reference ellipsoid. Therefore:

$$W_0 = U_1 - \gamma_1 N + T_g. \tag{2.3}$$

By ignoring the effect of considering $r_1(\theta)$ instead of r_g, T_g can be substituted by the disturbing potential computed on the surface of the reference ellipsoid using a GGM, i.e. $T^{\mathrm{GGM}}(r_1(\theta),\theta,\lambda)$. Consequently, Eq. 2.3 can be rewritten as:

$$N = \frac{T^{\mathrm{GGM}}}{\gamma_1} - \frac{\Delta W_0}{\gamma_1}, \tag{2.4}$$

where ΔW_0 is defined as $\Delta W_0 = W_0 - U_1$. On the other hand, the SHCs of a GGM can be used directly along with Bruns' formula to estimate the geoid height as:

$$N^{\mathrm{GGM}} = \frac{T^{\mathrm{GGM}}}{\gamma_1}. \tag{2.5}$$

A simple comparison between Eqs. 2.4 and 2.5 reveals that the GGM-derived geoid height lacks the unknown correction $-\Delta W_0 / \gamma_1$. In this regard, it is worth noting that, since T_g is the disturbing potential inside the topographic mass, accordingly, one needs to take into account the analytical downward continuation error or topographic bias to estimate N^{GGM} over the land areas using a GGM and Bruns' formula (e.g., Sjöberg, 2007).

Taking the advantage of satellite altimetry observations for determining DOT, and using a pre-defined geoid, some studies estimated W_0 as the potential on an equipotential surface that minimizes the square sum of the DOT measured at the location of reference tide gauges all around the world (Lelgemann, 1977). In other words, the following condition should be satisfied (cf. Sánchez, 2012, Eq. 20):

$$\sum_{p=1}^{n} \left[W_0 - \left(W_0^p + \delta W^p\right)\right]^2 = \min, \tag{2.6}$$

and consequently:

$$W_0 = \frac{1}{n} \sum_{p=1}^{n} \left(W_0^p + \delta W^p\right), \tag{2.7}$$

where δW^p represents the potential differences produced by DOT at the sea

surface at the location of each tide gauge. Accordingly, as this strategy is based on determining the DOT, precise measurements of the sea surface and the Earth's gravity field at the location of reference tide gauges around the world are required. However, as tide gauges are typically located in coastal areas and the accuracy of satellite altimetry observations decreases over shallow water and coastal zones (Cipollini et al., 2017), therefore, this approach does not lead to a precise estimation of W_0. Moreover, the final output in this method is highly dependent on the selection of reference tide gauges.

Following the previous approach, a new strategy of estimating W_0 was considered in which W_0 corresponds to an equipotential surface that minimizes the square integral of the DOT obtained within the ocean on a global scale (Burša et al., 1992; Nesvornỳ and Šíma, 1994; Burša et al., 1997, 1998a,b, 1999, 2002a,b, 2007b,a; Sanchez, 2007; Dayoub et al., 2012), i.e. (cf. Sánchez, 2012, Eq. 21):

$$\iint_{\Omega_1} \mathrm{DOT}^2 d\Omega = \min, \tag{2.8}$$

where Ω is the unit sphere and Ω_1 represents the ocean-covered areas. As shown in Figure 3, the DOT at any given point j located at the sea surface can be achieved as (Sacerdote and Sanso, 2001; Sánchez, 2012):

$$\mathrm{DOT}_j = [h_s - r_j - N_j] = \frac{W_j - W_0}{\gamma_j}, \tag{2.9}$$

where h_s is the ellipsoidal height of the satellite w.r.t. a reference ellipsoid, r_j is the range observation measured by the satellite denoting the distance between the satellite and the point j, N_j, γ_j, and W_j represent geoid height, normal gravity (e.g., Sjöberg and Bagherbandi, 2017, p. 22), and gravity potential (Eq. 2.1) at point j, respectively. Accordingly, the target function defined in Eq. 2.8 is minimized by the following condition (Sacerdote and Sanso, 2001; Sánchez et al., 2016):

$$\begin{aligned} \frac{\partial}{\partial W_0} \iint_{\Omega_1} \mathrm{DOT}^2 d\Omega &= \frac{\partial}{\partial W_0} \iint_{\Omega_1} \left[\frac{W_j - W_0}{\gamma_j} \right]^2 d\Omega \\ &= -2 \iint_{\Omega_1} \frac{1}{\gamma_j^2} (W_j - W_0)\, d\Omega = 0, \end{aligned} \tag{2.10}$$

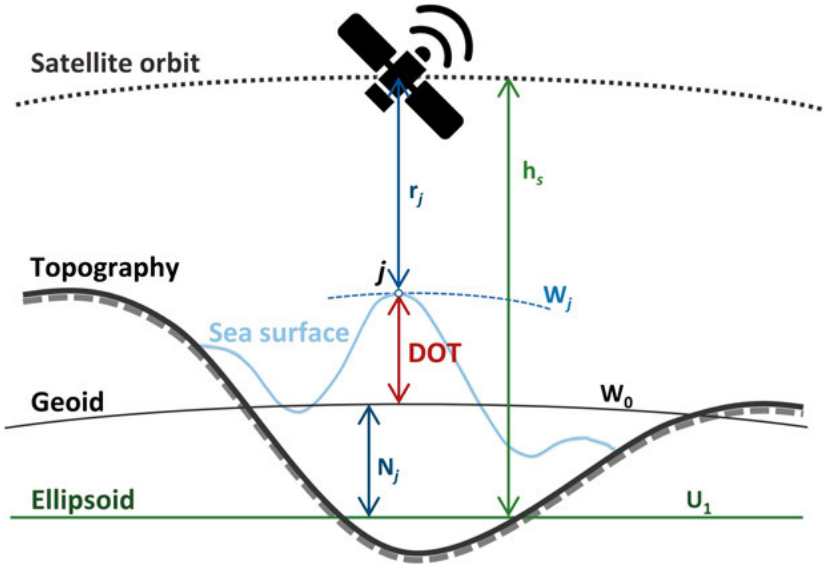

Figure 3. A schematic illustration of dynamic ocean topography, geoid height, satellite ellipsoidal height, and range observation (not to scale)

from which we get (cf. Sacerdote and Sanso, 2001, Eq. 5):

$$W_0 = \frac{\iint_{\Omega_1} \frac{W_j}{\gamma_j^2} d\Omega}{\iint_{\Omega_1} \frac{1}{\gamma_j^2} d\Omega}. \tag{2.11}$$

As the disturbing potential at each point j is estimated as $T_j = W_j - U_j = W_j - (U_1 - \gamma_j h_j)$, therefore, W_j can be substituted by $U_1 - \gamma_j h_j + T_j$, where h_j is the ellipsoidal height of j. Accordingly, by considering that the disturbing potential can be estimated by a GGM, one can rewrite Eq. 2.11 as:

$$W_0 = U_1 + \frac{\iint_{\Omega_1} \left[\frac{T_j^{\mathrm{GGM}} - \gamma_j h_j}{\gamma_j^2} \right] \mathrm{d}\Omega}{\iint_{\Omega_1} \left[\frac{1}{\gamma_j^2} \right] \mathrm{d}\Omega}. \tag{2.12}$$

However, the main drawback of this approach is that it accounts for only ocean-covered areas and is not defined over the entire Earth.

In a more recent study, Sánchez et al. (2016) relied on newly released GGMs and MSS models and employed standardized data and techniques to estimate a new global value for W_0. They explained that "*if the sea surface S* [equivalent to Ω_1 in Eq. 2.11] *would coincide with an equipotential surface, it would be*

sufficient to determine the potential W at any point at S to know the potential value W_S [equivalent to W_j]". They continued "*since this is not the case, Eq. (10)* [equivalent to Eq. 2.11] *has to be evaluated in a discrete form based on those points k* [equivalent to *i*] *describing a quasi-stationary representation of the sea surface*". Accordingly, as the potential at each point i, W_i, is quantified as:

$$W_i = U_1 - \gamma_i h_i + T_i, \tag{2.13}$$

then, Eq. 2.11 can be written as (cf. Sánchez et al., 2016, Eq. 12):

$$W_0 = U_1 + \frac{\sum_1^i \left[\frac{T_i^{\mathrm{GGM}} - \gamma_i h_i}{\gamma_i^2}\right] \delta\Omega_i}{\sum_1^i \left[\frac{1}{\gamma_i^2}\right] \delta\Omega_i}, \tag{2.14}$$

where h_i is the ellipsoidal height of the computational point, T_i^{GGM} is the disturbing potential obtained from a GGM, and $\delta\Omega_i = \cos\varphi\ \delta\varphi\ \delta\lambda$ (φ and λ are geodetic latitude and longitude). In this regard, they also proposed that DOT be subtracted from the sea surface heights to arrive at the MSS nearer to an equipotential surface. As such, DOT should be served as a quasi-stationary parameter precisely in the same way as the sea surface heights are also served. This implies that one needs to remove all time-varying factors influencing the instantaneous sea surface. In this case, one may not need to consider the condition introduced in Eq. 2.10, and Eq. 2.13 can be rewritten as (cf. Sánchez et al., 2016, Eq. 13):

$$W_{i0} = U_1 - \gamma_{i0}\left(h_i - \mathrm{DOT}_i\right) + T_{i0}, \tag{2.15}$$

and (cf. Sánchez et al., 2016, Eq. 14)

$$\begin{aligned} W_0 &= \frac{1}{\Omega_0} \iint\limits_{\Omega_0} W_{\Omega_0}\, \mathrm{d}\Omega_0 \\ &= U_1 + \frac{1}{\Omega_0} \iint\limits_{\Omega_0} \left[T_{\Omega_0} - \gamma_{\Omega_0}\left(h_\Omega - \mathrm{DOT}_\Omega\right)\right] \mathrm{d}\Omega_0, \end{aligned} \tag{2.16}$$

where Ω_0 stands for the surface $[h - \mathrm{DOT}]$. The discrete representation of Eq. 2.16 would be (cf. Sánchez et al., 2016, Eq. 15):

$$W_0 = U_1 + \frac{\sum_1^i \left[T_{i0} - \gamma_{i0}\left(h_i - \mathrm{DOT}_i\right)\right] \delta\Omega_{i0}}{\sum_1^i \delta\Omega_{i0}}. \tag{2.17}$$

Sánchez et al. (2016) estimated and reported W_0 values based on Eqs. 2.14

and 2.17. In this strategy of estimating W_0 as well, the main disadvantage is including only oceans and neglecting the land areas.

As Sánchez et al. (2016) explained, the quantification of an "absolute" value for W_0 from observational data is not feasible unless after considering sufficient constraints, in which the solution is possible only in the context of the Geodetic Boundary Value Problem (GBVP). The GBVP is another formulation that have been used for estimating a value for W_0. For instance, Sánchez (2008) empirically evaluated the fixed GBVP, where the boundary surface was geometrically represented by an MSS model, and estimated a reference geopotential value W_0 (in the fixed GBVP, since the boundary surface is regarded to be geometrically known, the only unknown parameter is the potential value). Čunderlík and Mikula (2009) applied the boundary element approach to the linear altimetry–gravimetry boundary value problem. They included both ocean and land areas, and discretized boundary element method over land and ocean areas using the collocation technique with linear basis functions. For representing the geometry of the boundary surface, they utilized an MSS model over the ocean, and a combination of a topography model and a GGM on the continents, and finally reported an absolute value for W_0 as a numerical result of utilizing that approach.

2.2 Studying the Earth's Gravity Field Change using GRACE and GRACE-FO Observations

In this section, first, the concept of the Gravity Recovery and Climate Experiment (GRACE) and GRACE Follow-On (GRACE-FO) missions is addressed. Afterward, different types of GRACE(-FO) data products are introduced. Thereafter, in Section 2.2.3, a summary of the processing steps to infer surface mass changes from GRACE(-FO) time-varying gravity solutions is provided. Within this context, a common analytical solution to the problem of surface mass change detection from the satellite gravimetry data is reviewed, and also the required corrections that one needs to apply within the processing steps are discussed.

2.2.1 GRACE and GRACE-FO Satellite Gravimetry Missions

GRACE, as a gravity study mission in NASA's Earth System Science Pathfinder (ESSP) program, was a joint US-German partnership between the National Aeronautics and Space Administration (NASA) and the Space Agency of the German Research Center for Aerospace (DLR; Deutsche Forschungsanstalt für Luft- und Raumfahrt). The mission was designed to observe and measure the Earth's gravity field and its temporal variations with unprecedented accuracy.

Although the mission was planned for a nominal lifetime of five years, with the launch on 17 March 2002, it continued its data collection till June 2017 and orbited the Earth until 27 October 2017 when one of its twin spacecrafts ran out of fuel after more than 15 years operating.

The GRACE mission consisted of two near-identical satellites, GRACE-1 and GRACE-2, chasing each other around the Earth and flew $\sim$ 220 km apart in a near-circular polar orbit with an inclination of 89.5° and with non-repeat ground tracks (Tapley et al., 2004b). The spacecrafts started their mission in 2002 with an initial altitude of $\sim$500 km above the Earth that naturally decreased to $\sim$447 km in 2012, $\sim$382 km in 2015, and $\sim$330 km in 2017 (equivalent to a decay of $\sim$30 m/day) due to atmospheric drag, which was the main reason why the ground track did not have a fixed repeat pattern. The orbital period of the mission was 94.5 minutes, i.e. in the orbital track, it took 94.5 minutes for the spacecraft to move around the Earth from pole to pole to complete an orbit.

Within the GRACE satellite-to-satellite tracking geodetic mission, the Earth's gravity field was globally mapped by accurately measuring the separation between the two spacecrafts using a K-Band microwave Ranging (KBR) system. The inter-satellite range was measured with a 5-sec sampling rate and an accuracy of 10 µm by both spacecrafts (Tapley et al., 2004b). The KBR systems on both the lead and the trailing satellites were coupled with GPS receivers to determine the accurate position of the spacecrafts on the orbit to within a centimeter or less, and also to allow time-tagging of all onboard sensors (Dunn et al., 2003). Moreover, in order to validate the position and velocity of satellites (precise orbit determination), both spacecrafts were equipped with Satellite Laser Ranging (SLR) retro-reflectors (Tapley et al., 2004b). In addition, two star cameras were used in each satellite to precisely consider the attitudes of the spacecrafts by tracking them relative to the position of stars (e.g., Inácio et al., 2015). The effect of non-gravitational forces such as those due to atmospheric drag was determined with the precision of 100 µGal (Loomis et al., 2012) by means of the three-axis electrostatic accelerometers that were mounted at each satellite's center of mass so that only gravity effects were considered (Tapley et al., 2004b).

GRACE-FO mission, as the successor to the original GRACE mission, is a collaboration between NASA and the German Research Centre for Geosciences (GFZ; Deutsches GeoForschungsZentrum) that was launched on 22 May 2018. In this mission, the orbital parameters are pretty similar to its predecessor, GRACE, and the pair of almost-identical twin satellites are equipped with the same double-way microwave ranging measurement system as GRACE. However, the advancing technology employed in the production of onboard

sensors and measurement systems makes the observations even more precise. As an experimental instrument, in addition to the improved sensors, an advanced Laser Ranging Interferometry (LRI) system is installed in the GRACE-FO twin spacecrafts to be tested. The laser instrument provides the possibility of more accurate separation distance measurements, which is mainly attributed to the shorter wavelength of light. With a design precision 26 times better than the KBR on GRACE (Tapley et al., 2019), the LRI is a promising improvement to be used operationally for future generations of satellite gravimetry missions (Landerer et al., 2020).

GRACE-FO employs the same strategy to map the Earth's gravity field as GRACE. After removing the effect of non-gravitational forces, the ultra-precise KBR measurements of variations in the inter-satellite separation are translated into changes in the Earth's gravity field, which are attributed to the mass redistribution within the Earth system. The principle of converting the inter-satellite separation measurements into the gravity fields is based on the definition of gravity, which is the attraction between two objects. Figure 4 shows how the inter-satellite separation changes in the GRACE and GRACE-FO missions as the spacecrafts pass from a massive Earth feature to the ocean. In Figure 4a, while both satellites are flying over the ocean, the trailing satellite follows the leading spacecraft with a relatively constant distance of 220 km. As the leading satellite passes over a massive Earth feature, it experiences the effect of the stronger gravity that comes from the greater mass concentration, i.e. the feature's stronger attraction pulls it away from the trailing satellite, which is still flying over the ocean (Figure 4b), and, consequently, the distance between two satellites increases. When the trailing spacecraft encounters the same denser mass, its speed increases as well due to the higher gravity of the mass concentration, resulting in a decrease in the separation between satellites. The distance decreases even more as the first satellite is pulled back by the greater attraction of the feature (Figure 4c). Once both satellites fly over the ocean again (Figure 4d), the distance starts to increasing, because while the leading spacecraft speeds up and escapes the gravity field of the denser mass, the trailing satellite is pulled back under the effect of higher mass concentration. Finally, as the effect of mass on the trailing satellite disappears, it returns to its original distance behind the first satellite. It is worth mentioning that the along track separation between satellites is maintained between 170 to 270 km (220 ± 50 km).

Orbiting the Earth 15 times a day, the twin satellites provide full coverage of the entire globe with a dense ground track of non-repeating orbit within typically 30 days, constructing monthly maps of the regional variations in the

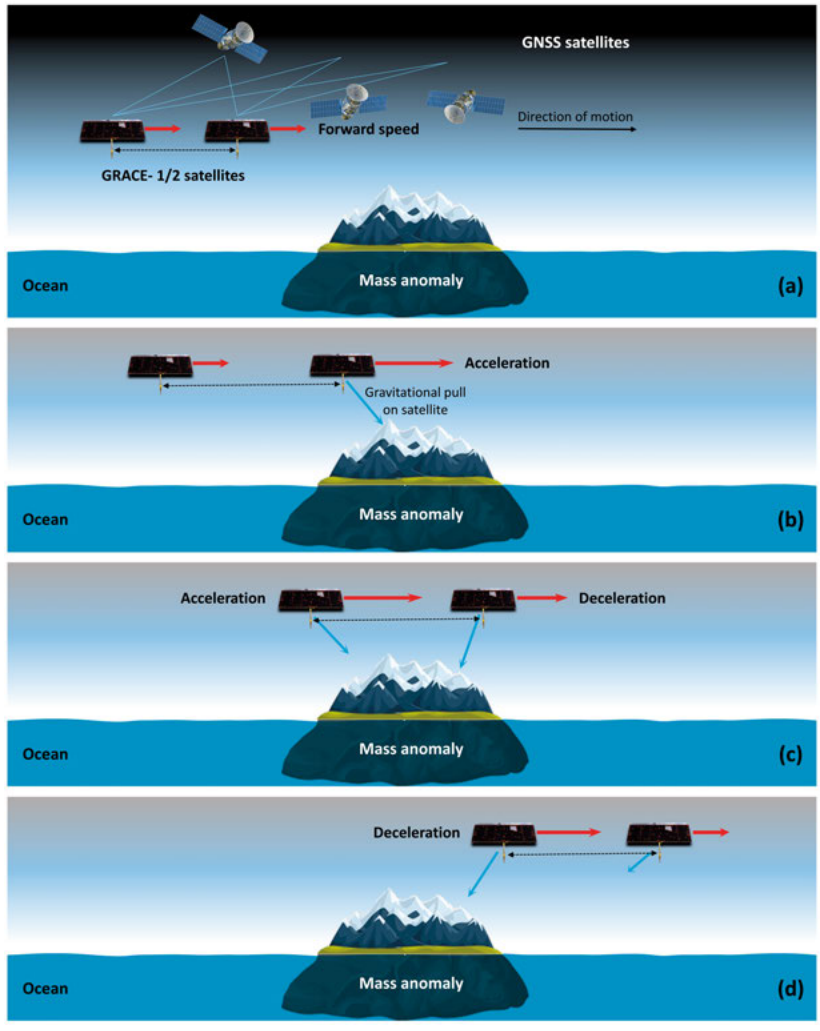

Figure 4. Step-by-step diagram description of how GRACE and GRACE-FO satellites work (not to scale)

global gravity field with a spatial resolution of typically 300 km.

Our complex planet and its gravity field are continually changing. Given the fact that the more mass a feature has, the stronger its gravitational pull, the gravity force changes from one point to another on the Earth's surface. However, due to the movement of mass within the Earth system, this geographically varying gravity is not constant over time and continuously changes with time. Among all contributors to the Earth's gravity field change, water mass plays the main role as it changes daily in the Earth system.

Moving between land, ocean, and atmosphere, water constantly changes its

state (liquid, vapor, and ice), but its mass does not change. As such, tracking the processes that make the water move and change within the Earth system are fundamental for studying the most crucial challenges in climate science. Accordingly, as time-varying gravity observations can detect water mass redistribution, GRACE and GRACE-FO missions play a key role in climate science by providing an integrated picture of how the Earth's hydrological cycle and energy balance are globally evolving. Among others, some scientific applications of GRACE and GRACE-FO missions are in the following fields (e.g., Chen et al., 2022):

- melting ice sheets and glaciers (e.g., Velicogna et al., 2020; Ciracì et al., 2020; Groh and Horwath, 2021),
- changing sea level and ocean dynamics (e.g., WCRP Global Sea Level Budget Group, 2018; Horwath et al., 2022),
- ocean surface and bottom currents, and ocean heat content (e.g., Landerer et al., 2015; Meyssignac et al., 2019),
- ocean bottom pressure (e.g., Poropat et al., 2018),
- storage of water and snow on land including runoff and river basins, Groundwater Storage (GWS), and surface and near-surface water storage (e.g., Sadeghi et al., 2020; Rateb et al., 2020), and
- dry soil and drought (e.g., Zhao et al., 2017).

In addition to tracking water cycle, the GRACE(-FO)-based time-varying gravity observations are used to study the solid Earth as well. In response to the water mass movement on the Earth's surface, the viscous mantle below the crust is constantly moving very slightly (e.g., Shafiei Joud et al., 2017; Wang et al., 2019; Sun and Riva, 2020). Moreover, mass redistribution in the Earth's surface directly changes the planet's rotation in which GRACE(-FO) gravity fields can considerably contribute to estimate the contemporary surface mass load contribution (e.g., Adhikari and Ivins, 2016; Seo et al., 2021). More recently, GRACE and GRACE-FO observations were used to detect transient ocean mass redistribution propagating as tsunamis triggered by great earthquakes (Ghobadi-Far et al., 2020), in which due to the transient nature of the phenomenon, it is not possible to detect tsunamis by monthly gravity fields and one may need to directly analyze the inter-satellite distance data measured by the KBR system. Another scientific goal of the GRACE and GRACE-FO missions is to contribute to monitoring and forecasting weather by providing better profiles of the Earth's atmosphere. In this regard, each of the twin satellites utilizes its GPS receivers and special antennas to supply profiles of atmospheric temperature and humidity, and water vapor content.

2.2.2 GRACE and GRACE-FO Data Products

In the GRACE and GRACE-FO missions, data from the science instruments and subsystems onboard include satellites position and velocity obtained by the GPS receivers, inter-satellite separation measured by the KBR system, non-gravitational accelerations measured by the SuperSTAR accelerometers, and attitude observations detected by star cameras. In general, all data are gathered onboard continuously throughout the mission, except for the GPS radio occultation data that will be collected to supply atmospheric profiles per day (Bettadpur, 2012). The collected data go through some processing steps, in which each step results in specific data product. Generally, the processing results are categorized and released in five different data products, namely Level-0, Level-1A, Level-1B, Level-2, and Level-3.

***Level-0 data products*:** The Level-0 data products are the raw instrument data that are gathered onboard and transmitted to the GRACE raw data center and are down-linked by the satellites to the center. In this way, there are two files from each satellite (data from each down-link pass are divided into the science instrument and spacecraft housekeeping data streams) that are labeled as Level-0 data products, which contain, in addition to the description headers, the unscaled binary encoded instrument data.

***Level-1A data products*:** The Level-1A data products are resulted from applying a non-destructive processing to the previously obtained unscaled binary Level-0 products. In this context, the binary encoded data are translated to the actual meaningful units using the sensor calibration factors, are time-tagged using the corresponding satellite receiver clock, and are labeled with quality control flags.

***Level-1B data products*:** The Level-1B data products are achieved through applying a destructive processing to the previously generated Level-1A products. In this processing, Level-1A products are transformed to a common reference frame and data sample rate (temporal resolution) is reduced through filtering. The data include the inter-satellite range observations and their first and second time derivatives, the non-gravitational accelerations, the orbit measurements from GPS, and attitude observations.

***Level-2 data products*:** The Level-2 data products, which are resulted from applying Level-2 processing on one month of the pre-processed Level-1B data products, include global monthly-mean gravity field solutions provided in the form of SHCs. During Level-2 processing, some ancillary data products are also generated, which are also released with the Level-2 label. Different GRACE data processing centers provide monthly Level-2 data products. Among all, three institutions officially release the data: (1) NASA Jet Propulsion

Laboratory (JPL), (2) the German Research Centre for Geosciences (GFZ), and (3) the Center for Space Research (CSR) at the University of Texas at Austin. Both GRACE and GRACE-FO Level-2 gravity field solutions processed by the aforementioned centers can be obtained from `https://podaac-tools.jpl.nasa.gov/drive/files/allData`. In addition to the official Science Data System (SDS) centers, other processing groups also process and provide monthly Level-2 gravity fields, e.g., Institute of Geodesy at Graz University of Technology (ITSG) and Leibniz Universität Hannover (LUH). One can find detailed information about the processing centers at International Centre for Global Earth Models (ICGEM; `http://icgem.gfz-potsdam.de/series`).

***Level-3 data products*:** The Level-3 data products are generated by applying various processing steps on either Level-2 products or Level-1B data, where the latter is termed as Mass concentration (Mascon) approach. As discussed in Section 2.2.3, an analytical model and some certain processing steps are required, which mainly deal with reducing the effect of Level-2 data errors, to convert the Level-2 data into meaningful monthly maps of surface mass densities. The result of applying those processing steps along with an analytical model on the monthly gravity solutions is termed as the Level-3 data products, which are usually released in the form of monthly gridded maps of surface mass change expressed in terms of Equivalent Water Height (EWH) relative to a time-mean. Institute of Geodesy and Geoinformation (IGG) at the University of Bonn (`https://www.apmg.uni-bonn.de/daten-und-modelle/grace_level3_monthly_solutions`), European Gravity Service for Improved Emergency Management (EGSIEM; `http://egsiem.eu/tools`), and JPL (under GRACE TELLUS; `https://grace.jpl.nasa.gov/data/monthly-mass-grids/`) are some of the processing centers providing Level-3 data grids of monthly surface mass changes. In addition to the Level-2 data, the Level-1B products can also be utilized directly to determine the Level-3 monthly maps of EWH, referred to as Level-3 Mascon data products. Mascon blocks are native basis functions of the gravity field with identified geophysical locations to which KBR separation observations are fit. In this approach, since a location is assigned to each Mascon, unlike the location-independent SHCs, geophysical constraints can be applied easily during the data inversion. In this way, the apriori constraints offer canceling out correlated noise, which is needed to be filtered out using post-processing filtering while analyzing Level-2 data to produce monthly surface mass changes (discussed in Section 2.2.3.2), and it is required to use destriping or smoothing techniques to the constrained Mascon solutions (e.g., Watkins et al., 2015). JPL (`https:`

//grace.jpl.nasa.gov/data/get-data/jpl_global_mascons/) and NASA's Goddard Space Flight Center (GSFC; https://earth.gsfc.nasa.gov/geo/data/grace-mascons) are two centers for analyzing and providing Level-3 Mascon solutions.

2.2.3 From Time-Variable Geopotential Coefficients to Surface Mass Change Anomalies

The sequential monthly gravity field solutions (Level-2 products) can be used in analytical models to reveal the long-term and seasonal mass change signals within the Earth system (e.g., Tapley et al., 2004a,b). Within this frame, as explained in Section 2.2.2, the Level-2 data need to be mapped into the Level-3 monthly maps of surface mass density. This process involves the converting of the Level-2 products from the spherical harmonic domain into a georeferenced grid, usually a global regular grid with a 1° spatial resolution.

In general, the problem of extracting the Earth's mass density variations from time-varying gravity solutions is an inverse problem that does not have a unique solution. However, based on considering some assumptions, different approximations can be found leading to a unique solution of mass change detection at the Earth's surface. Since the launch of GRACE twin spacecrafts, the spherical approximation of Wahr et al. (1998) has typically been employed as the common analytical method to infer surface mass changes from the time-varying gravity solutions. According to this spherical approach, the Earth's surface mass density redistribution, $\Delta\sigma$, can be estimated from the Level-2 data as (Wahr et al., 1998):

$$\begin{aligned}\Delta\sigma(\theta,\lambda) = \frac{R\rho_{\text{ave}}}{3}\sum_{n=0}^{\infty}\sum_{m=0}^{n}\left(\frac{2n+1}{1+k_n}\right) \\ \times(\Delta C_{nm}\cos m\lambda + \Delta S_{nm}\sin m\lambda)\bar{P}_{nm}(\cos\theta),\end{aligned} \tag{2.18}$$

where (θ,λ) is the geocentric spherical coordinate, R denotes the mean radius of the Earth, ρ_{ave} is the Earth's average mass density, n/m is the degree/order of the SHCs, k_n represents the degree-dependent load Love numbers accounting for the deformation of the solid Earth (Farrell, 1972), $(\Delta C_{nm}, \Delta S_{nm})$ are the temporal variations in the fully-normalized SHCs of the Earth's gravitational field relative to a temporal mean value of SHCs, and $\bar{P}_{nm}$ is the fully-normalized associated Legendre functions. Accordingly, assuming that the surface mass density results just from variations in water mass, the surface mass density

variations can be converted to EWH changes as follows:

$$\Delta h_w(\theta,\lambda) = \frac{R\rho_{\text{ave}}}{3\rho_w}\sum_{n=0}^{\infty}\sum_{m=0}^{n}\left(\frac{2n+1}{1+k_n}\right) \times (\Delta C_{nm}\cos m\lambda + \Delta S_{nm}\sin m\lambda)\,\bar{P}_{nm}(\cos\theta), \tag{2.19}$$

where ρ_w is the mass density of water. A certain set of assumptions have been considered to form this spherical approximation for globally extracting the Earth's mass variations from the Level-2 data: (1) the mass variations mostly occur within the Earth's relatively thin fluid envelope, (2) the Earth's topography is negligible, and (3) the Earth has a spherical shape.

Chao (2016) challenged some fundamental assumptions underpinning the common analytical solution and issued specific caveats on the indiscriminate utilization of such a common solution. Thereafter, Li et al. (2017) discussed that using the common spherical approximation for inferring surface mass changes from time-varying SHCs results in a systematic bias, especially for polar regions where the spherical approximation leads to systematic underestimation. Accordingly, since an ellipsoid better represents the Earth's shape, they recommended an ellipsoidal correction to be considered for more precise mass recovery with GRACE SHCs.

Studying the effect of considering an ellipsoid rather than a sphere as the Earth's shape, Ditmar (2018) suggested a modified technique for converting Level-2 data into the Earth's surface mass variations, based on the assumptions that: 1) mass transport occurs at the reference ellipsoid, and 2) at each point on the ellipsoid, the ellipsoidal surface is approximated by a sphere with a radius equal to the current radial distance from the center of the Earth. Ditmar (2018) showed that one may not easily ignore the difference between the estimated mass variations based on spherical and ellipsoidal coordinates, and, therefore, a conversion of geodetic co-latitudes into geocentric ones should be taken into account. Following this, Ghobadi-Far et al. (2019) assumed that: (1) mass variations occur within the Earth's surface, (2) the Earth's topography is negligible, and (3) the Earth has an ellipsoidal shape, and proposed the ellipsoidal version of the common spherical approximation based on converting the SHCs into the Ellipsoidal Harmonic Coefficients (EHCs) using the linear transformation introduced by Jekeli (1988). The theory of this ellipsoidal approximation is developed, similar to Wahr et al. (1998), based on a one-to-one linear relation between the harmonic coefficients of surface mass change and the Earth's gravitational potential. According to this ellipsoidal approximation, the surface mass density changes can be estimated by the following ellipsoidal

harmonic expansion (Ghobadi-Far et al., 2019):

$$\Delta\sigma_E(\beta,\lambda) = \frac{ab\rho_{ave}}{3L_b(\beta)} \sum_{n=0}^{\infty}\sum_{m=0}^{n} \left(\frac{2n+1}{(1+k_{nm}^E)\,T_{nm}^{a,b}}\right) \times \left(\Delta C_{nm}^E \cos m\lambda + \Delta S_{nm}^E \sin m\lambda\right) \bar{P}_{nm}(\cos\theta), \tag{2.20}$$

where β is the reduced latitude, a and b are the semi-major and semi-minor axes of the reference ellipsoid, $L_b(\beta) = \sqrt{b^2+\varepsilon^2 sin^2\beta}$, $\varepsilon = \sqrt{a^2-b^2}$, k_{nm}^E denotes the load Love number coefficients associated with an ellipsoidal Earth model, $(\Delta C_{nm}^E, \Delta S_{nm}^E)$ represents the variation in the EHCs of the Earth's gravitational field, and $T_{nm}^{a,b}$ is an auxiliary function used for brevity. If it is assumed that the surface mass density results only from redistribution of water mass, then, the ellipsoidal-based EWH can be estimated as $\Delta h_w^E = \frac{1}{\rho_w}\Delta\sigma_E$.

Regardless of using spherical, ellipsoidal, or any other analytical solutions for the problem of mass change detection at the Earth's surface from the observed variations in the Earth's gravitational field (Level-2 products), GRACE(-FO)-derived time-varying gravity solutions are subject to a number of errors that are required to be taken into account appropriately to arrive at accurate estimates of the Earth's surface mass change. In the following, those issues are discussed.

2.2.3.1 Low-Degree GRACE(-FO) Stokes Coefficients

***Degree-1 coefficients*:** The GRACE(-FO) Level-2 products are made available in a reference frame with its origin at the Center of Mass (CM) of the Earth system (geocenter), not Center of Figure (CF). Therefore, SHCs of degree 1 (ΔC_{10}, ΔC_{11}, and ΔS_{11}), which represent the position of the Earth's instantaneous geocenter relative to its center of figure (origin of an Earth-fixed reference frame) (Crétaux et al., 2002), cannot be retrieved by GRACE(-FO). Accordingly, since the Earth's geocenter undergoes periodic variations that are, on seasonal timescales, mainly due to the movement of water mass within the Earth system (Crétaux et al., 2002), and represent a significant recovered mass variations (Chambers, 2006), GRACE(-FO)-based degree-1 coefficients need to be replaced by those provided by auxiliary models.

Based on external observations, various strategies have been proposed to correct Level-2 SHCs for the Earth's geocenter motion while studying mass transportation within the Earth's surface (e.g., SLR, GPS, modeled Ocean Bottom Pressure (OBP), or a combination of them). The following equation can be used to directly convert geocenter fluctuations to normalized degree-1

gravity coefficients (e.g., Swenson et al., 2008):

$$\begin{Bmatrix} C_{11}(t) \\ S_{11}(t) \\ C_{10}(t) \end{Bmatrix} = \frac{1}{\sqrt{3}R} \begin{Bmatrix} X_g(t) \\ Y_g(t) \\ Z_g(t) \end{Bmatrix}, \tag{2.21}$$

where $(X_g(t), Y_g(t), Z_g(t))$ is the Cartesian coordinate of the geocenter in the terrestrial reference frame (a reference frame attached to the solid Earth) and R represents the Earth's mean radius. Figure 5 shows the fluctuations of the instantaneous Earth's center of mass relative to the reference axis center based on the SLR observations provided by CSR (`http://download.csr.utexas.edu/pub/slr/geocenter/`). However, relying on a method based on ocean and atmospheric models and GRACE(-FO) coefficients for degrees 2 and higher (Swenson et al., 2008; Sun et al., 2016), each official processing center releases monthly estimates of degree-1 gravity coefficients along with providing Level-2 data products (GRACE Technical Note TN-13; `https://podaac.jpl.nasa.gov/gravity/gracefo-documentation`), which are recommended by GRACE SDS to be used.

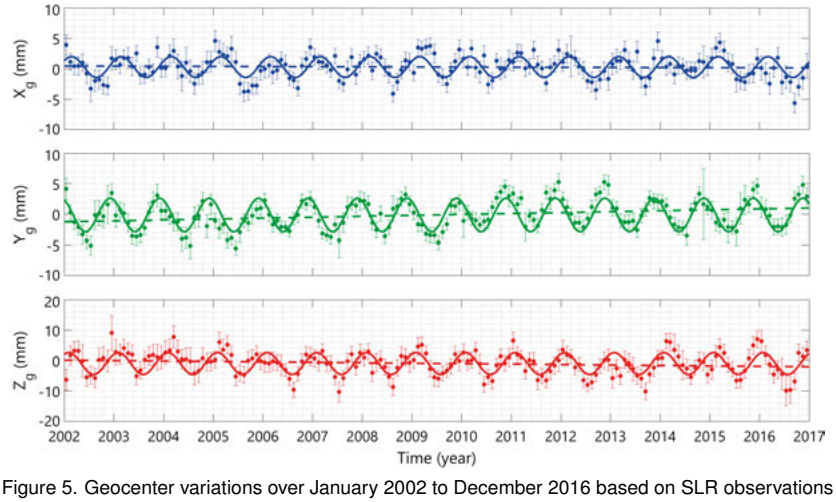

Figure 5. Geocenter variations over January 2002 to December 2016 based on SLR observations provided by CSR data center. Monthly values are shown by dots with error bars representing the standard deviation. Dashed and solid lines indicate linear trend and Fourier fitted curves, respectively

It is worth mentioning that although different observations and techniques provide different geocenter solutions at the few mm level, when accounting for water mass movement studies the error in the solution is considerably less than the error in ignoring geocenter motion.

***Degree-2 zonal coefficients*:** The spherical harmonic of degree 2 and order

0, C_{20}, is related to the flattening of the Earth (Earth's dynamic oblateness). Analysis of SLR data has revealed a significant time variation in the C_{20} gravity coefficient (e.g., Cheng and Tapley, 2004), which is due to the mass transportation within the Earth's dynamic system, and especially water mass variations (e.g., Cheng and Tapley, 2004). However, Chen et al. (2004) reported that GRACE-based C_{20} coefficients show considerably higher variability than the Earth Orientation Parameters (EOP; polar motion and length of day) and climate model estimates, and Chen et al. (2005) showed that the EOP-derived results agree well with the SLR-based observation of low degree gravity changes. The relatively large uncertainty in the GRACE(-FO)-based C_{20} coefficients is mainly attributed to the orbital geometry of GRACE(-FO) twin satellites and tidal error (Chen, 2019). Therefore, since SLR observations result in more accurate low degree coefficients, GRACE(-FO)-based C_{20} coefficients need to be replaced by those introduced by SLR solutions.

Similar to degree-1 coefficients, monthly estimates of C_{20} coefficients are also released by the official processing centers (GRACE Technical Note TN-11) along with the Level-2 data products. These estimates are obtained from the analysis of SLR data to five geodetic satellites LAGEOS-1 and 2, Starlette, Stella, and Ajisai. In addition, a new time series of SLR-based C_{20} coefficients is provided by GSFC under GRACE Technical Note TN-14 (`https://podaac.jpl.nasa.gov/gravity/gracefo-documentation`). This new standard oblateness solution utilizes a time-variable gravity background model (Loomis et al., 2019), while the earlier C_{20} harmonic solutions provided by the previous GRACE technical notes used a fixed background model (Cheng and Ries, 2017). Figure 6 depicts the variations in C_{20} from SLR observations (GRACE TN-11) and GRACE monthly solutions (CSR Release 06; RL06) over the period of GRACE mission. The unexpectedly

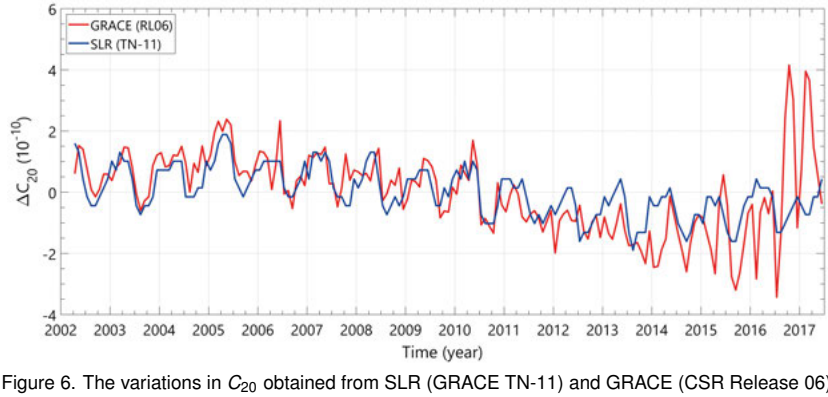

Figure 6. The variations in C_{20} obtained from SLR (GRACE TN-11) and GRACE (CSR Release 06). A mean value is subtracted from each time series

large fluctuation in GRACE time series after 2015 are associated to the high level of noise in GRACE solutions due to the degradation of the satellites as they came towards the end of their mission (WCRP Global Sea Level Budget Group, 2018).

***Degree-3 zonal coefficients*:** Loomis et al. (2020) showed that while GRACE(-FO) mission is not operating with both accelerometers, C_{30} coefficient is also subject to large uncertainty. The GRACE twin satellites continued to observe the Earth nominally until October 2016 when the accelerometer aboard GRACE-2 had been switched off to save battery power (thereafter, data processing strategies were developed to retrieve the missing information, and non-gravitational accelerations measured onboard GRACE-1, thereby, were transplanted to GRACE-2, e.g., see Bandikova et al. (2019)). In addition, in the GRACE-FO mission, the data of one of the accelerometers degraded after operating one month in orbit, and the data are not included in the processing due to elevated noise levels. Therefore, SDS recommends replacing the native GRACE-FO C_{30} coefficients with those estimated based on SLR observations provided in the GRACE-FO Technical Note TN-14. For the GRACE data as well, it is recommended to replace C_{30} coefficients with the time series from August 2016 (Loomis et al., 2020). Figure 7 compares the GRACE-FO- and SLR-based time series of C_{30} from GRACE-FO monthly solutions and GRACE-FO TN-14, respectively, over 2018.06 to 2021.07.

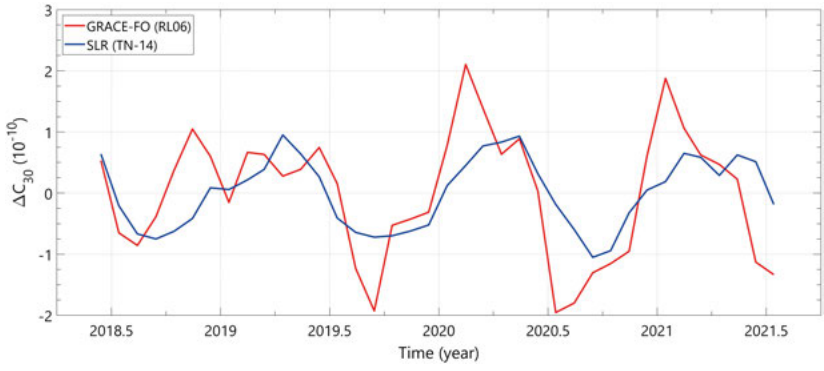

Figure 7. The variations in C_{30} obtained from SLR (GRACE-FO TN-14) and GRACE-FO (CSR Release 06). A mean value is subtracted from each time series

2.2.3.2 Smoothing and Destriping

Spatial averaging, or smoothing, of GRACE(-FO) Level-2 products is essential to minimize the contribution of noisy high-degree Stokes coefficients in recovering the Earth's gravity field, i.e. the contribution of noisy short-wavelength components of the gravity field solutions. However, apart

from suppressing the effects of GRACE(-FO) observational errors, spatially correlated errors in GRACE(-FO) solutions are also required to be suppressed. Because of the observation geometry with its pure along-track ranging on near-polar orbits, GRACE(-FO) gravity fields divulge extremely anisotropic error characteristics. Swenson and Wahr (2006) showed that the spatially correlated errors, which especially present at shorter wavelengths (higher degrees of SHCs), manifest themselves in the form of north-south long, linear features in the grids of surface mass changes. They concluded that these spatially correlated patterns, often referred to as "stripes", imply corresponding correlations in the spectral domain, and revealed that for a specific order (higher than 8) there are evident correlations as a function of degree where the pattern alternates with even and odd degrees, i.e. even and odd coefficients do not seem correlated with one another (see Figure 2 in Swenson and Wahr (2006)). Seo et al. (2008) explain that this pattern is mainly attributed to the aliasing of mismodeled atmospheric and oceanic pressure fields (non-tidal geophysical signal). Save (2009, p. 48) discusses that the ill-posed nature of the least-squares estimation problem accounts for part of this pattern as well. In a more recent study, Peidou and Pagiatakis (2020) claim to find the source of longitudinal stripes on the gravity fields. They analyzed the spatiotemporal structure of latitudinal stripe profiles and reported that the stripes are resulted from the oversampling of the Earth's low-frequency geoid along the parallels of latitude. In other words, the low latitudinal frequency geoid modulates the total sampled gravitational signal, and the stripes arise from the amplitude of that modulation (Peidou and Pagiatakis, 2020).

In the context of Stokes coefficients errors, many post-processing filtering techniques have been developed and applied since the launch of GRACE twin satellites to reduce the effect of errors, e.g., optimized smoothing approaches (Chen et al., 2006b), Wiener optimal filtering (Sasgen et al., 2006), statistical filtering methods (Davis et al., 2008), localized basis functions (Schmidt et al., 2007), correlated-error filters (Swenson and Wahr, 2006), Empirical Orthogonal Functions (EOF) (Schrama et al., 2007; Wouters and Schrama, 2007), anisotropic filters (Han et al., 2005; Kusche, 2007; Zhang et al., 2009), Independent Component Analysis (ICA) (Frappart et al., 2011), and Tikhonov regularization strategy (Save et al., 2012). Some of the proposed filters are fixed-parameter filters, such as Gaussian smoothing function (Jekeli, 1981; Wahr et al., 1998) that applies equally to all orders at each degree, and some are data-adaptive filters that use geophysical models or GRACE observations to judge noise and signal levels, such as the filtering techniques proposed by Klees et al. (2008) and Crowley and Huang (2020). Generally speaking, smoothing

and destriping filters can be employed in either spatial or spectral domain to suppress the impact of SHCs noise in estimating the Earth's surface mass variations.

In this thesis, conventional Gaussian spatial smoothing function, anisotropic DDK filters (Kusche, 2007; Kusche et al., 2009), and Kernel Fourier Integration (KeFIn) filter (Khaki et al., 2018) are utilized. With the two-point smoothing kernel $W(\theta,\lambda,\theta',\lambda')$, the smoothed surface mass density can be obtained by convolving $\Delta\sigma$ against W, presented in the spatial domain as (e.g., Wahr et al., 1998; Kusche et al., 2011):

$$\Delta\sigma^{W}(\theta,\lambda)=\int \sin\theta' d\theta' d\lambda' \Delta\sigma\left(\theta',\lambda'\right) W\left(\theta,\lambda,\theta',\lambda'\right), \tag{2.22}$$

where $\Delta\sigma(\theta',\lambda')$ can be estimated using GRACE(-FO) Stokes coefficients. By substituting Eq. 2.18 in the above equation, the smoothed field in the spectral domain is obtained as:

$$\begin{aligned}\Delta\sigma^{W}(\theta,\lambda)=\frac{R\rho_{\text{ave}}}{3}\sum_{n=0}^{\infty}\sum_{m=0}^{n}\left(\frac{2n+1}{1+k_n}\right)\bar{P}_{nm}(\cos\theta)\sum_{n'=0}^{\infty}\sum_{m'=0}^{n'}\\ \left[\left(\Delta C_{n'm'}W_{nmc}^{n'm'c}+\Delta S_{n'm'}W_{nmc}^{n'm's}\right)\cos m\lambda\right.\\ \left.+\left(\Delta C_{n'm'}W_{nms}^{n'm'c}+\Delta S_{n'm'}W_{nms}^{n'm's}\right)\sin m\lambda\right],\end{aligned} \tag{2.23}$$

where

$$\begin{aligned}\begin{Bmatrix} W_{nmc}^{n'm'c}\\ W_{nms}^{n'm'c}\\ W_{nmc}^{n'm's}\\ W_{nms}^{n'm's}\end{Bmatrix}=\int\sin\theta d\theta d\lambda\int\sin\theta' d\theta' d\lambda'\begin{Bmatrix}\cos m'\lambda'\cos m\lambda\\ \cos m'\lambda'\sin m\lambda\\ \sin m'\lambda'\cos m\lambda\\ \sin m'\lambda'\sin m\lambda\end{Bmatrix}\\ \times W(\theta,\lambda,\theta',\lambda')\bar{P}_{nm}(\cos\theta)\bar{P}_{n'm'}(\cos\theta').\end{aligned} \tag{2.24}$$

Accordingly, by defining the smoothed coefficients as:

$$\Delta C_{nm}^{W}=\sum_{n'=0}^{\infty}\sum_{m'=0}^{n'}\left(\Delta C_{n'm'}W_{nmc}^{n'm'c}+\Delta S_{n'm'}W_{nmc}^{n'm's}\right) \tag{2.25}$$

$$\Delta S_{nm}^{W}=\sum_{n'=0}^{\infty}\sum_{m'=0}^{n'}\left(\Delta C_{n'm'}W_{nms}^{n'm'c}+\Delta S_{n'm'}W_{nms}^{n'm's}\right), \tag{2.26}$$

the smoothed form of Eq. 2.18 is presented as:

$$\Delta\sigma^{W}(\theta,\lambda) = \frac{R\rho_{\text{ave}}}{3}\sum_{n=0}^{\infty}\sum_{m=0}^{n}\left(\frac{2n+1}{1+k_n}\right) \times \left(\Delta C^{W}_{nm}\cos m\lambda + \Delta S^{W}_{nm}\sin m\lambda\right)\bar{P}_{nm}(\cos\theta). \tag{2.27}$$

With the same formulation, Jekeli (1981) developed the idea of spatial averaging to suppress the effect of noise in poorly known, short-wavelength (high-degree) SHCs. Along with this idea, he introduced his normalized isotropic Gaussian averaging function, popularized by Wahr et al. (1998), as:

$$W(\psi) = \frac{b}{2\pi}\frac{e^{-b(1-\cos\psi)}}{1-e^{-2b}}, \tag{2.28}$$

with

$$b = \frac{\ln(2)}{(1-\cos(r/R))}. \tag{2.29}$$

Here, $r = R\psi$ is the distance on the Earth's surface, referred to as averaging radius, in which the kernel drops to $1/2$ its power at $\psi = 0$ (ψ is the spherical distance between two points (θ,λ) and (θ',λ')) (Wahr et al., 1998). The Legendre coefficients W_n can be computed with recursion relations as follows (Jekeli, 1981, Eq. 63):

$$W_0 = 1, \qquad W_1 = \left[\frac{1+e^{-2b}}{1-e^{-2b}} - \frac{1}{b}\right], \qquad W_{n+1} = -\frac{2n+1}{b}W_n + W_{n-1}, \tag{2.30}$$

Provided that the error characteristics are random, this filter suppresses signals with a wavelength shorter than $2r$. In other words, in this filter, the contribution of higher frequencies reduces with increasing the averaging radius. This fact can be seen in Figure 8 where the Legendre coefficients of this filter are plotted for different averaging radii.

As mentioned earlier, the Gaussian averaging function is an isotropic filter, i.e. the smoothing kernel depends only on the spherical distance ψ between two points (θ,λ) and (θ',λ') and not on their relative orientation, implying that the spherical harmonics of the kernel can be reduced to the Legendre coefficients of a zonal function (Kusche et al., 2011). In other words, in isotropic filters the smoothing kernel is only degree-dependent (it can be seen in Eq. 2.30). Therefore, in the case of using Gaussian spatial smoothing function, in Eq. 2.23, $W^{n'm'c}_{nm} = W^{n'm's}_{nm} = W_n$. Accordingly, Eq. 2.23 can be rewritten as (e.g.,

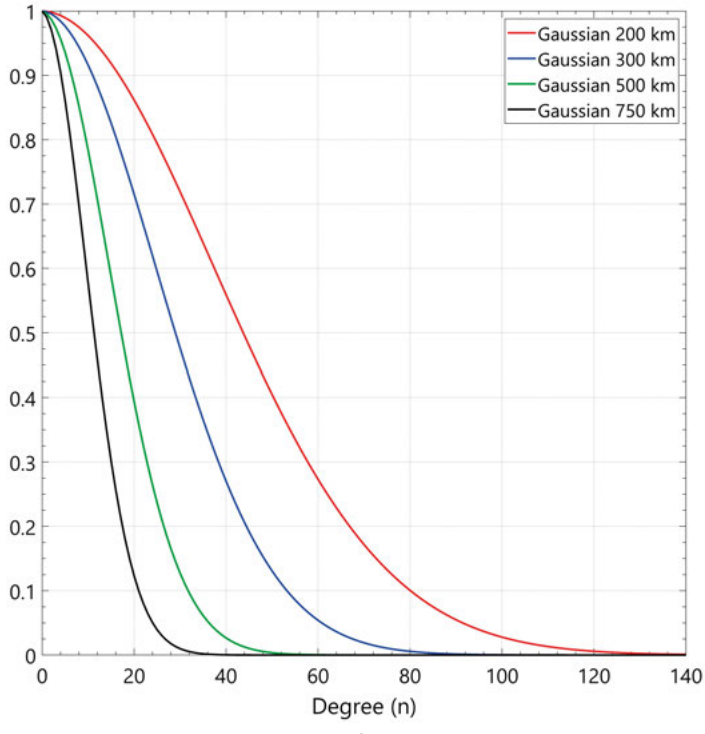

Figure 8. The frequency response of isotropic Gaussian spatial smoothing function in different averaging distances

Chambers, 2006):

$$\Delta\sigma^{W}(\theta,\lambda) = \frac{R\rho_{\text{ave}}}{3}\sum_{n=0}^{\infty}\sum_{m=0}^{n}\left(\frac{2n+1}{1+k_n}\right)W_n \times (\Delta C_{nm}\cos m\lambda + \Delta S_{nm}\sin m\lambda)\,\bar{P}_{nm}(\cos\theta). \tag{2.31}$$

In addition to the Gaussian spatial smoothing function, anisotropic DDK filters introduced by Kusche (2007) are utilized in this thesis as well. In this method, the filter matrix is obtained by regularization of a normal equation system that involves an apriori synthetic model of the geometry. In other words, this technique is based on a least-squares estimation of the Stokes coefficients using the KBR range measurements along with orbital data (observation vector). Accordingly, the SHCs can be estimated as:

$$\hat{\mathbf{x}} = \mathbf{N}^{-1}\mathbf{b}, \tag{2.32}$$

where $\mathbf{N}$ is the normal matrix of equations and $\mathbf{b}$ is the observation vector. If $\mathbf{M}^{-1}$ is considered to be an approximation to the signal covariance, $\mathbf{C_x} =$

$E\left\{\mathbf{x}\mathbf{x}^T\right\}$, and $\mathbf{N}^{-1}$ is apriori GRACE error covariance, $\mathbf{C}_{\hat{\mathbf{x}}} = E\left\{\hat{\mathbf{x}}\hat{\mathbf{x}}^T\right\}$, thus, the regularized SHCs can be estimated as:

$$\hat{\mathbf{x}}_{(\alpha)} = (\mathbf{N} + \alpha\mathbf{M})^{-1}\mathbf{b} = (\mathbf{N} + \alpha\mathbf{M})^{-1}\mathbf{N}\hat{\mathbf{x}}, \tag{2.33}$$

with $\mathbf{W}_{(\alpha)} = (\mathbf{N} + \alpha\mathbf{M})^{-1}\mathbf{N}$ defined as the anisotropic DDK filter. Therefore, the smoothed SHCs can be estimated as:

$$\hat{\mathbf{x}}_{(\alpha)} = \mathbf{W}_{(\alpha)}\hat{\mathbf{x}}, \tag{2.34}$$

where α is a damping parameter (smoothing power) that controls the degree of smoothing in the filter, and is defined by the weight of the covariances and the power law within the signal covariance (Kusche, 2007, Eqs. 45, 47, 48). Therefore, it is vital to obtain a proper estimate of the noise and signal covariance matrices. Kusche (2007) proposed to estimate the GRACE error covariance by using the orbital characteristics of the mission, and assumed that, given that the GRACE satellite velocities are perfectly known (that is surely not true), the error in the monthly fields arises only from the error in the observed potential difference between two satellites. In this case, the correlation in the errors of SHCs is not completely modeled. However, as this filter takes into account the north-south correlation of the fields, it suppresses the stripes more effectively than the isotropic Gaussian filter and is much less likely to bias the data. Kusche (2007) showed that instead of estimating the GRACE error covariance for each month separately, it can be computed for one month and used for all months without drastically changing the results.

Figure 9 shows the performance of different filters in effectively removing noise and, at the same time, retaining geophysical signals, for the example of a single monthly GRACE solution (October 2010).

In this thesis, in addition to the conventional Gaussian spatial smoothing function and anisotropic DDK filters, KeFIn filter proposed by Khaki et al. (2018) is used as well to reduce noise (correlated/colored) in GRACE(-FO) data. The proposed filtering technique also accounts for signal attenuation and leakage error arising from smoothing. This filter works through a two-step consecutive scheme, in which the first step reduces the measurement noise and the aliasing of unmodeled high-frequency mass variations, and the second phase decreases the leakage error using an efficient anisotropic kernel (Khaki et al., 2018). To maintain the integrity of the presentation, this filtering technique is presented in the following section after discussing the leakage problem.

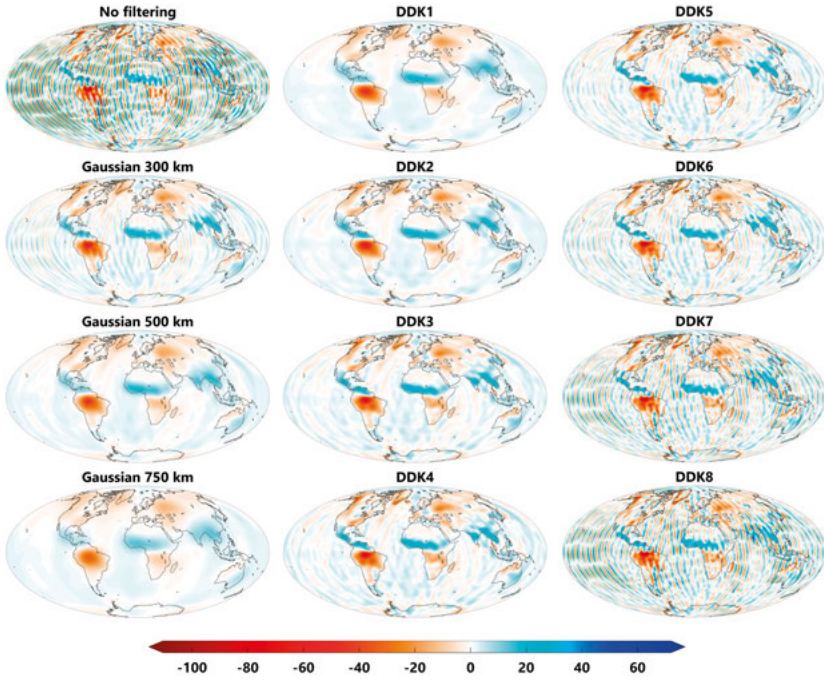

Figure 9. Monthly GRACE solution as of October 2010 from CSR processing center expanded up to degree 60 (top left). Different filters have been applied: Gaussian averaging function with 300, 500, and 750 km half width, and DDK1 to DDK8 filters. [Units: cm water equivalent]

2.2.3.3 Leakage Problem

Since small-scale surface mass variations are attenuated at orbital altitude, therefore, monthly gravity fields are typically estimated up to a limited degree and order. Accordingly, the Stokes coefficients are not able to recover surface mass variations of high spatial resolution. In other words, the spatial resolution of the gravity fields (the scale of the smallest feature of the gravity field that can be resolved using Stokes coefficients) is restricted by the maximum degree and order to which the monthly solutions are presented. In this regard, the maximum degree n_{max} corresponds to a spatial resolution on the Earth's surface of $\pi R/n_{max} \approx 20,000/n_{max}$ (e.g., Velicogna and Wahr, 2013), where R is the Earth radius. For instance, with an $n_{max} = 60$, the shortest resolvable wavelength at the Earth's surface is $\sim$300 km and gravity solutions will only recover wavelengths longer than that.

As the spatial resolution of the GRACE(-FO)-derived solutions is limited, small-scale mass change signals, with spatial variability of less than a few hundred kilometers, do not exist in the mapped surface mass changes. This, therefore, makes it challenging to quantitatively interpret nearby mass changes in contiguous regions, for instance, between the ocean and ice-covered land

areas. This limited spatial resolution due to the spherical harmonic truncation results in an error termed as "spectral leakage error". In addition to the limited range of SHCs available (limited spatial resolution), leakage error also originates from applying filtering techniques required to suppress increasing noise with increasing spherical harmonic degree, referred to as "spatial leakage error", in such a way that using a filter with a large smoothing radius leads to more mass signal distortion. From this, reliable estimates of mass variations require a suitable trade-off between GRACE(-FO) noise reduction and minimum leakage error, which can be fulfilled by means of a proper filtering strategy.

In the spatial domain, leakage typically manifests as signals spreading spatially, especially around land areas with high signal amplitude, thus not being concentrated completely in the region where it originates, but also leaks into surrounding areas. This type of leakage is termed "leakage-out". On the contrary, the "leakage-in" error is defined as the signal in the surrounding region leaking into the area of interest. Leakage is especially troublesome when quantifying ice-sheet mass changes and variations in mountain glacier mass because these are mostly in highly localized areas close to outlet glaciers, and usually along the coast, where signal leaks into adjacent oceans (Chen et al., 2015). Accordingly, leakage causes attenuation of signal amplitudes (e.g., Baur et al., 2009; Chen et al., 2015; Mu et al., 2017), and ignoring it can introduce substantial biases, overestimation or underestimation, in the estimates of surface mass changes (e.g., Guo et al., 2010; Landerer and Swenson, 2012). Therefore, an appropriate leakage correction strategy is needed to be employed to address the problem of leakage error introduced both by spherical harmonic truncation (restricted spectral resolution) and imperfect suppression of satellite measurement errors, and, thereby, to infer unbiased changes in surface mass (e.g., Chambers and Bonin, 2012; Chen et al., 2015).

Figure 10 shows the behavior of both spectral and spatial leakage error over Greenland caused by truncation and spatial filtering. First, a synthetic mass rate model is constructed over a $1^\circ \times 1^\circ$ grid for Greenland in such a way that the mass loss signal is uniformly distributed around the coast from north-west to east, and mass rates for other regions are zero (Figure 10a). Then, the synthetic mass loss rates are converted into the SHCs of mass change up to degree/order 180/180 (e.g., Heiskanen and Moritz, 1967, p. 31). In the next step, the achieved synthetic SHCs are used up to $n_{max} = 60$ to reestimate the mass change rates at any grid point. The results from this truncated expansion are illustrated in Figure 10b. As can be seen, the rates are significantly attenuated relative to the original synthetic model. Figures 10c and d are created with the same processing as Figure 10b is, with the difference that a Gaussian averaging function with 300

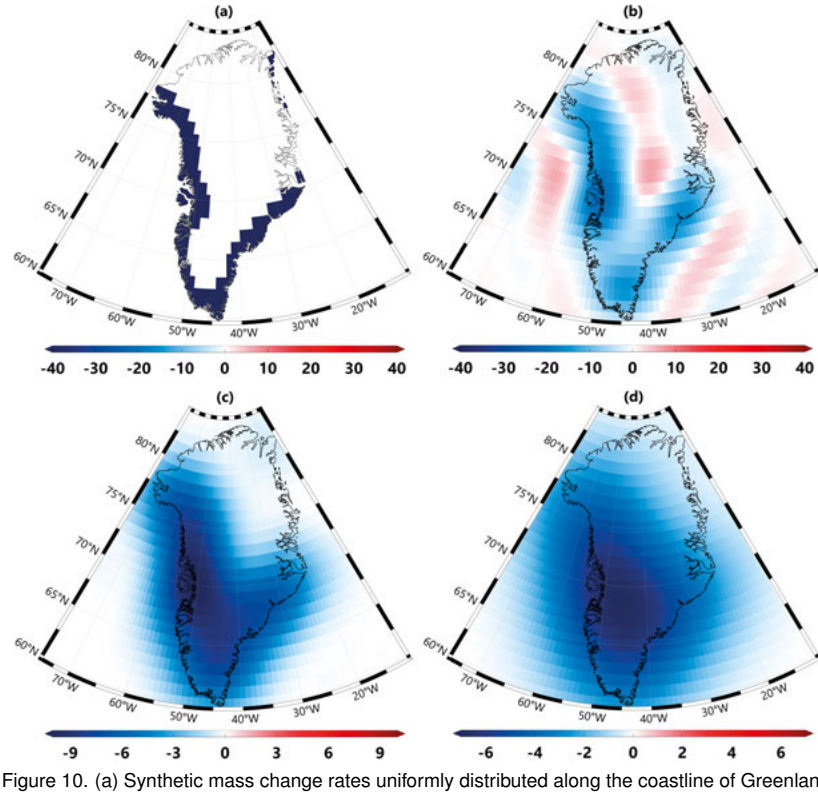

Figure 10. (a) Synthetic mass change rates uniformly distributed along the coastline of Greenland, (b) estimated mass change rates using a spherical harmonic expansion truncated at n_{max} = 60 (no filtering applied), (c) and (d) similar to (b) but with 300 and 500 km Gaussian averaging function applied, respectively. Note the different color scales for the four figures. [Units: $\mathrm{cm\,yr^{-1}}$ water equivalent]

and 500 km radius is applied to the SHCs before being converted to the mass change rates, i.e. Figures 10c and d depict the effect of both spectral truncation and filtering. It can be clearly seen that Gaussian smoothing greatly suppresses signal amplitudes and increases spatial leakage, causing synthetic data to differ significantly from the primary model, and even from the rates obtained only under the impact of truncation.

A proper leakage correction method is required to be selected as a compromise between the following inconsistent requirements: (1) mass variations inside the area are perfectly recovered, (2) mass variations outside the area do not have any effect on the regional mass change estimate, and (3) propagated errors of the GRACE(-FO) fields have a small effect on the estimate. To reduce the effect of leakage error in GRACE(-FO)-derived estimates of mass change, different methods have been introduced and employed that can be categorized according to the application for which they were proposed, e.g., for

hydrological signal leakage, for ice sheet signal leakage, and for bleeding of land signals into the ocean, or according to the source of the correction quantity, e.g., model-dependent and data-driven approaches (e.g., Klees et al., 2007; Baur et al., 2009; Horwath and Dietrich, 2009; Longuevergne et al., 2010; Landerer and Swenson, 2012; King et al., 2012; Dutt Vishwakarma et al., 2016; Vishwakarma et al., 2017; Khaki et al., 2018). For instance, Baur et al. (2009) concentrated on the Greenland ice mass variations to evaluate their proposed four-step leakage correction procedure, including a validation step based on forward modeling, which accounts for both leakage-out and leakage-in errors. In contrast to the spatial domain, a sensitivity kernel in the spectral domain was constructed by Jacob et al. (2012) that can be evaluated for various potential configurations, and finally, a configuration is used that optimizes the kernel and recovers the so-called "true" mass changes of glaciers and ice caps. Tang et al. (2012) offered a correction model for the leakage error by developing a nonlinear programming method and assuming that mass variations only occur on continents. They compared the computed and observed apparent mass variations, employed nonlinear programming for solving the ill-conditioned correction equation, and estimated the true mass changes through an iterative process. Following this study, Mu et al. (2017) employed regularization technique with the L-curve method to solve the correction equation constructed by Tang et al. (2012). Aiming at the evaluation of GRACE-derived time series of ice-sheet mass variations over Antarctic and Greenland, Groh et al. (2019) utilized independent synthetic datasets (models and observations) to estimate the total leakage error, without distinguishing between leakage-in and leakage-out. In this case, the synthetic dataset should have a spatial resolution better than what GRACE offers, and should be processed in the same way as GRACE products are (for instance, if the dataset is provided in the spatial domain, it requires to be converted into the spectral domain (with the corresponding spatial resolution) as the GRACE solutions are). In the literature, the additive technique (e.g., Klees et al., 2007; Long et al., 2014; Chen et al., 2017; Pan et al., 2017), the multiplicative method (e.g., Longuevergne et al., 2010), the scaling approach (e.g., Landerer and Swenson, 2012; Scanlon et al., 2012; Long et al., 2015), and the unconstrained forward modeling approach (e.g., Chen et al., 2015) are four popular model-dependent approaches. By criticizing model-dependent methods (in addition to the wide range of models that differ significantly from each other, in model-dependent techniques, the errors and uncertainties in the model propagate into the results), Dutt Vishwakarma et al. (2016) concentrated on hydrological signal variations over different catchments and proposed a data-driven (model-independent)

technique to account for the signal damage due to the post-processing filtering of GRACE data. In a follow-up study, Vishwakarma et al. (2017) avoided some approximations used in Dutt Vishwakarma et al. (2016), and reported that the revised strategy works efficiently even for small size catchments as well.

However, among all leakage correction techniques, forward modeling is widely used in many studies, e.g., Chen et al. (2006a), Chen et al. (2015), Wouters et al. (2008), Schrama and Wouters (2011), Bonin and Chambers (2013), Jin and Zou (2015), and Chen et al. (2009) utilized in studying polar ice-sheet mass changes, Chen et al. (2007) and Chen et al. (2013) used for mass changes of mountain glaciers, and Chen et al. (2014) employed for hydrology applications. In this contribution, forward modeling on a global scale (not at regional scales) is used to minimize the effect of land-ocean leakage error on the surface mass change estimates (e.g., Chen et al., 2013; Jin and Zou, 2015), where, comparing to forward modeling at regional scales, it can more efficiently suppress the leakage error between land and ocean signals (Chen et al., 2013). In the global forward modeling technique, a field is iteratively updated until the residual difference between the filtered field and initial field is less than a pre-defined threshold. To obtain the true GRACE(-FO) land mass changes by the global forward modeling technique, the processing steps are as follows:

1. A global regular grid $1^\circ \times 1^\circ$ of GRACE(-FO) apparent (initial trial) field is constructed after applying desired filtering and smoothing steps.
2. A layer of mass changes is uniformly assigned to the grid points of step 1 over the ocean in a way that conserves the global mass changes. In other words, by keeping mass variations over continents unchanged, the assigned mass over the ocean is negatively equal to the mean mass changes over land. The resulted field of this step is considered as the simulated true field.
3. The simulated true global field obtained from step 2 is then converted into the SHCs up to a degree and order that offers the same resolution as GRACE(-FO) fields do.
4. The same GRACE data processing steps are then applied to the achieved SHCs of the simulated field (including smoothing) to convert them into a global grid of mass variations (forward modeled field).
5. The difference between the forward modeled field and the GRACE(-FO) apparent field is computed for each grid point, and the trial field is adjusted as the reconstructed true field by adding these differences to the simulated true field. The updated trial

field is now used as the trial field in step 2, and steps 2-5 are repeated until the forward modeled field matches the GRACE(-FO) apparent field (the root mean square of difference between the forward modeled field (obtained from step 5) and the GRACE(-FO) apparent field is less than a pre-defined threshold).

Finally, the obtained reconstructed true field is considered to be almost free of the effect of the leakage error. As the same filtering steps are utilized to match forward modeled field with the GRACE(-FO) apparent field during the process, the forward modeling estimates do not, in principle, depend on the spatial filtering (Chen et al., 2013). Figure 11 graphically explains different steps of the global forward modeling technique for reducing the effect of land-ocean leakage error on a single surface mass change map of GRACE solutions

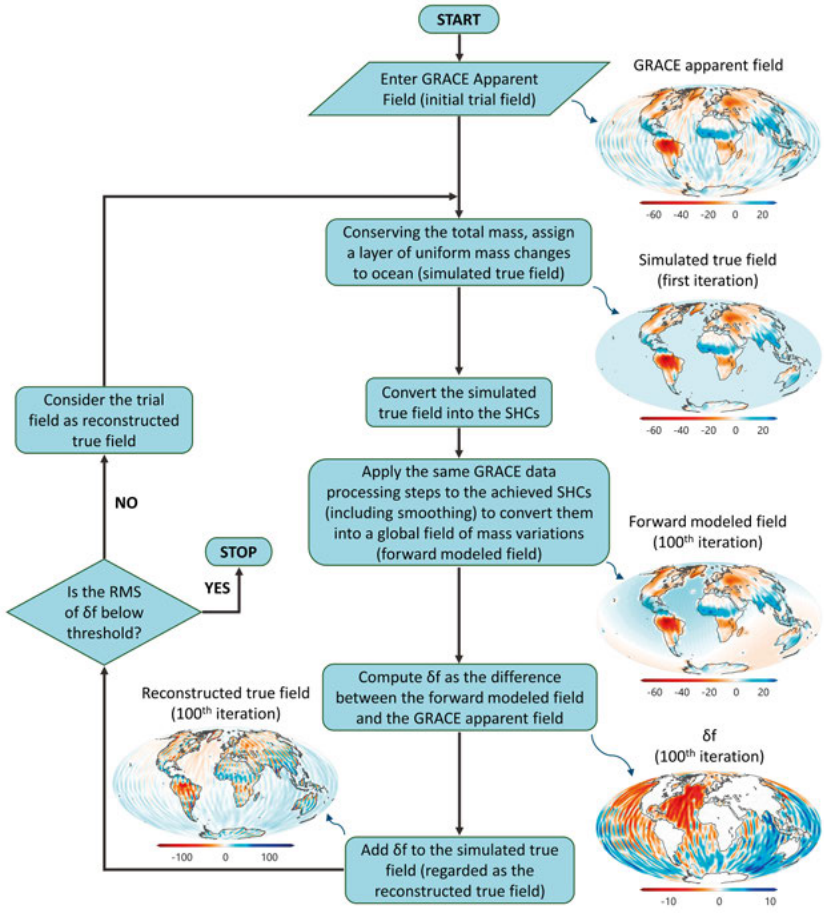

Figure 11. The global forward modeling steps for reconstructing the true mass changes of October 2010 GRACE field. [Units: cm water equivalent]

(October 2010).

In addition to the global forward modeling technique, in this study, a simple iterative procedure introduced by Chambers and Bonin (2012) is used as well, which is based on mapped data from the simulated gravity coefficients over land. According to their technique, to estimate and reduce the bleeding of land signals into the ocean, one needs first to construct a gridded map of surface mass change from GRACE(-FO) monthly solutions without applying any smoothing or destriping filter (unfiltered apparent field). Then, the ocean is simply masked out and the mass changes over continents are converted back into the SHCs. In the next step, a spatial averaging function is applied to the achieved SHCs, and the smoothed coefficients are converted to a global grid of mass variations over land and ocean. By these steps, now, one can regard the values over the ocean as the leaked signal from land, which should be subtracted from the filtered apparent field to remove the effect of leakage error.

In the context of reducing contamination of ocean data from mass change signal over the land, many studies aimed at simply excluding ocean data within certain distance from the coastal lines, referred to as ocean basin mask (kernel) approach (e.g., Chambers, 2009; Llovel et al., 2010; Johnson and Chambers, 2013; Chen et al., 2018; WCRP Global Sea Level Budget Group, 2018). However, masking out coastal zones causes not taking into account a major part of valuable grids into the computations. In this study, this technique of leakage correction is used as well.

As mentioned in the previous section, the KeFIn filtering method is utilized as well in this thesis, which first reduces correlated noise in GRACE(-FO) data and then decreases leakage effects. The approach is based on the concept of an image processing method, in which an original image f can be estimated from the observed degraded image g in spatial domain as:

$$g(x,y) = f(x,y) * d(x,y), \tag{2.35}$$

where $d(x,y)$ is degradation kernel and $*$ represents convolution operator. Since, convolution in spatial domain is similar to the multiplication in frequency domain, Eq. 2.35 can be written as:

$$G(u,v) = F(u,v) \cdot D(u,v), \tag{2.36}$$

where G, F, and D denote the Fourier transforms of the observed image g, original image f, and degradation function d, respectively, and (u,v) are spatial frequencies. By generalizing this concept to the GRACE(-FO) Total Water Storage (TWS) fields, G, F, and D represent the Fourier transforms of the noisy

TWS field g, unperturbed (ideal) TWS signal f, and a 2-D smoothing kernel d, respectively. Theoretically, if G and D are known, one could made an estimation for F using inverse filtering as $\hat{F}(u,v) = G(u,v)/D(u,v)$. However, in reality, there are two problems related to such an inverse filtering. First, D is not known precisely, and its definition needs lots of trial and error. Second, since the sinc function goes to 0 at some locations, inverse filtering fails in some cases leading to the amplification of noise in data sets. To solve the first problem, as proposed by Khaki et al. (2018), here, a motion filter is employed as the averaging kernel d (with different smoothing lengths) for reducing the correlated stripes. In addition, Wiener filtering can be utilized to solve the second problem, which estimates F as:

$$\hat{F}(u,v) = \frac{|D(u,v)|^2 \cdot G(u,v)}{|D(u,v)|^2 \cdot D(u,v) + K}, \tag{2.37}$$

where $K = P_G/P_F$ is a signal to noise ratio chosen to optimize the estimate, with P_G and P_F representing the power spectral densities of the observed field G and the original unperturbed field F, respectively. As the ideal signal is unknown, P_F can be estimated either by using a hydrological model or by trial and error (Khaki et al., 2018).

The second step of the KeFIn filtering technique includes an efficient kernel to suppress the leakage problem caused by the spatial smoothing of the previous step. Because of the low spatial resolution of GRACE(-FO) products, spatial averaging is a common technique for estimating TWS. Over the region of interest S, the regional average of field f is defined as (Dutt Vishwakarma et al., 2016):

$$f_{\mathrm{s}} = \frac{1}{A_{\mathrm{s}}} \int_S f(\theta,\lambda)\mathrm{d}\Omega, \tag{2.38}$$

where

$$A_s = \int_S \mathrm{d}\Omega \tag{2.39}$$

represents the area of S. Instead of taking the regional average directly, however, one can define a basin kernel $\Xi(\theta,\lambda)$ as:

$$\Xi(X) = \begin{cases} 1, & X \in S \\ 0, & X \notin S \end{cases}, \tag{2.40}$$

converting Eq. 2.38 to:

$$f_{\mathrm{s}} = \frac{1}{A_{\mathrm{s}}} \int_\Omega f(\theta,\lambda)\Xi(\theta,\lambda)\mathrm{d}\Omega, \tag{2.41}$$

where Ω represents the domain of the Earth's surface, $X/(\theta,\lambda)$ refer to the positions on the Earth's surface, and dΩ is the infinitesimal surface element $\sin\theta d\theta d\lambda$. By defining $\Xi^*(X)$ as the complement of the basin kernel $\Xi(X)$:

$$\Xi^*(X) = 1 - \Xi(X) = \begin{cases} 0, & X \in S \\ 1, & X \notin S \end{cases}, \tag{2.42}$$

the field f can be rewritten as the sum of signals within and outside the basin of interest, F and F^*, respectively:

$$\begin{aligned} f(\theta,\lambda) &= f(\theta,\lambda)\Xi(\theta,\lambda) + f(\theta,\lambda)\Xi^*(\theta,\lambda) \\ &= F(\theta,\lambda) + F^*(\theta,\lambda). \end{aligned} \tag{2.43}$$

Assuming that $\bar{f}$ represents the smoothed field f achieved from step 1, similarly, it can be written as the sum of smoothed signals inside (with leakage-out effects) and outside (with leakage-in effects) the region of interest:

$$\bar{f}(\theta,\lambda) = \bar{F}(\theta,\lambda) + \bar{F}^*(\theta,\lambda). \tag{2.44}$$

By limiting the analysis to the region of interest, Eq. 2.44 can be written as:

$$\bar{f}(\theta,\lambda)\Xi(\theta,\lambda) = \bar{F}(\theta,\lambda)\Xi(\theta,\lambda) + \bar{F}^*(\theta,\lambda)\Xi(\theta,\lambda), \tag{2.45}$$

which equals to:

$$\bar{f}_s(\theta,\lambda) = \bar{F}_s(\theta,\lambda) + E_{leakage-in}(\theta,\lambda), \tag{2.46}$$

where the filtered field over the region $\bar{f}_s$ is the summation of the attenuated signal of F ($\bar{F}_s$) and the signal leaked into the basin due to filtering ($E_{leakage-in}$). It is shown that $F = k\bar{F}_s$, where scaling factor k can be defined as:

$$k = \frac{\int \Xi d\Omega}{\int \Xi\bar{\Xi} d\Omega}, \tag{2.47}$$

with $\bar{\Xi}$ achieved by smoothing basin kernel Ξ. Accordingly, Eq. 2.46 can be rewritten as:

$$F(\theta,\lambda) = k(\bar{f}_s(\theta,\lambda) - E_{leakage-in}(\theta,\lambda)). \tag{2.48}$$

Similarly, by confining the analysis to the outside of the region of interest, Eq. 2.44 can be written as:

$$\bar{f}(\theta,\lambda)\Xi^*(\theta,\lambda) = \bar{F}(\theta,\lambda)\Xi^*(\theta,\lambda) + \bar{F}^*(\theta,\lambda)\Xi^*(\theta,\lambda), \tag{2.49}$$

or

$$\bar{f}_{1-s}(\theta,\lambda) = \bar{F}^{*}_{1-s}(\theta,\lambda) + E_{leakage-out}(\theta,\lambda). \tag{2.50}$$

By developing a mask filter, Khaki et al. (2018) could account for both leakage-in and leakage-out effects and, consequently, estimated F and F^{*}. The idea is that the mask filter should maximize signals concentrated in various basins while reducing their impacts on the surrounding signals. Accordingly, over a certain basin, considering the leakage-in error, the mask filter holds values outside the region of interest with a certain concentration on strong anomalies. On the contrary, for the leakage-out effect, the mask filter contains values within the region again with a focus on strong anomalies. The following steps summarize the procedure of defining a mask filter and estimating leakage-in and leakage-out errors (Khaki et al., 2018):

1. As a measure of the spatial variability of signal, $\widetilde{f}$ is computed from the smoothed field $\bar{f}$ as:

$$\widetilde{f} = \left(\frac{(\bar{f} - \min(\bar{f}))}{(\max(\bar{f}) - \min(\bar{f}))} \right), \tag{2.51}$$

   referred to as the normalized $\bar{f}$.

2. An intensity matrix is defined as follows to identify strong anomalies:

$$I = \begin{cases} 1, & \widetilde{f} > \xi \\ 0, & \tilde{f} < \xi \end{cases}, \tag{2.52}$$

   where the threshold ξ is a value between 0 and 1 (it can be defined as the median of $\widetilde{f}$).

3. A high pass filter, e.g., the Laplacian filter ($\nabla^2\Theta(X) = \sum_{i=1}^{n} \frac{\partial^2\Theta}{\partial x_i^2}$, with Θ defining a function of vector X, for instance an image in 2-D, and $X = (x_1, x_2, ..., x_n)$), is applied to the predefined intensity matrix I to highlight regions of rapid intensity change (intensifying strong anomalies while decreasing their impacts on surrounding anomalies):

$$L = \frac{1}{\sin\theta} \frac{\partial}{\partial\theta} \left(\sin\theta \frac{\partial I}{\partial\theta} \right) + \frac{1}{\sin^2\theta} \frac{\partial^2 I}{\partial\lambda^2}. \tag{2.53}$$

4. The filtered I, i.e. L, is further smoothed (to reduce high-frequency errors due to the Gibbs phenomenon) using an isotropic or anisotropic filter. Here, the conventional Gaussian

spatial smoothing function is used:

$$\bar{L} = \int W\left(\theta,\lambda,\theta',\lambda'\right) L\left(\theta',\lambda'\right) d\Omega'. \tag{2.54}$$

5. The mask filter ϑ is estimated as $\vartheta\left(\theta,\lambda\right) = 1 + \bar{L}\left(\theta,\lambda\right)$.
6. The calculated mask filter ϑ is then converted to its spherical harmonic coefficients as:

$$\left\{ \begin{array}{c} \vartheta^c_{nm} \\ \vartheta^s_{nm} \end{array} \right\} = \int_{\Omega} \vartheta(\theta,\lambda) \bar{P}_{nm}(\cos\theta) \left\{ \begin{array}{c} \cos m\lambda \\ \sin m\lambda \end{array} \right\} d\Omega, \tag{2.55}$$

where ϑ^c_{nm} and ϑ^s_{nm} describe $\vartheta\left(\theta,\lambda\right)$ as:

$$\vartheta(\theta,\lambda) = \frac{1}{4\pi} \sum_{n=0}^{\infty} \sum_{m=0}^{n} \bar{P}_{nm}(\cos\theta) \left\{ \vartheta^c_{nm} \cos m\lambda + \vartheta^s_{nm} \sin m\lambda \right\}. \tag{2.56}$$

7. The achieved kernel ϑ is then multiplied by the smoothed signal as:

$$\Upsilon(\theta,\lambda) = \bar{f}(\theta,\lambda) \odot \vartheta(\theta,\lambda), \tag{2.57}$$

with the operator $\odot$ performing a component-wise multiplication.
8. Finally, leakage-in and leakage-out effects can be estimates as:

$$E_{leakage-in} = \frac{\Xi(\theta,\lambda)}{4\pi} \int W\left(\theta,\lambda,\theta',\lambda'\right) \Xi^*\left(\theta',\lambda'\right) \Upsilon\left(\theta',\lambda'\right) d\Omega', \tag{2.58}$$

$$E_{leakage-out} = \frac{\Xi^*(\theta,\lambda)}{4\pi} \int W\left(\theta,\lambda,\theta',\lambda'\right) \Xi\left(\theta',\lambda'\right) \Upsilon\left(\theta',\lambda'\right) d\Omega'. \tag{2.59}$$

It is worth noting that the smoothing can be performed by employing the same smoothing process as the first step or by applying a Gaussian filter as above. As can be seen from the above equations, to compute the leakage-in error, one needs to only take into account Υ outside the region of interest and use smoothing to compute the leakage signal pulled inside. Similarly, to estimate the leakage-out effect, one needs to only consider signal within the region of interest.

Using $E_{leakage-in}$ and $E_{leakage-out}$, one can compute F and F^* from Eqs. 2.48 and 2.50.

2.2.3.4 High-Frequency Oceanic and Atmospheric Non-Tidal Mass Variations

GRACE(-FO) senses all sources of mass variations in the vicinity of the Earth's surface. Among all, GRACE(-FO) range-rate variations are required to be corrected for the effect of well-recognized high-frequency signals such as solid Earth and ocean tides. However, in addition to the tidal signals, there are also significant oceanic and atmospheric non-tidal mass variations with periods less than 30 days that are required to be taken into account within the processing of GRACE(-FO) data. The effect of such high-frequency signals is reduced by using "background" models (Bettadpur, 2007). Failure to account for such short-term (sub-daily to monthly) signals within the gravity field retrieval process leads to temporal aliasing of those signals into the monthly-mean gravity fields, ending in misinterpretation of estimated surface mass variations (Han et al., 2004; Dobslaw et al., 2017). However, as the model-based apriori information of mass variations used to correct the range-rate observations are imperfect, new GRACE(-FO) data releases are computed regularly to take advantage of improvements in background models.

In the context of removing high-frequency signals, tidal models are utilized to reduce the effect of ocean and Earth tides. However, in the case of non-tidal high-frequency signals, apriori information about temporal changes in the Earth's gravity field due to atmospheric and oceanic mass variability is provided under the Atmosphere and Ocean De-Aliasing Level-1B (AOD1B) products. In other words, AOD1B provides fully-normalized Stokes coefficients of the temporal variations in the Earth's gravity field caused by the non-tidal atmospheric and oceanic mass variability estimated from background models. OBP data from an unconstrained simulation with the ocean general circulation model MPIOM (Max-Planck-Institute Ocean Model), which is frequently forced with ECMWF (European Centre for Medium-Range Weather Forecasts) atmospheric data, and also forecast data from the operational Numerical Weather Prediction (NWP) model from ECMWF are different products underpinning the latest version of AOD1B (Release 06) (Dobslaw et al., 2017).

AOD1B non-tidal product comprises four individual sets of coefficients:

1. The impact of the atmosphere provided as ATM coefficients including the contribution of atmospheric surface pressure within the land, the static contribution of atmospheric pressure to OBP, and the contribution of upper-air density anomalies above both land and oceans. The monthly-averages of ATM coefficients are typically presented along with the GRACE(-FO) Level-2 solutions termed as GAA products.

2. The contribution of the dynamic ocean to OBP is provided as OCN coefficients, where GAB products are the monthly-means of these coefficients that are normally given along with the Level-2 solutions.
3. The GLO coefficients as the sum of ATM and OCN products. In this frame, the monthly-means of the GLO coefficients are presented along with the Level-2 fields as so-called GAC products.
4. The OBA coefficients that are zero over land and provide the simulated OBP that includes air and water contributions elsewhere. The monthly-means of this group of coefficients are typically provided along with the Level-2 gravity fields as GAD solutions.

Different sets of coefficients are applied for different applications. For instance, for precise orbit determination studies, it is recommended to apply GLO coefficients, or for sea-level studies, it is recommended to re-add GAD coefficients to the GRACE Level-2 gravity fields (Dobslaw et al., 2017).

2.2.3.5 Glacial Isostatic Adjustment

As has been mentioned in the previous section, GRACE(-FO) responds to all sources of mass redistribution near the Earth's surface. However, besides correcting range-rate observations for high-frequency signals, to estimate surface mass variations within land and ocean (e.g., ice sheets and glaciers mass, sea-level change, and hydrologic contents) from GRACE(-FO)-derived observations, the gravity effects of Glacial Isostatic Adjustment (GIA) signal needs to be taken into account and removed. The Earth responds to changes of the load on its surface, and GIA describes the Earth's delayed viscoelastic response to the retreat and re-advance (growth and decay) of ice sheets under the last glacial maximum (Peltier, 2004). The latest global deglaciation cycle began 21,000 years ago and was essentially complete about 4000 years ago (Huang, 2013, p. 4). However, the Earth is still under redistribution of mass on its surface due to this deglaciation (for instance with a rate of about 10 $\mathrm{mm\,yr^{-1}}$ in the northern hemisphere, e.g., Lidberg et al. (2010)). This continuing variation is due to the delayed viscoelastic response of the solid Earth seeking to gain a new equilibrium state. In other words, due to the very high mantle viscosity, the gravity field of the Earth is still gradually recovering from the load of ice that was disappeared after deglaciation.

Based on the GIA models, the effect of the ongoing GIA process can be simply corrected as a linear trend (it can be considered as linear over the relatively short period of the GRACE and GRACE-FO missions). There exist a number of regional and global GIA models, e.g., IJ05_R2 (Ivins et al., 2013)

and W12a (Whitehouse et al., 2012) regional ice histories for Antarctica, Huy3 (Lecavalier et al., 2014) and GNET-GIA (Khan et al., 2016) for Greenland, ICE-7G_NA (VM7; Roy and Peltier, 2017, 2018) over North America, NKG2016GIA (Vestøl et al., 2019) over Fennoscandia, and A13 (Wahr and Zhong, 2013), Paulson07 (Paulson et al., 2007), Caron-2018 (Caron et al., 2018), and ICE-6G_C/D (VM5a; Peltier et al., 2015; Richard Peltier et al., 2018) over a global scale. Major discrepancies between GIA models are mainly attributed to the assumptions on ice loading and melting history, the spatial distribution of ice, differences in the parameters (e.g., viscosity differences) in the Earth models, and computational strategies (Spada et al., 2011).

The continuous GIA process makes contemporary crustal uplift/subsidence mainly close to the center of the last glacial maximum ice sheets. Within the ice age, the enormous load of ice sheets caused the surface of the Earth's crust to depress. This deformation forced the mantle to flow away from the loading center to the neighboring area. Gradually, the melting of ice and disappearing of weight caused the mantle to flow back leading to land uplift over the deglaciated area and land subsidence over the surrounding region. In this context, the GRACE(-FO)-derived surface mass change estimates can be corrected for the effect of GIA using the model-based water equivalent land uplift. Figure 12 shows the regional distribution of the contemporary land uplift rates from GIA as predicted by the ICE6G-D model.

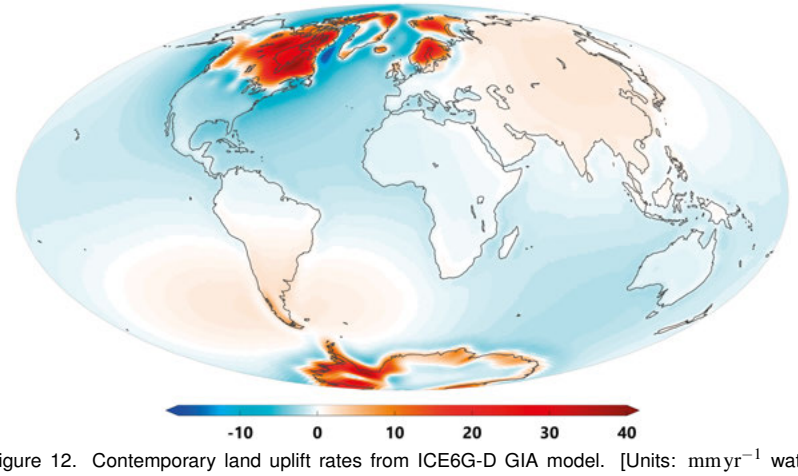

Figure 12. Contemporary land uplift rates from ICE6G-D GIA model. [Units: $\mathrm{mm\,yr^{-1}}$ water equivalent]

2.2.4 Data Gaps within GRACE and GRACE-FO Products and the Intermission Gap between Missions

The time series of monthly GRACE solutions experiences some temporal data outages during the mission period. Particularly, after 2010, due to the natural degradation of the batteries on the GRACE twin spacecrafts, within specific orbit periods through a few successive weeks (usually 4-5 weeks), inter-satellite range observations were not collected, and, therefore, no gravity solutions are estimated and provided. Figure 13 provides time information about the monthly solutions of both GRACE and GRACE-FO missions. As can be seen, for GRACE, temporal gaps happened roughly every 5-6 months after 2010. The same temporal gaps also occurred at the beginning of the GRACE-FO mission (August and September 2018). As such, many efforts were carried out to fill the gaps for the missing months of the GRACE(-FO) products, e.g., interpolation methods, such as linear interpolation, cubic spline interpolation, and least-squares fitting (e.g., Rangelova et al., 2010; Guo et al., 2018), Singular Spectrum Analysis (SSA) approaches (e.g., Zotov and Shum, 2010; Zotov, 2012; Prevost et al., 2019; Wang et al., 2020; Shen et al., 2021), using GPS-derived time-variable deformation (e.g., Rietbroek et al., 2014), and model-based approaches (e.g., Sun et al., 2019; Sahour et al., 2020).

In addition to the temporal gaps of each mission, especially the 11-month intermission gap (from July 2017 to May 2018) between the termination of GRACE and the start of GRACE-FO (Figure 13) negatively affects long-term studies of the global mass variation. Therefore, this gap requires to be reliably bridged to be able to reconstruct the continual global mass change signals. The gap-bridging methods can be classified into three different groups: (1) a continuous time series can be constructed by data-adaptive approaches using the information content within the GRACE and GRACE-FO solutions (e.g., Li et al., 2019; Wang et al., 2021; Yi and Sneeuw, 2021), (2) data-driven techniques based on other models of climatic and hydrological variables, such as precipitation and temperature, investigating on the relationship between TWS and model-based observable fields (e.g., Humphrey and Gudmundsson, 2019; Sun et al., 2019; Ahmed et al., 2019; Li et al., 2020; Sahour et al., 2020; Hasan and Tarhule, 2020), and (3) low spatial resolution temporal gravity fields from other sources, such as SLR or GPS observations to European Space Agency (ESA) Swarm satellites (e.g., Bezděk et al., 2016; Jäggi et al., 2016; Talpe et al., 2017; Lück et al., 2018), can be used to fill the gap (e.g., Forootan et al., 2020; Richter et al., 2021).

In this study, linear interpolation is used to fill the data gaps within each mission. Moreover, it is shown that since, on a continental scale, both GRACE

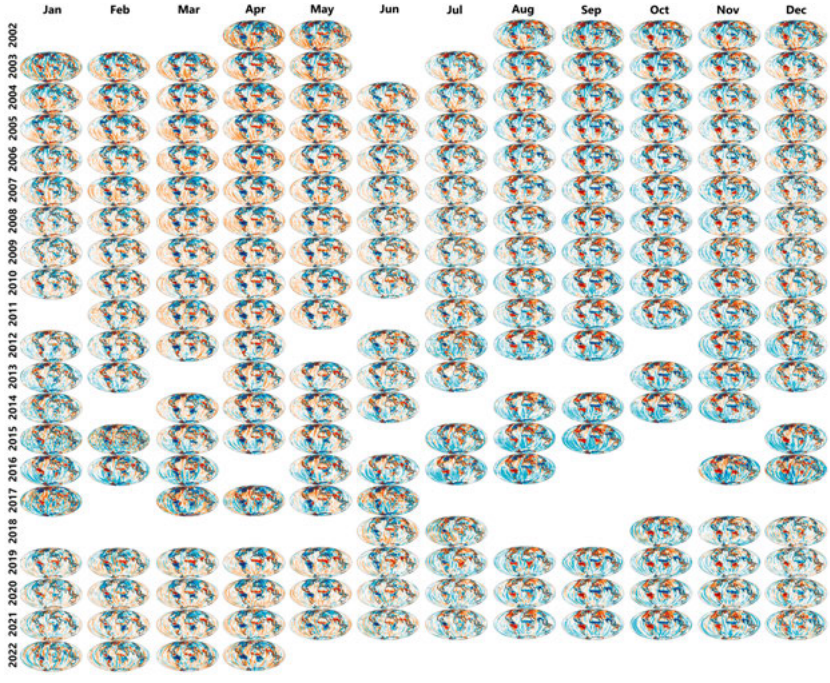

Figure 13. Time information about the monthly products of GRACE and GRACE-FO missions. GRACE-FO is still providing crucial continuity to these observations

and GRACE-FO monthly solutions are consistent across the data gap, confirming no intermission biases from GRACE to GRACE-FO, the 11-month data gap between two missions can be assuredly bridged with time series from the other model-based methods.

3 Research Methodology and Data

3.1 Joint Determination of W_0 and the MEE Parameters using Least-Squares Adjustment

In this contribution, joint estimation of W_0 and dimensions of the MEE is performed relying on the approach proposed by Sjöberg (2013), on the GGM-derived geoid heights, and on the altimetry-based MSS and MDT models. In what follows, the examined approach is summarized.

The radius vector of a point on the surface of MEE is given by:

$$r_E(\beta) = a\sqrt{1 - e^2 \sin^2 \beta}, \tag{3.1}$$

where a is the semi-major axis and e represents eccentricity of MEE, and β is the reduced latitude. In the same way, the radius vector of a point on the surface of a preliminary reference ellipsoid with geometrical parameters a_1 and e_1 is defined as $r_1(\beta) = a_1\sqrt{1 - e_1^2 \sin^2 \beta}$.

MEE is defined as the globally best-fitting ellipsoid to the geoid surface (Heiskanen and Moritz, 1967, p. 214). Accordingly, the axes are so that the global mean square of the separation between the radius vector of the geoid surface (defined as $r_1(\beta) + N$) and the radius vector $r_E(a, e, \beta)$, which should be optimized, is a minimum (Sjöberg, 2013; Sjöberg and Bagherbandi, 2017, Sec. 7.4.3):

$$J = \frac{1}{4\pi} \iint_{\Omega} [r_1(\beta) + N - r_E(a, e, \beta)]^2 \, \mathrm{d}\Omega = \min(a, e), \tag{3.2}$$

where Ω is the unit sphere. To optimize this target function, it is required to have the absolute geoid height over a global scale. Within the oceans, both satellite altimetry-based observations, along with an MDT, and a GGM can be employed to estimate the absolute geoid heights. In addition, over continents, a GGM can be used to compute the geoid heights. However, as stated in Section 2.1, GGM-derived geoid height lacks the unknown correction $-\Delta W_0/\gamma_1$. Accordingly, the target function J is augmented by the additional unknown $x = -\Delta W_0 = U_1 - W_0$. By considering that both altimetry-based and GGM-derived geoid heights, N^{alt} and N^{GGM}, respectively, are relative to the reference ellipsoid with parameters a_1, e_1, and $r_1(\beta)$, the target function J can be rewritten as:

$$I = pI_1(a, e) + (1 - p)I_2(x, a, e) + I_3(x, a, e) = \min(x, a, e), \tag{3.3}$$

with

$$
\begin{aligned}
I_1(a,e) &= \iint_{\Omega 1} \left[N^{\text{alt}} + r_1(\beta) - r_E(a,e,\beta)\right]^2 \, \mathrm{d}\Omega \\
I_2(x,a,e) &= \iint_{\Omega 1} \left[\tfrac{x}{\gamma_1} + N^{\text{GGM}} + r_1(\beta) - r_E(a,e,\beta)\right]^2 \, \mathrm{d}\Omega \\
I_3(x,a,e) &= \iint_{\Omega_2} \left[\tfrac{x}{\gamma_1} + N^{\text{GGM}} + r_1(\beta) - r_E(a,e,\beta)\right]^2 \, \mathrm{d}\Omega,
\end{aligned}
\tag{3.4}
$$

where Ω_1 and Ω_2 represent ocean- and land-covered areas of the unit sphere, respectively. $0 \leq p \leq 1$ is a weight coefficient defining the contribution of N^{GGM} and N^{alt} within marine areas in minimizing the augmented target function I. In this way, apriori variances κ_1^2 and κ_2^2 of the altimetry- and GGM-derived geoid heights, respectively, can be used for the selection of p as $p = \frac{\kappa_2^2}{\kappa_1^2+\kappa_2^2}$.

The target function presented by Eq. 3.3 is minimized by the following condition:

$$
\frac{\partial I}{\partial x} = 0, \quad \frac{\partial I}{\partial a} = 0, \quad \frac{\partial I}{\partial e} = 0. \tag{3.5}
$$

These three conditions are nonlinear in the unknowns x, a, and e. Accordingly, the target function can be minimized using an iteration procedure. In this way, the initial values for a and e, denoted A and E, respectively, can be chosen from a geodetic reference system such as GRS80, and x can be initially set to zero. Then, the radius vector of MEE can be expanded to the first order as:

$$
r_E = r_0 + r_a dA + r_e dE, \tag{3.6}
$$

where

$$
\begin{aligned}
r_0 &= A\sqrt{1 - E^2 \sin^2\beta} \\
r_a &= \left[\frac{\partial r_E}{\partial a}\right]_{e=E} = \sqrt{1 - E^2 \sin^2\beta} \\
r_e &= \left[\frac{\partial r_E}{\partial e}\right]_{\substack{a=A \\ e=E}} = -\frac{AE \sin^2\beta}{\sqrt{1 - E^2 \sin^2\beta}},
\end{aligned}
\tag{3.7}
$$

and the residual geoid height can be written as:

$$
\begin{aligned}
dR^{\text{alt}} &= r_1 + N^{\text{alt}} - r_0 \\
dR^{GGM} &= r_1 + N^{\text{GGM}} - r_0.
\end{aligned}
\tag{3.8}
$$

Accordingly, the target function Eq. 3.3 can be presented as:

$$I = pI_1(dA, dE) + (1-p)I_2(x, dA, dE) + I_3(x, dA, dE) = \min(x, dA, dE), \tag{3.9}$$

with

$$\begin{aligned} I_1 &= \iint\limits_{\Omega_1} \left[dR^{\text{alt}} - r_a dA - r_e dE\right]^2 \, \mathrm{d}\Omega \\ I_2 &= \iint\limits_{\Omega_1} \left[dR^{\text{GGM}} + \tfrac{x}{\gamma_1} - r_a dA - r_e dE\right]^2 \, \mathrm{d}\Omega \\ I_3 &= \iint\limits_{\Omega_2} \left[dR^{\text{GGM}} + \tfrac{x}{\gamma_1} - r_a dA - r_e dE\right]^2 \, \mathrm{d}\Omega. \end{aligned} \tag{3.10}$$

By equating the derivatives of I with respect to x, dA, and dE to zero, the least-squares solution for I can be achieved, leading to the following matrix system of equations:

$$\begin{pmatrix} F_{xx} & F_{xa} & F_{xe} \\ F_{xa} & F_{aa} & F_{ae} \\ F_{xe} & F_{ae} & F_{ee} \end{pmatrix} \begin{pmatrix} x \\ dA \\ dE \end{pmatrix} = \begin{pmatrix} f_x \\ f_a \\ f_e \end{pmatrix}, \tag{3.11}$$

where

$$\begin{aligned} F_{xx} &= (1-p) \iint\limits_{\Omega_1} \tfrac{\mathrm{d}\Omega}{\gamma_1^2} + \iint\limits_{\Omega_2} \tfrac{\mathrm{d}\Omega}{\gamma_1^2} \\ F_{xa} &= -(1-p) \iint\limits_{\Omega_1} \tfrac{r_a \, \mathrm{d}\Omega}{\gamma_1} - \iint\limits_{\Omega_2} \tfrac{r_a \, \mathrm{d}\Omega}{\gamma_1} \\ F_{xe} &= -(1-p) \iint\limits_{\Omega_1} \tfrac{r_e \, \mathrm{d}\Omega}{\gamma_1} - \iint\limits_{\Omega_2} \tfrac{r_e \, \mathrm{d}\Omega}{\gamma_1} \\ F_{aa} &= \iint\limits_{\Omega} r_a^2 \, \mathrm{d}\Omega \\ F_{ee} &= \iint\limits_{\Omega} r_e^2 \, \mathrm{d}\Omega \\ F_{ae} &= \iint\limits_{\Omega} r_a r_e \, \mathrm{d}\Omega, \end{aligned} \tag{3.12}$$

and

$$\begin{aligned} f_x &= -(1-p) \iint\limits_{\Omega_1} \tfrac{dR^{GGM} \, \mathrm{d}\Omega}{\gamma} - \iint\limits_{\Omega_2} \tfrac{\mathrm{d}R^{GGM} \, \mathrm{d}\Omega}{\gamma} \\ f_a &= \iint\limits_{\Omega_1} r_a \left[p dR^{alt} + (1-p) dR^{GGM}\right] \mathrm{d}\Omega + \iint\limits_{\Omega_2} r_a dR^{GGM} \, \mathrm{d}\Omega \\ f_e &= \iint\limits_{\Omega_1} r_e \left[p dR^{alt} + (1-p) dR^{GGM}\right] \mathrm{d}\Omega + \iint\limits_{\Omega_2} r_e dR^{GGM} \, \mathrm{d}\Omega. \end{aligned} \tag{3.13}$$

By solving for dA and dE, A and E are updated to the new values $A = A + dA$ and $E = E + dE$ after each iteration. Finally, after stopping the iteration, W_0 is estimated as $\hat{W}_0 = U_1 - \hat{x}$.

3.2 A New Analytical Model of Surface Mass Change Detection from Time-Variable Gravity Fields

As stated in Section 2.2.3, the issue of quantifying the Earth's surface mass change from monthly gravity fields is an inverse problem with no unique solution. In this context, the spherical approximation of this problem is well known (e.g., Wahr et al., 1998). However, ever-improving the accuracy of GRACE(-FO) time-varying gravity fields (due to the progress of both processing techniques and background models) and also longer time series of Level-2 data imply the need for calculating certain non-spherical details to higher precisions. Accordingly, in addition to the use of the common spherical approximation of the surface mass change detection problem (Wahr et al., 1998), a novel analytical solution underpinned by stronger approximations that are closer to the reality of the Earth is proposed and utilized in this study.

By modifying the assumptions of the spherical (Wahr et al., 1998) and ellipsoidal (Ghobadi-Far et al., 2019) approximations, the assumptions underpinning the new solution to the problem of surface mass change detection from the time-varying gravity fields are closer to the reality of the Earth. Accordingly, (1) the mass redistribution is concentrated in the Earth's surface, (2) the Earth's topography is not negligible, and (3) the Earth's shape is neither sphere nor ellipsoid, but it can be approximated by a regular surface. Furthermore, the other difference between the previous approximations and the new solution is that the spherical and ellipsoidal approximations are based on direct relations between the surface mass change and the variations of the harmonic coefficients, while the new solution presented in this study is based on a theorem in Potential theory investigating the behavior of a gravitational potential V at a regular surface S when the surface S contains a density distribution σ that generates the gravitational potential V (Kellogg, 1953, p. 164):

Theorem 3.1 *Let the density distribution σ on the regular surface S be continuous at the point p, then the normal derivative of the gravitational potential V approaches a limit as the point P approaches p along the normal n to S from the outside, and the limit is:*

$$\frac{\partial V}{\partial n_+} = -2\pi G\sigma(p) + \iint\limits_{S-\{p\}} G\sigma \frac{\partial}{\partial n}\frac{1}{r} dS, \tag{3.14}$$

where n_+ denotes the direction of the positive normal to S from outside, G is the universal gravitational constant, and r is the Euclidean distance between the point p and the surface element dS.

Assuming that at the target point, in which the surface mass change is about to be quantified, the Earth's surface is deferentially flat, the second term in the right-hand side of the above equation will be negligible. In this case, the limit of the normal derivative of the potential at the surface is achieved by the following relation (Kellogg, 1953):

$$\frac{\partial V}{\partial n_+} \simeq -2\pi G\sigma(p), \tag{3.15}$$

which has various applications in geodesy and geophysics, for instance, the gravity reduction corresponding to the Bouguer plate (e.g., Sjöberg and Bagherbandi, 2017, p. 107). Accordingly, density variation, $\Delta\sigma$, is achieved as:

$$\Delta\sigma \simeq -\frac{1}{2\pi G}\frac{\partial \Delta V}{\partial n_+}. \tag{3.16}$$

Moreover, the variation of the gravitational potential, ΔV, is related to the variation of the harmonic coefficients, $(\Delta C_{nm}, \Delta S_{nm})$, by the following equation (e.g., Hofmann-Wellenhof and Moritz, 2006):

$$\begin{aligned}\Delta V = \frac{GM}{R}\sum_{n=0}^{\infty}\sum_{m=0}^{n}\left(\frac{R}{r}\right)^{n+1}\left(\frac{1}{1+k_n}\right)\\ \times\left(\Delta C_{nm}\cos m\lambda + \Delta S_{nm}\sin m\lambda\right)\bar{P}_{nm}(\cos\theta).\end{aligned} \tag{3.17}$$

Accordingly, by substituting Eq. 3.17 into Eq. 3.16, and considering that $\frac{\partial \Delta V}{\partial n_+} \simeq \frac{\partial \Delta V}{\partial r}$, $M = \rho_{\text{ave}}\left(\frac{4}{3}\pi a^3\right)$, and $r = r_T(\theta,\lambda)$ represents the Earth's shape in the spherical coordinate system (r,θ,λ), an initial approximation of the surface mass change can be obtained as follows:

$$\begin{aligned}\Delta\sigma^{(0)} \simeq \frac{R\rho_{ave}}{3}\sum_{n=0}^{\infty}\sum_{m=0}^{n}\left(\frac{2n+2}{1+k_n}\right)\left(\frac{R}{r_T}\right)^{n+2}\\ \left(\Delta C_{nm}\cos m\lambda + \Delta S_{nm}\sin m\lambda\right)\bar{P}_{nm}(\cos\theta).\end{aligned} \tag{3.18}$$

Comparing this initial solution with the common spherical approximation (Wahr et al., 1998), it can be seen that the coefficients of the two models tend to each other at high degrees $(n \gg 1)$ when the shape of the Earth is considered to be a sphere, i.e. $r_T = R$. However, by containing the term $r_T(\theta,\lambda)$, which describes the Earth's topography in the spherical coordinate system, the initial model of Eq. 3.18 is able to take into account the real shape of the Earth within the process of surface mass change detection from time-variable gravity solutions.

However, due to the assumption that at the target point the Earth's surface is deferentially flat, the second term in the right-hand side of Eq. 3.14 is neglected, and, therefore, the final solution of the surface mass change detection problem needs a modification fulfilling the following equation:

$$\Delta\sigma = -\frac{1}{2\pi G}\frac{\partial \Delta V}{\partial n_+} + \mathscr{H}(\Delta\sigma), \tag{3.19}$$

where the linear operator $\mathscr{H}$ is defined by Newton's integral operator as follows:

$$\mathscr{H}(\Delta\sigma) = \frac{1}{2\pi}\iint\limits_{S-\{p\}} \Delta\sigma \frac{\partial}{\partial n}\frac{1}{r} dS, \tag{3.20}$$

with S describing the Earth's surface. Therefore, with introducing the $\mathscr{H}(\Delta\sigma)$ modification, the initial solution converts to the final solution as:

$$\Delta\sigma = \Delta\sigma^{(0)} + \mathscr{H}(\Delta\sigma). \tag{3.21}$$

Finally, according to Eq. 3.18, the final solution has the following form:

$$\begin{aligned}\Delta\sigma \simeq \frac{R\rho_{ave}}{3}\sum_{n=0}^{\infty}\sum_{m=0}^{n}\left(\frac{2n+2}{1+k_n}\right)\left(\frac{R}{r_T}\right)^{n+2} \\ \times\left(\Delta C_{nm}\cos m\lambda + \Delta S_{nm}\sin m\lambda\right)\bar{P}_{nm}(\cos\theta) + \mathscr{H}(\Delta\sigma).\end{aligned} \tag{3.22}$$

However, in this contribution, the effect of the term $\mathscr{H}(\Delta\sigma)$ is neglected and the results are based on only the core of the final solution, i.e. the initial solution. The experimental results of this study indicate how the initial model could easily surpass the common model in numerical experiments.

3.3 Other Data and Models

In this contribution, in addition to analyzing the Earth's static global gravity field, MSS, and MDT models for estimating a new value for W_0, and also monthly time-varying gravity fields of GRACE and GRACE-FO missions for detecting surface mass change, other datasets and models are used and analyzed as well mainly to validate the findings of this study. In what follows, those models and datasets are described (specific details about the models and datasets used in this study can be found in the papers).

***Satellite altimetry-based Global Mean Sea Level (GMSL)*:** Variations in the GMSL are analyzed based on the satellite altimetry products provided by various processing centers. The analyzed GMSL time series are utilized along

with the steric component of sea-level change (summarized in the next section) to validate the ocean mass change.

***Steric sea level from Argo floats*:** The steric part of the GMSL (variation of the ocean volume due to density changes defined as the combined effect of thermosteric and halosteric contributions) is quantified based on the Argo-derived observations of temperature and salinity in different ocean layers. The Argo products of different processing centers are analyzed in this study along with the altimetry-based GMSL time series to evaluate the closure of the GMSL budget.

***Hydrological models*:** Different hydrological models are analyzed to estimate and remove the disturbance factors contaminating the GRACE-based estimates of GWS. In other words, to evaluate the GWS changes, certain analysis is conducted on hydrological models to subtract the effect of surface water storage from the GRACE-based TWS. In addition, within river basins, hydrological models (global hydrological and land surface models) are utilized to be compared by the GRACE-derived surface mass changes.

***In-situ oil wells production data*:** This dataset is analyzed as in-situ observations of mass change to validate the GRACE-based GWS changes over land. The dataset provides a relatively long-period daily oil and water extraction record.

***Sentinel-1 Synthetic Aperture Radar (SAR) data*:** To detect and quantify ground surface deformation (in the form of subsidence) induced by the extraction of mass from underground sources, Sentinel-1 SAR data are analyzed.

***Surface Mass Balance (SMB) and Discharge Mass Flow (D)*:** Mass Balance (MB) is defined as the difference between SMB and D and can be directly compared to the GRACE(-FO)-based time series of ice mass change. In this study, two different models of SMB and D are utilized to validate the GRACE-derived ice mass balance results over Greenland.

***Altimetry-based Surface Elevation Change (SEC)*:** Over Antarctica, altimetry-based ice SEC time series are analyzed to evaluate the estimates of ice sheet mass balance achieved based on the GRACE monthly solutions.

4 Summary and Contribution of Papers

The research articles appended to this thesis are briefly summarized in this section, together with the different contributions made.

4.1 Paper I: A global vertical datum defined by the conventional geoid potential and the Earth ellipsoid parameters

This paper concentrates on utilizing a new method on a joint estimation of W_0 and the MEE parameters relying on the newest gravity field, mean sea surface and mean dynamic topography models. As this approach utilizes both satellite altimetry observations and a GGM model, different aspects of the input data are considered to evaluate the sensitivity of estimations to the input data. According to the achieved results, it is shown that, unlike previous studies, it is not sufficient to use only the satellite-component of a static global gravity field model to estimate W_0. In addition, a high sensitivity of the applied approach to the altimetry-based geoid heights is confirmed, i.e. mean sea surface and mean dynamic topography models. Moreover, as W_0 should be considered a quasi-stationary parameter, the effect of time-dependent Earth's gravity field changes as well as the time-dependent sea-level changes on the estimation of W_0 is quantified. Finally, computations resulted in the geoid potential $W_0 = 62636848.102 \pm 0.004$ m^2 s^{-2} and the semi-major and minor axes of the MEE, $a = 6378137.678 \pm 0.0003$ m and $b = 6356752.964 \pm 0.0005$ m, which are 0.678 and 0.650 m larger than those axes of GRS80 reference ellipsoid, respectively. Moreover, a new estimation for the geocentric gravitational constant is obtained as $GM = (398600460.55 \pm 0.03) \times 10^6$ m^3 s^{-2}.

Contribution

In 2015, the United Nations General Assembly adopted a new resolution (A/RES/69/266) entitled "A global geodetic reference frame for sustainable development". The resolution has been adopted to meet the growing demand for an accurate and stable GGRF, to improve the reliability of decision-making in an ever-increasing location-based society, with inclusive social progress, environmental sustainability, and economic development. The GGRF is essential for monitoring changes within the Earth system which includes the continents, oceans, cryosphere, and atmosphere. For instance, it is a key enabler for tracking disasters and specifying land areas with a high risk of flooding, earthquakes, and droughts, and also is essential for taking measures to

counteract these. The GGRF is fundamental for monitoring sea-level variations, ice-sheet and glacier changes, movement of tectonic plates, and land uplift so that international society can track changes to the Earth system and plan accordingly across scales from the local up to the global. It is also essential for universal timing, providing accurate positioning and navigation through satellite positioning technology, and mapping.

During the last decades, tremendous improvements in the definition and realization of the international terrestrial and celestial reference systems ensure a globally unified high-precision (at centimeter level) geometric reference frame. However, currently an equivalent high-precision global height system related to the Earth's gravity field is still missing (Sánchez et al., 2021). In 2015, the IAG released a new resolution (No. 1) defining the IHRS as the conventional gravity field-related global height system, which is a geopotential reference system co-rotating with the Earth. A major aspect of the realization of the IHRS (establishment of the International Height Reference Frame; IHRF) is the integration of the existing regional height systems into the global one referred to as vertical datum unification. To do so, all the existing regional vertical coordinates should be referred to one and the same reference surface (zero level) that is realized by a conventional W_0 (Sánchez and Sideris, 2017). In this context, the vertical coordinates of points on the surface of the Earth are provided by geopotential numbers with respect to an equipotential surface of the Earth's gravity field expressed by the conventional value W_0. Accordingly, the geoid potential, W_0, is a key parameter for the vertical datum unification and, consequently, the realization of the IHRS.

In addition to a worldwide unified vertical reference system, W_0, as a parameter of the gravity field, is required for satellite orbit determination and transformation between time scales Geocentric Coordinate Time and the Terrestrial Time, and it can be introduced as a primary parameter for the definition of a reference mean Earth ellipsoid, i.e. a level ellipsoid that best fits the geoid. By estimating W_0 based on a new method and the most recent released datasets, this study serves all the branches that have been created based on the need for geoid potential.

4.2 Paper II: Quantifying barystatic sea-level change from satellite altimetry, GRACE and Argo observations over 2005–2016

This study concentrates on different sources of uncertainty in estimating barystatic (mass-related) sea-level change using the GRACE solutions, and tries

to find the best filtering approach and leakage correction method to accurately estimate the global mean sea-level budget closure. In this study, the rate of barystatic sea-level change is quantified using GRACE monthly gravity field models and the results are compared with estimates achieved from a GMSL budget closure approach. Results confirm that the choice of decorrelation filters does not play a significant role in quantifying the global barystatic sea-level change, and spatial filtering may not be needed. Accounting for the GRACE RL05 and RL06 solutions, barystatic sea-level change trends of 2.19 ± 0.13 mm yr^{-1} and 2.25 ± 0.16 mm yr^{-1} are achieved, respectively. Accordingly, the residual trend, defined as the difference between the altimetry-derived GMSL and sum of the steric and barystatic components, amounts to 0.51 ± 0.51 and 0.45 ± 0.44 mm yr^{-1} for RL05 and RL06-based barystatic sea-level changes, respectively. The exclusion of the halosteric component results in a lower residual trend of about 0.36 ± 0.46 mm yr^{-1}, which suggests a sea-level budget closed within the uncertainty. This could be a confirmation on a high level of salinity bias particularly after 2015. Moreover, considering the assumption that the GRACE-based barystatic component includes all mass change signals, the rather large residual trend could be attributed to an additional contribution from the deep ocean, where salinity and temperature cannot be monitored by the current observing systems. The errors from various sources, including the model-based GIA signal, independent estimation of geocenter motion that are not quantified in the GRACE solutions, as well as the uncertainty of the second degree of zonal SHCs, are other possible contributors to the residual trend.

Contribution

Goal #13 of the United Nations sustainable development goals is "Take urgent action to combat climate change and its impacts". The current situation of global warming and climate change is of particular significance because most of present-day warming trend is extremely likely to be the result of human activity since the mid-20^{th} century and proceeding at a rate that is unprecedented over decades to millennia (Pachauri et al., 2014). In this regard, the global mean sea-level rise is a critical indicator of global warming and climate change. Earth-orbiting satellites and other technological advances have enabled scientists to see the big picture, collecting many different types of information about the planet and its climate on a global scale.

The better and more accurate the global mean sea-level change is estimated, the better scientists can model climate change to take proper actions in reducing the impacts. Sea-level rise represents one of the most prominent threats that climate change poses to the large human population inhabiting coastal.

Therefore, a better understanding of the current situation of sea-level rise can considerably help to more accurately project the phenomenon and estimate the rate of changes in the future, which is a key point for governments and decision-makers in sustainability issues.

In addition, sea-level rise has been long used as an indicator to monitor the Earth's energy imbalance and the associated global warming. The ocean has stored more than 90% of the increase in energy in the climate system over recent decades (Pachauri et al., 2014, p. 40), resulting in ocean thermal expansion and hence sea-level rise. Thus, the energy and sea level budgets are linked and must be consistent. Therefore, as the global sea-level change and the ocean thermal expansion can be more precisely estimated, the additional heat that has been used to warm the continents, warm and melt glacial and sea ice, and warm the atmosphere, can be accurately modeled. Consequently, right actions can be made to efficiently use the increased energy in the Earth system and/or to take proper actions to reduce disadvantageous impacts.

Sea-level rise is also of particular importance among other sciences, e.g., oceanography, marine logistics, etc. For instance, the projected global warming-induced sea-level rise has led to widespread speculation about the impact on erosion rates at the coastline as well as increasing hazard risk to coastal users. Coastal California, for example, can be found where it is undergoing the initial impacts of sea-level rise, i.e. increasing coastal erosion, periodic tidal flooding, and wider coastal flooding in the time of storms. Accordingly, sea-level studies are fundamental to the future management of the changing coastal environment. Therefore, an accurate estimation of sea-level change would be important for other applications as well.

This study concentrates on accurate estimation of the barystatic sea-level change. Therefore, findings of this study can be utilized to accurately project the global mean sea-level rise. Furthermore, considering the shortcomings of in-situ data achieved from Argo project, findings of this paper can be used, along with satellite altimetry observations, to better model ocean thermal expansion, and consequently model the Earth' energy imbalance.

4.3 Paper III: Satellite monitoring of mass changes and ground subsidence in Sudan's oil fields using GRACE and Sentinel-1 data

In this paper, groundwater storage changes over the major oil reservoirs in Sudan are studied using the GRACE monthly gravity field solutions (to study total water storage) and different hydrological models (to study surface water storage

and soil moisture). Then, concentrating on the use of different destriping and smoothing filters in analyzing GRACE monthly fields, the results are correlated with the available in-situ oil wells production data for the period of 2003–2012. In addition, using the only freely available Sentinel-1 data, collected between November 2015 and April 2019, the ground surface deformation associated with this oil and water depletion is studied. The trend of groundwater storage changes due to water and oil depletion ranged from -18.5 ± 6.3 to -6.2 ± 1.3 $\mathrm{mm\,yr^{-1}}$ using the GRACE monthly solutions and the best tested hydrological model in this study. Moreover, the Sentinel-1 SAR data analysis using the persistent scatterer interferometry method shows a high rate of subsidence, that is, -24.5 ± 0.85, -23.8 ± 0.96, -14.2 ± 0.85, and -6 ± 0.88 $\mathrm{mm\,yr^{-1}}$ over Heglig, Neem, Diffra,and Unity-area oil fields, respectively.

Contribution

In most African countries, including Sudan, there is a considerable lack of in-situ observations of groundwater storage change. Therefore, the GRACE monthly solutions along with hydrological models can be used to monitor groundwater storage changes in those regions. However, as destriping and smoothing filters play a significant role in the processing of GRACE data, and since different hydrological models result in different estimates of groundwater storage changes, it is vital to choose the best filtering approach and hydrological model so that the findings best fit the reality. To do so, groundwater storage change over a region where in-situ observations are also available can be studied, and GRACE- and hydrological-based results can be compared with in-situ data to find the best filtering strategy and hydrological model resulting in the highest correlation. In this study, concentrating on the major oil reservoirs in Sudan where in-situ oil wells production data are available, the best destriping filter and the best hydrological model are selected, which can be generalized to study the groundwater storage change in other regions where there are no in-situ data available.

Moreover, owing to the lack of terrestrial geodetic monitoring data in Sudan, the use of Sentinel-1 satellite data is very valuable to monitor extraction-induced land subsidence over the region of interest. The results of this study can help to control the integrity and safety of operations and infrastructure in that region, as well as to study the groundwater/oil storage behavior.

4.4 Paper IV: On a model of surface mass change detection from satellite gravimetry, a case study of barystatic sea-level, ice-sheet mass and basin mass changes

In this study, the common spherical model of surface mass change detection using satellite gravity data (Wahr et al., 1998) and the ellipsoidal form of the common model (Ghobadi-Far et al., 2019) are reviewed in detail, and the assumptions behind each model are considered. Although in recent years some scientists started a determined effort to make a modification to the common spherical model (Wahr et al., 1998) in order to enhance its accuracy in high-latitude regions, however, in this study, the main modification is applied to the assumptions, and it considers that the Earth's real shape and its topography are neither negligible nor simple enough to be approximated by sphere or ellipsoid. By making more reliable assumptions nearer to the reality of the Earth, some ideas of potential theory are recalled and a new model for detecting surface mass change from satellite gravimetry is proposed that carries further details about the Earth's reality.

In order to practically examine the proposed model, various numerical experiments in certain case studies in different parts of the Earth such as oceans, Greenland, Antarctica, and three major river basins (Amazon, Mississippi, and Ob), are performed and findings are compared with the results based on the previous models. These numerical experiments show how the proposed model surpasses the common model as well as its ellipsoidal version, and provides us with acceptable results over different study areas. For instance, a remarkable achievement of the numerical experiments is obtained in the case studies belonging to high-latitude regions like Greenland where the numerical experiments indicate that the proposed model is capable of improving the accuracy of the common spherical model and its ellipsoidal version in the Greenland ice sheet by 45 and 24 %, respectively.

Contribution

The Earth's mass redistribution acquired by the satellite gravimetry missions like GRACE and GRACE-FO have found various applications to geoscientific fields and particularly to climate change studies, and it is easy to discover their traces in numerous studies of the solid Earth, continental water resources, cryosphere, and oceans. As the accuracy of GRACE and GRACE-FO time-variable gravity data have significantly improved over time, and since a relatively long time series of GRACE data is available, which allows for determining seasonal and inter-annual changes with an accuracy much higher than that of individual months, therefore, a model other than the spherical and ellipsoidal models is

needed for accurately quantifying the Earth's surface mass change.

The proposed model in this study helps to quantify surface mass change with a significantly better accuracy, and can be utilized in all studies and applications in which the common spherical or the ellipsoidal models have been used to detect surface mass change using GRACE(-FO) monthly solutions. Accordingly, all the GRACE(-FO)-based surface mass change estimations can be improved and the accuracy of all the GRACE(-FO)-based assimilation products can be enhanced. Generally, it should be mentioned that the model proposed in this study opens a new window in processing time-variable gravity solutions with higher accuracy.

4.5 Paper V: Mass balance of the Greenland ice sheet and its recent contribution to sea-level rise from the GRACE and GRACE Follow-On time-variable gravity data

In this study, using the model proposed in *Paper IV* along with the GRACE and GRACE-FO monthly gravity fields, ice mass balance over Greenland is evaluated for April 2002 to December 2020. Both trend and acceleration of ice mass loss are studied over the entire Greenland Ice Sheet (GrIS) and seven individual major basins. Over the period of the GRACE mission, the eastern part of Greenland is experiencing a decreasing mass loss with time, while the mass loss increases with time along all the basins in north and west. Among all individual basins, north-west, with a rate of -74.70 ± 1.58 Gt yr^{-1}, is losing the most mass, which equals to $\sim$26.5 % of the total mass loss signal over the GrIS. To evaluate data continuity between the recently decommissioned GRACE and its successor, GRACE-FO, independent mass change estimates are utilized, as the difference between Surface Mass Balance (SMB) and Ice Discharge (D), referred to as the input–output or mass budget method. It is found that the GRACE-FO mission provides continuity for the GRACE dataset and, on a continental scale, both GRACE and GRACE-FO gravity fields are consistent across the data gap, confirming an unbiased data record from GRACE to GRACE-FO. Accordingly, as there is no intermission biases from GRACE to GRACE-FO, the 11-month data gap between two missions can be confidently bridged with time series from the mass budget method. Overall, over the period of GRACE and GRACE-FO missions till December 2020, analyzing mass balance data confirms a general, nearly constant loss across all individual regions of the GrIS, which accumulates to $\sim$5295 Gt, or -282.39 ± 9.84 Gt yr^{-1} on average, and contributes to the global mean sea-level rise of $\sim$0.8 mm yr^{-1}, equivalent to a $\sim$15 mm rise over the period of this study.

Contribution

The Earth's second-largest ice sheet, Greenland, is losing mass and is known as the greatest single contributor to the global mean sea-level rise. The recent deglaciation of Greenland is a response to both oceanic and atmospheric forcings. From 2000 to 2010, ice loss was concentrated in the south-east and north-west margins of the ice sheet, in large part due to the increasing discharge of marine-terminating outlet glaciers, emphasizing the importance of oceanic forcing (Bevis et al., 2019). However, over the period of GRACE mission, south-east is experiencing a decreasing mass loss with time, and the largest sustained ($\sim$10 years) increasing mass loss detected by GRACE occurred in west Greenland. The sustained acceleration and the subsequent, abrupt, and even stronger deceleration were mostly driven by changes in air temperature and solar radiation. Continued atmospheric warming will lead to Greenland contributing more to the global sea-level rise (Bevis et al., 2019).

The important point to remember is that ice loss is accelerating in some regions. In Greenland, the mass loss increased from 137 $\mathrm{Gt\,yr^{-1}}$ in 2002–2003 to 286 $\mathrm{Gt\,yr^{-1}}$ in 2007–2009 (Velicogna, 2009). At 2002-2003 rate, the ice sheet would take nearly 22000 years to dissipate. By 2009, this rate had more than doubled to 286 $\mathrm{Gt\,yr^{-1}}$, reducing the ice sheet lifetime to 10500 years. As the rate of ice loss increases, the ice sheet's lifetime is also diminishing. Therefore, the key question is "how will the Greenland ice sheet behave in the future?" Answering this question depends highly on our capability to accurately model the present-day ice mass loss. In addition, future projections of ice mass loss can be used to simulate and predict future sea levels. In this study, relying on the new model of surface mass change, ice mass loss trend and acceleration in different regions of Greenland are studied, which helps to better understand the behavior of the Greenland ice sheet in the future.

4.6 Paper VI: The efficiency of global hydrological and land surface models against GRACE data in quantifying land total water storage variability

In this contribution, relying on the model proposed in *Paper IV*, the performance of two common Global Hydrological Models (GHMs; produced by the hydrological community) and four prevailing Land Surface Models (LSMs; developed by the climate community) is assessed against GRACE monthly gravity solutions in estimating terrestrial TWS anomalies over twenty of the world's largest river basins. Over the period of this study (Jan 2003 - Dec 2016), the modeled and GRACE-derived time series of TWS anomalies are

decomposed into different temporal components, namely long-term, seasonal, and residual signals, in which the latter represents a summation of subseasonal water storage variability (a combination of real unmodeled seasonal and long-term signals) and the noise. In this regard, the long-term component is further decomposed into two signals, linear trend and the residual relative to this linear trend, referred to as interannual signal. However, since, among all the temporal components of TWS anomaly, seasonal cycles and long-term trends play an essential role in water resource assessment and studying variations of water storage in response to climatic and anthropic variability, therefore, this study is focused on analyzing long-term and seasonal components. Results reveal that both GHMs and LSMs underestimate GRACE-derived trends of TWS anomalies. In this context, the underestimation in basins with a rising trend is more than in those with a decreasing trend. On the contrary, the performance of global models in tracking GRACE-derived seasonal amplitudes of TWS anomalies varies with latitude, in which almost all LSMs overestimate seasonal amplitudes of GRACE-derived TWS anomalies in relatively higher latitudes, while GHMs mostly underestimate seasonal amplitudes in northern high latitudes. In tropical and mid-latitude basins, however, both GHMs and LSMs mostly underestimate seasonal amplitudes estimated by GRACE data. Overall, findings of this study confirm that global models have better performance in modeling GRACE-derived seasonal amplitudes of TWS anomalies rather than long-term trends.

Contribution

Due to their essential role in studying land TWS variations, hydrological models are intimately linked with the global water cycle, the climate system, the Earth's energy cycle, regional food and water security, human and ecosystem health, and economic and societal development. The scientific society increasingly relies on global models to evaluate how water resources are influenced by climate and humans, and to project how the situation will be in the future. Hydrological models are considered useful datasets along with other observational techniques (e.g., satellite technologies, in-situ data, and so on) to study spatiotemporal variations of water storage. For instance, global models are frequently utilized for downscaling GRACE(-FO)-derived water storage change (e.g., Yin et al., 2018; Miro and Famiglietti, 2018; Chen et al., 2019; Seyoum et al., 2019; Vishwakarma et al., 2021). Climate extremes (droughts and floods), which are influenced by land TWS changes, are other examples highlighting the importance of having reliable models. It is, therefore, crucial to assess how reliable those global models are in estimating spatiotemporal changes of water.

Relying on an accurate model of surface mass change detection from GRACE data, this study reveals deficiencies of different GHMs and LSMs and confirms that global models require significant improvements, especially in tracking long-term trends of water mass variations. As hydrologic modeling is complicated over large spatial and long temporal scales, therefore, calibrating models is an essential task (Yu, 2015). Model calibration shows that the model is able to reproduce observed values of different hydrological components. Accordingly, this study can help to calibrate global models. The results of this study can also be served for defining proper scaling factors in studies aiming at downscaling GRACE(-FO) water mass variations.

5 Conclusions and Outlook

Solid Earth's ongoing processes and mass transport within the Earth system induce variations in the gravity field of the Earth over a broad range of temporal and spatial scales. Accordingly, the Earth's gravity field and its changes reflect the spatiotemporal evolution of our planet. In this frame, among all, quantifying the static and dynamic parts of the Earth's gravity field is of great importance to fully understand the impact of climate change and global warming on the planet.

This contribution aimed at providing a deep understanding of the Earth's surface mass variations by studying its static and time-varying gravity field characteristics. More specifically, the present study was motivated by a general research question: *how the Earth's static and time-varying gravity field estimates can be improved?* To that end, under six peer-reviewed articles, different datasets and models coming from different observational techniques were analyzed, various aspects of existing data processing methods were studied, and some new techniques were examined and proposed.

5.1 Conclusion

In the context of quantifying the Earth's static and time-varying gravity field, calculating details to high precisions is a natural issue to consider once the data and their interpretation become more precise as observation progresses. Therefore, data processing strategies and analytical solutions for converting the gravity fields into meaningful functionals are of significant importance. Accordingly, the main focus of this work was on the processing methods. In what follows, the findings of the present contribution are summarized in three different categories.

5.1.1 The Geoid Potential, W_0

A new strategy that simultaneously estimates the geopotential value of the geoid and the geometrical parameters of the MEE was examined. In this regard, by considering various types of input data into the computations, different GGMs, MSS, and MDT models have been employed to quantify the dependency of estimations on the differences in the treatment of the input data. Furthermore, as both the geoid potential and the MEE dimensions are defined as time-independent parameters, the effect of the time-varying gravity field and sea-surface changes on the estimates was considered. Compared to the other common methods of estimating W_0 that include only oceans and neglect the land areas, the approach of this study takes into account both ocean and land.

The results showed that the employed technique is highly sensitive to the satellite altimetry-derived geoid heights (selection of MDT and MSS models), and, on the contrary, it was shown that the choice of the GGM does not notably affect the estimation of W_0. Moreover, unlike the previous studies in the literature, the findings of this study showed that it is not sufficient to take into account the satellite-only component of a GGM (long-wavelength components up to degree 200) to estimate W_0. The employed strategy resulted in the geoid potential $W_0 = 62636848.102 \pm 0.004$ $\mathrm{m^2\,s^{-2}}$ that is 5.3 $\mathrm{m^2\,s^{-2}}$ smaller than the value adopted by the IAG (see IAG Resolution No. 1 (2015) in Drewes et al. (2016)), and the semi-major and minor axes of the MEE, $a = 6378137.678 \pm 0.0003$ m and $b = 6356752.964 \pm 0.0005$ m, which are 0.678 and 0.650 m larger than those axes of GRS80 reference ellipsoid, respectively. Moreover, a new estimation for the geocentric gravitational constant is obtained as $GM = (398600460.55 \pm 0.03) \times 10^6$ $\mathrm{m^3\,s^{-2}}$. The differences between the estimated parameters in this contribution and those in the literature are mainly attributed to the new method employed in this study and, to a lesser extent, to the use of new models and datasets.

5.1.2 Spherical Approximation of the Surface Mass Change Detection Problem

The spherical approximation of Wahr et al. (1998) was used in this study for detecting surface mass change within both the oceans and land areas. This analytical solution was employed to convert GRACE time-varying gravity fields into the monthly maps of surface mass change. Over the oceans, a comprehensive analysis of the barystatic component of the GMSL change was carried out. It was shown that how the most recent released GRACE monthly solutions (RL06) surpass the previous released solutions (RL05) in terms of assessing the GMSL budget closure. Accordingly, the residual trend (a measure of the closure of the GMSL budget) was estimated to be 0.51 ± 0.51 and 0.45 ± 0.44 $\mathrm{mm\,yr^{-1}}$ for RL05 and RL06-based, respectively. The findings of this study showed that, over a global scale, while excluding ocean grids within 300 km from the coastal lines, applying a leakage correction has a minor impact on estimating the rate of barystatic sea-level change. However, taking the coastal water into computations, even in the case of applying a simple iterative leakage correction procedure, leads to a notably underestimated trend that is due to the residual land-ocean leakage signal. Moreover, the findings confirmed that, over the global scales, it may not be needed to apply any destriping and spatial filters to the GRACE coefficients for estimating the rate of barystatic sea-level change. On the contrary, by using different hydrological models and employing

in-situ oil wells production data along with the spherical analytical model over regional scales within continents, the results showed a high dependency of the GRACE-based GWS changes on the selection of destriping and smoothing filters.

5.1.3 Surface Mass Change Detection by a New Analytical Model

By considering the Earth's real shape rather than its simple spherical or ellipsoidal approximations (assuming that the effect of the Earth's topography on the solution is not insignificant), a new analytical solution for the problem of inferring surface mass change from time-varying gravity fields was formulated and numerically investigated. The results confirmed that the proposed model surpasses the common spherical model as well as its ellipsoidal version. In other words, by performing various practical numerical experiments in certain case studies, the findings of this study showed that the new proposed model carries further details about the Earth's reality and is able to more accurately convert monthly gravity solutions to the maps of surface mass change. It was shown that although the ellipsoidal correction considerably improves the spherical approximation (mainly in high-latitude regions with great signal size), it still underestimates the surface mass change. For instance, in the case of estimating ice-sheet mass change, the proposed approach improves the accuracy of the common spherical and ellipsoidal approximations in Greenland by $\sim$45 % and $\sim$24 %, respectively, and in Antarctica, the accuracy is improved by $\sim$19 % and $\sim$16 % for the spherical and ellipsoidal approximations, respectively. Therefore, applying the common spherical model and its ellipsoidal approximation cause irrefutable systematic errors in the estimates of surface mass change. Overall, the results of this study showed that the spherical and ellipsoidal approximations are no longer tenable for inferring accurate mass change estimates from GRACE(-FO) time-varying gravity fields.

5.2 Recommendations for Future Work

This contribution aimed to more accurately reveal and quantify large-scale processes that contribute to the Earth's gravity field change. In the end, it is believed that although the present study has improved our understanding of the Earth's surface mass variations, there is still room to enhance the accuracy of surface mass change estimations. Apart from improving the data and background models, improving the data processing strategies can lead us to more reliable results.

In this study, a new method for converting time-varying gravity fields into surface mass change was developed that could easily excel the common

spherical and ellipsoidal models. However, it is still believed that the assumptions and models presented by this research still need further studies. More specifically, a comprehensive study on the estimation of the term $\mathscr{H}(\Delta\sigma)$, discussed by Section 3.2, and how it influences the results based on the final model (Eq. 3.22) is required.

In addition, by concentrating on the nature of the GRACE(-FO) data and also the new analytical approach of converting time-varying gravity solutions to surface mass change, more research can be conducted on new filtering techniques adapted for the proposed model to enhance the accuracy effectively. Moreover, since the leakage effect is known as a major source of uncertainty in GRACE(-FO)-derived estimations considerably impacting the signal amplitude, it would be worth trying to develop a new strategy for reducing the effect of leakage error that can surpass the existing techniques, arriving at more dependable and accurate estimates of the Earth's surface mass change.

As the analytical solutions of the problem of mass change detection from gravity fields improve, a determined effort can be started on other aspects of the problem to enhance the accuracy of estimates. In this context, for instance, downscaling of the GRACE(-FO)-derived surface mass change fields can be conducted more confidently. In the end, the aforementioned improved data processing strategies (e.g., filtering and leakage correction approaches) can be employed for different mass change studies such as hydrological applications, sea-level change monitoring, and global glacier and polar ice-sheet mass change detection.

References

Adhikari, S. and Ivins, E. R. (2016). Climate-driven polar motion: 2003–2015. *Science advances*, 2(4):e1501693.

Ahmed, M., Sultan, M., Elbayoumi, T., and Tissot, P. (2019). Forecasting grace data over the african watersheds using artificial neural networks. *Remote Sensing*, 11(15):1769.

Ardalan, A. and Safari, A. (2005). Global height datum unification: a new approach in gravity potential space. *Journal of Geodesy*, 79(9):512–523.

Bandikova, T., McCullough, C., Kruizinga, G. L., Save, H., and Christophe, B. (2019). Grace accelerometer data transplant. *Advances in Space Research*, 64(3):623–644.

Baur, O., Kuhn, M., and Featherstone, W. (2009). Grace-derived ice-mass variations over greenland by accounting for leakage effects. *Journal of Geophysical Research: Solid Earth*, 114(B6).

Bettadpur, S. (2007). Level-2 gravity field product user handbook. *The GRACE Project (Jet Propulsion Laboratory, Pasadena, CA, 2003)*.

Bettadpur, S. (2012). Grace product specification document, grace 327-720. *The University of Texas at Austin*.

Bevis, M., Harig, C., Khan, S. A., Brown, A., Simons, F. J., Willis, M., Fettweis, X., Van Den Broeke, M. R., Madsen, F. B., Kendrick, E., et al. (2019). Accelerating changes in ice mass within greenland, and the ice sheet's sensitivity to atmospheric forcing. *Proceedings of the National Academy of Sciences*, 116(6):1934–1939.

Bezděk, A., Sebera, J., Teixeira da Encarnação, J., and Klokočník, J. (2016). Time-variable gravity fields derived from gps tracking of swarm. *Geophysical Journal International*, 205(3):1665–1669.

Bonin, J. and Chambers, D. (2013). Uncertainty estimates of a grace inversion modelling technique over greenland using a simulation. *Geophysical Journal International*, 194(1):212–229.

Bruns, H. (1878). Die figur der erde. *Berlin*.

Burša, M., Groten, E., Kenyon, S., Kouba, J., Raděj, K., Vatrt, V., and Vojtíšková, M. (2002a). Earth's dimension specified by geoidal geopotential. *Studia geophysica et geodaetica*, 46(1):1–8.

Burša, M., Kenyon, S., Kouba, J., Müller, A., Raděj, K., Vatrt, V., Vojtíšková, M., and Vítek, V. (1999). Long-term stability of geoidal geopotential fromtopex/poseidon satellite altimetry 1993–1999. *Earth, Moon, and Planets*, 84(3):163–176.

Burša, M., Kenyon, S., Kouba, J., Raděj, K., Vatrt, V., Vojtíšková, M., and Šimek, J. (2002b). World height system specified by geopotential at tide gauge stations. In *Vertical reference systems*, pages 291–296. Springer.

Burša, M., Kenyon, S., Kouba, J., Šíma, Z., Vatrt, V., Vítek, V., and Vojtíšková, M. (2007a). The geopotential value w 0 for specifying the relativistic atomic time scale and a global vertical reference system. *Journal of Geodesy*, 81(2):103–110.

Burša, M., Kouba, J., Raděj, K., True, S. A., Vatrt, V., and Vojtíšková, M. (1998a). Mean earth's equipotential surface from topex/poseidon altimetry. *Studia Geophysica et Geodaetica*, 42(4):459–466.

Burša, M., Kouba, J., Raděj, K., True, S. A., Vatrt, V., and Vojtíšková, M. (1998b). Monitoring geoidal potential on the basis of topex/poseidon altimeter data and egm96. In *Geodesy on the Move*, pages 352–358. Springer.

Burša, M., Raděj, K., Šima, Z., True, S. A., and Vatrt, V. (1997). Determination of the geopotential scale factor from topex/poseidon satellite altimetry. *Studia geophysica et geodaetica*, 41(3):203–216.

Burša, M., Šíma, Z., Kenyon, S., Kouba, J., Vatrt, V., and Vojtíšková, M. (2007b). Twelve years of developments: Geoidal geopotential W_0 for the establishment of a world height system–present state and future. In *Proceedings of the 1st international symposium of the international gravity field service, Harita Genel Komutanligi, Istanbul*, pages 121–123.

Burša, M., Šíma, Z., and Kostelecký, J. (1992). Determination of the geopotential scale factor from satellite altimetry. *Studia geophysica et geodaetica*, 36(2):101–108.

Caron, L., Ivins, E., Larour, E., Adhikari, S., Nilsson, J., and Blewitt, G. (2018). Gia model statistics for grace hydrology, cryosphere, and ocean science. *Geophysical Research Letters*, 45(5):2203–2212.

Chambers, D. and Bonin, J. (2012). Evaluation of release-05 grace time-variable gravity coefficients over the ocean. *Ocean Science*, 8(5):859–868.

Chambers, D. P. (2006). Observing seasonal steric sea level variations with grace and satellite altimetry. *Journal of Geophysical Research: Oceans*, 111(C3).

Chambers, D. P. (2009). Calculating trends from grace in the presence of large changes in continental ice storage and ocean mass. *Geophysical Journal International*, 176(2):415–419.

Chao, B. (2016). Caveats on the equivalent water thickness and surface mascon solutions derived from the grace satellite-observed time-variable gravity. *Journal of Geodesy*, 90(9):807–813.

Chen, J. (2019). Satellite gravimetry and mass transport in the earth system. *Geodesy and Geodynamics*, 10(5):402–415.

Chen, J., Cazenave, A., Dahle, C., Llovel, W., Panet, I., Pfeffer, J., and Moreira, L. (2022). Applications and challenges of grace and grace follow-on satellite gravimetry. *Surveys in Geophysics*, pages 1–41.

Chen, J., Li, J., Zhang, Z., and Ni, S. (2014). Long-term groundwater variations in northwest india from satellite gravity measurements. *Global and Planetary Change*, 116:130–138.

Chen, J., Tapley, B., Save, H., Tamisiea, M. E., Bettadpur, S., and Ries, J. (2018). Quantification of ocean mass change using gravity recovery and climate experiment, satellite altimeter, and argo floats observations. *Journal of Geophysical Research: Solid Earth*, 123(11):10–212.

Chen, J., Wilson, C., Blankenship, D., and Tapley, B. (2009). Accelerated antarctic ice loss from satellite gravity measurements. *Nature Geoscience*, 2(12):859–862.

Chen, J., Wilson, C., Li, J., and Zhang, Z. (2015). Reducing leakage error in grace-observed long-term ice mass change: a case study in west antarctica. *Journal of Geodesy*, 89(9):925–940.

Chen, J., Wilson, C., and Tapley, B. (2005). Interannual variability of low-degree gravitational change, 1980–2002. *Journal of Geodesy*, 78(9):535–543.

Chen, J., Wilson, C., and Tapley, B. (2006a). Satellite gravity measurements confirm accelerated melting of greenland ice sheet. *science*, 313(5795):1958–1960.

Chen, J., Wilson, C., and Tapley, B. (2013). Contribution of ice sheet and mountain glacier melt to recent sea level rise. *Nature Geoscience*, 6(7):549–552.

Chen, J., Wilson, C., Tapley, B., Blankenship, D., and Ivins, E. (2007). Patagonia icefield melting observed by gravity recovery and climate experiment (grace). *Geophysical Research Letters*, 34(22).

Chen, J., Wilson, C., Tapley, B., and Ries, J. (2004). Low degree gravitational changes from grace: validation and interpretation. *Geophysical Research Letters*, 31(22).

Chen, J., Wilson, C. R., and Seo, K.-W. (2006b). Optimized smoothing of gravity recovery and climate experiment (grace) time-variable gravity observations. *Journal of Geophysical Research: Solid Earth*, 111(B6).

Chen, L., He, Q., Liu, K., Li, J., and Jing, C. (2019). Downscaling of grace-derived groundwater storage based on the random forest model. *Remote Sensing*, 11(24):2979.

Chen, X., Long, D., Hong, Y., Zeng, C., and Yan, D. (2017). Improved modeling of snow and glacier melting by a progressive two-stage calibration strategy with grace and multisource data: How snow and glacier meltwater contributes to the runoff of the u pper b rahmaputra r iver basin? *Water Resources Research*, 53(3):2431–2466.

Cheng, M. and Ries, J. (2017). The unexpected signal in grace estimates of c_{20}. *Journal of Geodesy*, 91(8):897–914.

Cheng, M. and Tapley, B. D. (2004). Variations in the earth's oblateness during the past 28 years. *Journal of Geophysical Research: Solid Earth*, 109(B9).

Cipollini, P., Benveniste, J., Birol, F., Fernandes, M. J., Obligis, E., Passaro, M., Strub, P. T., Valladeau, G., Vignudelli, S., and Wilkin, J. (2017). Satellite altimetry in coastal regions. In *Satellite altimetry over oceans and land surfaces*, pages 343–380. CRC Press.

Ciracì, E., Velicogna, I., and Swenson, S. (2020). Continuity of the mass loss of the world's glaciers and ice caps from the grace and grace follow-on missions. *Geophysical Research Letters*, 47(9):e2019GL086926.

Crétaux, J.-F., Soudarin, L., Davidson, F. J., Gennero, M.-C., Bergé-Nguyen, M., and Cazenave, A. (2002). Seasonal and interannual geocenter motion from slr and doris measurements: Comparison with surface loading data. *Journal of geophysical research: solid earth*, 107(B12):ETG–16.

Crowley, J. W. and Huang, J. (2020). A least-squares method for estimating the correlated error of grace models. *Geophysical Journal International*, 221(3):1736–1749.

Čunderlík, R. and Mikula, K. (2009). Numerical solution of the fixed altimetry-gravimetry bvp using the direct bem formulation. In *Observing our changing Earth*, pages 229–236. Springer.

Davis, J. L., Tamisiea, M. E., Elósegui, P., Mitrovica, J., and Hill, E. M. (2008). A statistical filtering approach for gravity recovery and climate experiment (grace) gravity data. *Journal of Geophysical Research: Solid Earth*, 113(B4).

Dayoub, N., Edwards, S., and Moore, P. (2012). The gauss–listing geopotential value W_0 and its rate from altimetric mean sea level and grace. *Journal of Geodesy*, 86(9):681–694.

Ditmar, P. (2018). Conversion of time-varying stokes coefficients into mass anomalies at the earth's surface considering the earth's oblateness. *Journal of geodesy*, 92(12):1401–1412.

Dobslaw, H., Bergmann-Wolf, I., Dill, R., Poropat, L., and Flechtner, F. (2017). Product description document for aod1b release 06. *GFZ German Research Centre for Geosciences Department*, 1.

Drewes, H., Kuglitsch, F. G., Adám, J., and Rózsa, S. (2016). The geodesist's handbook 2016. *Journal of Geodesy*, 90(10):907–1205.

Dunn, C., Bertiger, W., Bar-Sever, Y., Desai, S., Haines, B., Kuang, D., Franklin, G., Harris, I., Kruizinga, G., and Meehan, T. (2003). Instrument of grace gps augments gravity measurements. *GPS world*, 14(2):16–29.

Dutt Vishwakarma, B., Devaraju, B., and Sneeuw, N. (2016). Minimizing the effects of filtering on catchment scale grace solutions. *Water Resources Research*, 52(8):5868–5890.

Farrell, W. (1972). Deformation of the earth by surface loads. *Reviews of Geophysics*, 10(3):761–797.

Forootan, E., Schumacher, M., Mehrnegar, N., Bezděk, A., Talpe, M. J., Farzaneh, S., Zhang, C., Zhang, Y., and Shum, C. (2020). An iterative ica-based reconstruction method to produce consistent time-variable total water storage fields using grace and swarm satellite data. *Remote Sensing*, 12(10):1639.

Frappart, F., Ramillien, G., Leblanc, M., Tweed, S. O., Bonnet, M.-P., and Maisongrande, P. (2011). An independent component analysis filtering approach for estimating continental hydrology in the grace gravity data. *Remote Sensing of Environment*, 115(1):187–204.

Gauss, C. F. (1828). *Bestimmung des Breitenunterschiedes zwischen den Sternwarten von Göttingen und Altona: durch Beobachtungen am Ramsdenschen Zenithsector*. Bei Vandenhoeck und Ruprecht.

Ghobadi-Far, K., Han, S.-C., Allgeyer, S., Tregoning, P., Sauber, J., Behzadpour, S., Mayer-Gürr, T., Sneeuw, N., and Okal, E. (2020). Grace gravitational measurements of tsunamis after the 2004, 2010, and 2011 great earthquakes. *Journal of Geodesy*, 94(7):1–9.

Ghobadi-Far, K., Šprlák, M., and Han, S.-C. (2019). Determination of ellipsoidal surface mass change from grace time-variable gravity data. *Geophysical Journal International*, 219(1):248–259.

Groh, A. and Horwath, M. (2021). Antarctic ice mass change products from grace/grace-fo using tailored sensitivity kernels. *Remote Sensing*, 13(9):1736.

Groh, A., Horwath, M., Horvath, A., Meister, R., Sørensen, L. S., Barletta, V. R., Forsberg, R., Wouters, B., Ditmar, P., Ran, J., et al. (2019). Evaluating grace mass change time series for the antarctic and greenland ice sheet—methods and results. *Geosciences*, 9(10):415.

Guo, J., Duan, X., and Shum, C. (2010). Non-isotropic gaussian smoothing and leakage reduction for determining mass changes over land and ocean using grace data. *Geophysical Journal International*, 181(1):290–302.

Guo, J., Li, W., Chang, X., Zhu, G., Liu, X., and Guo, B. (2018). Terrestrial water storage changes over xinjiang extracted by combining gaussian filter and multichannel singular spectrum analysis from grace. *Geophysical Journal International*, 213(1):397–407.

Han, S.-C., Jekeli, C., and Shum, C. (2004). Time-variable aliasing effects of ocean tides, atmosphere, and continental water mass on monthly mean grace gravity field. *Journal of Geophysical Research: Solid Earth*, 109(B4).

Han, S.-C., Shum, C., Jekeli, C., Kuo, C.-Y., Wilson, C., and Seo, K.-W. (2005). Non-isotropic filtering of grace temporal gravity for geophysical signal enhancement. *Geophysical Journal International*, 163(1):18–25.

Hasan, E. and Tarhule, A. (2020). Grace: Gravity recovery and climate experiment long-term trend investigation over the nile river basin: Spatial variability drivers. *Journal of Hydrology*, 586:124870.

Heiskanen, W. A. and Moritz, H. (1967). Physical geodesy(book on physical geodesy covering potential theory, gravity fields, gravimetric and astrogeodetic methods, statistical analysis, etc).

Hessler, J. (2009). Geodesy. In Kitchin, R. and Thrift, N., editors, *International Encyclopedia of Human Geography*, pages 390–393. Elsevier, Oxford.

Hofmann-Wellenhof, B. and Moritz, H. (2006). *Physical geodesy*. Springer Science & Business Media.

Horwath, M. and Dietrich, R. (2009). Signal and error in mass change inferences from grace: the case of antarctica. *Geophysical Journal International*, 177(3):849–864.

Horwath, M., Gutknecht, B. D., Cazenave, A., Palanisamy, H. K., Marti, F., Paul, F., Le Bris, R., Hogg, A. E., Otosaka, I., Shepherd, A., et al. (2022). Global sea-level budget and ocean-mass budget, with a focus on advanced data products and uncertainty characterisation. *Earth System Science Data*, 14(2):411–447.

Huang, Z. (2013). *The role of glacial isostatic adjustment (GIA) process on the determination of present-day sea-level rise*. The Ohio State University.

Humphrey, V. and Gudmundsson, L. (2019). Grace-rec: a reconstruction of climate-driven water storage changes over the last century. *Earth System Science Data*, 11(3):1153–1170.

Ihde, J., Augath, W., and Sacher, M. (2002). The vertical reference system for europe. In *Vertical Reference Systems*, pages 345–350. Springer.

Inácio, P., Ditmar, P., Klees, R., and Farahani, H. H. (2015). Analysis of star camera errors in grace data and their impact on monthly gravity field models. *Journal of Geodesy*, 89(6):551–571.

Ivins, E. R., James, T. S., Wahr, J., O. Schrama, E. J., Landerer, F. W., and Simon, K. M. (2013). Antarctic contribution to sea level rise observed by grace with improved gia correction. *Journal of Geophysical Research: Solid Earth*, 118(6):3126–3141.

Jacob, T., Wahr, J., Pfeffer, W. T., and Swenson, S. (2012). Recent contributions of glaciers and ice caps to sea level rise. *Nature*, 482(7386):514–518.

Jäggi, A., Dahle, C., Arnold, D., Bock, H., Meyer, U., Beutler, G., and Van den IJssel, J. (2016). Swarm kinematic orbits and gravity fields from 18 months of gps data. *Advances in Space Research*, 57(1):218–233.

Jekeli, C. (1981). Alternative methods to smooth the earth's gravity field. *Unknown*.

Jekeli, C. (1988). The exact transformation between ellipsoidal and spherical harmonic expansions. *Manuscripta geodaetica*, 13(2):106–113.

Jin, S. and Zou, F. (2015). Re-estimation of glacier mass loss in greenland from grace with correction of land–ocean leakage effects. *Global and Planetary Change*, 135:170–178.

Johnson, G. C. and Chambers, D. P. (2013). Ocean bottom pressure seasonal cycles and decadal trends from grace release-05: Ocean circulation implications. *Journal of Geophysical Research: Oceans*, 118(9):4228–4240.

Kellogg, O. D. (1953). *Foundations of potential theory*, volume 31. Courier Corporation.

Khaki, M., Forootan, E., Kuhn, M., Awange, J., Longuevergne, L., and Wada, Y. (2018). Efficient basin scale filtering of grace satellite products. *Remote sensing of environment*, 204:76–93.

Khan, S. A., Sasgen, I., Bevis, M., van Dam, T., Bamber, J. L., Wahr, J., Willis, M., Kjær, K. H., Wouters, B., Helm, V., et al. (2016). Geodetic measurements reveal similarities between post–last glacial maximum and present-day mass loss from the greenland ice sheet. *Science advances*, 2(9):e1600931.

King, M. A., Bingham, R. J., Moore, P., Whitehouse, P. L., Bentley, M. J., and Milne, G. A. (2012). Lower satellite-gravimetry estimates of antarctic sea-level contribution. *Nature*, 491(7425):586–589.

Klees, R., Revtova, E., Gunter, B., Ditmar, P., Oudman, E., Winsemius, H., and Savenije, H. (2008). The design of an optimal filter for monthly grace gravity models. *Geophysical Journal International*, 175(2):417–432.

Klees, R., Zapreeva, E., Winsemius, H., and Savenije, H. (2007). The bias in grace estimates of continental water storage variations. *Hydrology and Earth System Sciences*, 11(4):1227–1241.

Kornfeld, R. P., Arnold, B. W., Gross, M. A., Dahya, N. T., Klipstein, W. M., Gath, P. F., and Bettadpur, S. (2019). Grace-fo: the gravity recovery and

climate experiment follow-on mission. *Journal of Spacecraft and Rockets*, 56(3):931–951.

Kusche, J. (2007). Approximate decorrelation and non-isotropic smoothing of time-variable grace-type gravity field models. *Journal of Geodesy*, 81(11):733–749.

Kusche, J., Eicker, A., and Forootan, E. (2011). Analysis tools for grace and related data sets, theoretical basis.

Kusche, J., Schmidt, R., Petrovic, S., and Rietbroek, R. (2009). Decorrelated grace time-variable gravity solutions by gfz, and their validation using a hydrological model. *Journal of geodesy*, 83(10):903–913.

Landerer, F. W., Flechtner, F. M., Save, H., Webb, F. H., Bandikova, T., Bertiger, W. I., Bettadpur, S. V., Byun, S. H., Dahle, C., Dobslaw, H., et al. (2020). Extending the global mass change data record: Grace follow-on instrument and science data performance. *Geophysical Research Letters*, 47(12):e2020GL088306.

Landerer, F. W. and Swenson, S. (2012). Accuracy of scaled grace terrestrial water storage estimates. *Water resources research*, 48(4).

Landerer, F. W., Wiese, D. N., Bentel, K., Boening, C., and Watkins, M. M. (2015). North atlantic meridional overturning circulation variations from grace ocean bottom pressure anomalies. *Geophysical Research Letters*, 42(19):8114–8121.

Lecavalier, B. S., Milne, G. A., Simpson, M. J., Wake, L., Huybrechts, P., Tarasov, L., Kjeldsen, K. K., Funder, S., Long, A. J., Woodroffe, S., et al. (2014). A model of greenland ice sheet deglaciation constrained by observations of relative sea level and ice extent. *Quaternary Science Reviews*, 102:54–84.

Lelgemann, D. (1977). On the definition of the listing-geoid taking into consideration different height systems. *Geodesy and Physics of the Earth*, page 419.

Li, F., Kusche, J., Rietbroek, R., Wang, Z., Forootan, E., Schulze, K., and Lück, C. (2020). Comparison of data-driven techniques to reconstruct (1992–2002) and predict (2017–2018) grace-like gridded total water storage changes using climate inputs. *Water Resources Research*, 56(5):e2019WR026551.

Li, J., Chen, J., Li, Z., Wang, S.-Y., and Hu, X. (2017). Ellipsoidal correction in grace surface mass change estimation. *Journal of Geophysical Research: Solid Earth*, 122(11):9437–9460.

Li, W., Wang, W., Zhang, C., Wen, H., Zhong, Y., Zhu, Y., and Li, Z. (2019). Bridging terrestrial water storage anomaly during grace/grace-fo gap using ssa method: a case study in china. *Sensors*, 19(19):4144.

Lidberg, M., Johansson, J. M., Scherneck, H.-G., and Milne, G. A. (2010). Recent results based on continuous gps observations of the gia process in fennoscandia from bifrost. *Journal of Geodynamics*, 50(1):8–18.

Listing, J. B. (1872). *Über unsere jetzige Kenntniss der Gestalt und Grösse der Erde: Aus den Nachrichten der K. Ges. der Wiss*. Dieterich.

Llovel, W., Becker, M., Cazenave, A., Crétaux, J.-F., and Ramillien, G. (2010). Global land water storage change from grace over 2002–2009; inference on sea level. *Comptes Rendus Geoscience*, 342(3):179–188.

Long, D., Shen, Y., Sun, A., Hong, Y., Longuevergne, L., Yang, Y., Li, B., and Chen, L. (2014). Drought and flood monitoring for a large karst plateau in southwest china using extended grace data. *Remote Sensing of Environment*, 155:145–160.

Long, D., Yang, Y., Wada, Y., Hong, Y., Liang, W., Chen, Y., Yong, B., Hou, A., Wei, J., and Chen, L. (2015). Deriving scaling factors using a global hydrological model to restore grace total water storage changes for china's yangtze river basin. *Remote Sensing of Environment*, 168:177–193.

Longuevergne, L., Scanlon, B. R., and Wilson, C. R. (2010). Grace hydrological estimates for small basins: Evaluating processing approaches on the high plains aquifer, usa. *Water Resources Research*, 46(11).

Loomis, B., Rachlin, K., and Luthcke, S. (2019). Improved earth oblateness rate reveals increased ice sheet losses and mass-driven sea level rise. *Geophysical Research Letters*, 46(12):6910–6917.

Loomis, B. D., Nerem, R., and Luthcke, S. B. (2012). Simulation study of a follow-on gravity mission to grace. *Journal of Geodesy*, 86(5):319–335.

Loomis, B. D., Rachlin, K. E., Wiese, D. N., Landerer, F. W., and Luthcke, S. B. (2020). Replacing grace/grace-fo with satellite laser ranging: Impacts on antarctic ice sheet mass change. *Geophysical Research Letters*, 47(3):e2019GL085488.

Lück, C., Kusche, J., Rietbroek, R., and Löcher, A. (2018). Time-variable gravity fields and ocean mass change from 37 months of kinematic swarm orbits. *Solid Earth*, 9(2):323–339.

Meyssignac, B., Boyer, T., Zhao, Z., Hakuba, M. Z., Landerer, F. W., Stammer, D., Köhl, A., Kato, S., L'ecuyer, T., Ablain, M., et al. (2019). Measuring global ocean heat content to estimate the earth energy imbalance. *Frontiers in Marine Science*, 6:432.

Miro, M. E. and Famiglietti, J. S. (2018). Downscaling grace remote sensing datasets to high-resolution groundwater storage change maps of california's central valley. *Remote Sensing*, 10(1):143.

Moritz, H. (2000). Geodetic reference system 1980. *Journal of Geodesy*, 74(1):128–133.

Mu, D., Yan, H., Feng, W., and Peng, P. (2017). Grace leakage error correction with regularization technique: case studies in greenland and antarctica. *Geophysical Journal International*, 208(3):1775–1786.

Nesvornỳ, D. and Šíma, Z. (1994). Refinement of the geopotential scale factor r 0 on. *Earth, Moon, and Planets*, 65(1):79–88.

Pachauri, R. K., Allen, M. R., Barros, V. R., Broome, J., Cramer, W., Christ, R., Church, J. A., Clarke, L., Dahe, Q., Dasgupta, P., et al. (2014). *Climate change 2014: synthesis report. Contribution of Working Groups I, II and III to the fifth assessment report of the Intergovernmental Panel on Climate Change*. Ipcc.

Pan, Y., Zhang, C., Gong, H., Yeh, P. J.-F., Shen, Y., Guo, Y., Huang, Z., and Li, X. (2017). Detection of human-induced evapotranspiration using grace satellite observations in the haihe river basin of china. *Geophysical Research Letters*, 44(1):190–199.

Paulson, A., Zhong, S., and Wahr, J. (2007). Inference of mantle viscosity from grace and relative sea level data. *Geophysical Journal International*, 171(2):497–508.

Peidou, A. and Pagiatakis, S. (2020). Stripe mystery in grace geopotential models revealed. *Geophysical Research Letters*, 47(4):e2019GL085497.

Peltier, W. R. (2004). Global glacial isostasy and the surface of the ice-age earth: the ice-5g (vm2) model and grace. *Annu. Rev. Earth Planet. Sci.*, 32:111–149.

Peltier, W. R., Argus, D., and Drummond, R. (2015). Space geodesy constrains ice age terminal deglaciation: The global ice-6g_c (vm5a) model. *Journal of Geophysical Research: Solid Earth*, 120(1):450–487.

Poropat, L., Dobslaw, H., Zhang, L., Macrander, A., Boebel, O., and Thomas, M. (2018). Time variations in ocean bottom pressure from a few hours to many years: In situ data, numerical models, and grace satellite gravimetry. *Journal of Geophysical Research: Oceans*, 123(8):5612–5623.

Prevost, P., Chanard, K., Fleitout, L., Calais, E., Walwer, D., van Dam, T., and Ghil, M. (2019). Data-adaptive spatio-temporal filtering of grace data. *Geophysical Journal International*, 219(3):2034–2055.

Rangelova, E., Van der Wal, W., Sideris, M., and Wu, P. (2010). Spatiotemporal analysis of the grace-derived mass variations in north america by means of multi-channel singular spectrum analysis. In *Gravity, geoid and earth observation*, pages 539–546. Springer.

Rapp, R. (1995). Equatorial radius estimates from topex altimeter data. *Festschrift to E. Groten; M. Becker, G. Hein, and R. Rummel (eds.), Institute of Geodesy and Navigation, Univ. FAF, Munich*.

Rapp, R. H., Nerem, R. S., Shum, C., Klosko, S. M., and Williamson, R. G. (1991). Consideration of permanent tidal deformation in the orbit determination and data analysis for the topex/poseidon mission. *NASA Tech. Memo*, 100775.

Rateb, A., Scanlon, B. R., Pool, D. R., Sun, A., Zhang, Z., Chen, J., Clark, B., Faunt, C. C., Haugh, C. J., Hill, M., et al. (2020). Comparison of groundwater storage changes from grace satellites with monitoring and modeling of major us aquifers. *Water Resources Research*, 56(12):e2020WR027556.

Richard Peltier, W., Argus, D. F., and Drummond, R. (2018). Comment on "an assessment of the ice-6g_c (vm5a) glacial isostatic adjustment model" by purcell et al. *Journal of Geophysical Research: Solid Earth*, 123(2):2019–2028.

Richter, H. M. P., Lück, C., Klos, A., Sideris, M. G., Rangelova, E., and Kusche, J. (2021). Reconstructing grace-type time-variable gravity from the swarm satellites. *Scientific reports*, 11(1):1–14.

Rietbroek, R., Fritsche, M., Dahle, C., Brunnabend, S.-E., Behnisch, M., Kusche, J., Flechtner, F., Schröter, J., and Dietrich, R. (2014). Can gps-

derived surface loading bridge a grace mission gap? *Surveys in Geophysics*, 35(6):1267–1283.

Roy, K. and Peltier, W. (2017). Space-geodetic and water level gauge constraints on continental uplift and tilting over north america: regional convergence of the ice-6g_c (vm5a/vm6) models. *Geophysical Journal International*, 210(2):1115–1142.

Roy, K. and Peltier, W. (2018). Relative sea level in the western mediterranean basin: A regional test of the ice-7g_na (vm7) model and a constraint on late holocene antarctic deglaciation. *Quaternary Science Reviews*, 183:76–87.

Sacerdote, F. and Sanso, F. (2001). W0, a story of the height datum problem. *volume in honour of W. Torge*.

Sadeghi, M., Gao, L., Ebtehaj, A., Wigneron, J.-P., Crow, W. T., Reager, J. T., and Warrick, A. W. (2020). Retrieving global surface soil moisture from grace satellite gravity data. *Journal of Hydrology*, 584:124717.

Sahour, H., Sultan, M., Vazifedan, M., Abdelmohsen, K., Karki, S., Yellich, J. A., Gebremichael, E., Alshehri, F., and Elbayoumi, T. M. (2020). Statistical applications to downscale grace-derived terrestrial water storage data and to fill temporal gaps. *Remote Sensing*, 12(3):533.

Sanchez, L. (2007). Definition and realisation of the sirgas vertical reference system within a globally unified height system. In *Dynamic planet*, pages 638–645. Springer.

Sánchez, L. (2008). Approach for the establishment of a global vertical reference level. In *VI Hotine-Marussi Symposium on Theoretical and Computational Geodesy*, pages 119–125. Springer.

Sánchez, L. (2009). Strategy to establish a global vertical reference system. In *Geodetic reference frames*, pages 273–278. Springer.

Sánchez, L. (2012). Towards a vertical datum standardisation under the umbrella of global geodetic observing system. *Journal of Geodetic Science*, 2(4):325–342.

Sánchez, L., Ågren, J., Huang, J., Wang, Y. M., Mäkinen, J., Pail, R., Barzaghi, R., Vergos, G. S., Ahlgren, K., and Liu, Q. (2021). Strategy for the realisation of the international height reference system (ihrs). *Journal of Geodesy*, 95(3):1–33.

Sánchez, L., Čunderlík, R., Dayoub, N., Mikula, K., Minarechová, Z., Šíma, Z., Vatrt, V., and Vojtíšková, M. (2016). A conventional value for the geoid reference potential W_0. *Journal of Geodesy*, 90(9):815–835.

Sánchez, L. and Sideris, M. G. (2017). Vertical datum unification for the international height reference system (ihrs). *Geophysical Journal International*, 209(2):570–586.

Sasgen, I., Martinec, Z., and Fleming, K. (2006). Wiener optimal filtering of grace data. *Studia Geophysica et Geodaetica*, 50(4):499–508.

Save, H., Bettadpur, S., and Tapley, B. D. (2012). Reducing errors in the grace gravity solutions using regularization. *Journal of Geodesy*, 86(9):695–711.

Save, H. V. (2009). *Using regularization for error reduction in GRACE gravity estimation*. The University of Texas at Austin.

Scanlon, B. R., Longuevergne, L., and Long, D. (2012). Ground referencing grace satellite estimates of groundwater storage changes in the california central valley, usa. *Water Resources Research*, 48(4).

Schmidt, M., Fengler, M., Mayer-Gürr, T., Eicker, A., Kusche, J., Sánchez, L., and Han, S.-C. (2007). Regional gravity modeling in terms of spherical base functions. *Journal of Geodesy*, 81(1):17–38.

Schrama, E. J. and Wouters, B. (2011). Revisiting greenland ice sheet mass loss observed by grace. *Journal of Geophysical Research: Solid Earth*, 116(B2).

Schrama, E. J., Wouters, B., and Lavallée, D. A. (2007). Signal and noise in gravity recovery and climate experiment (grace) observed surface mass variations. *Journal of Geophysical Research: Solid Earth*, 112(B8).

Seo, K.-W., Kim, J.-S., Youm, K., Chen, J., and Wilson, C. R. (2021). Secular polar motion observed by grace. *Journal of Geodesy*, 95(4):1–11.

Seo, K.-W., Wilson, C. R., Chen, J., and Waliser, D. E. (2008). Grace's spatial aliasing error. *Geophysical Journal International*, 172(1):41–48.

Seyoum, W. M., Kwon, D., and Milewski, A. M. (2019). Downscaling grace twsa data into high-resolution groundwater level anomaly using machine learning-based models in a glacial aquifer system. *Remote Sensing*, 11(7):824.

Shafiei Joud, M. S., Sjöberg, L. E., and Bagherbandi, M. (2017). Use of grace data to detect the present land uplift rate in fennoscandia. *Geophysical Journal International*, 209(2):909–922.

Shen, Y., Wang, F., and Chen, Q. (2021). Weighted multichannel singular spectrum analysis for post-processing grace monthly gravity field models by considering the formal errors. *Geophysical Journal International*, 226(3):1997–2010.

Shum, C., Ries, J., and Tapley, B. (1995). The accuracy and applications of satellite altimetry. *Geophysical Journal International*, 121(2):321–336.

Sideris, M. G. (2011). Geoid determination, theory and principles. *Encyclopedia of Solid Earth Geophysics, Encyclopedia of Earth Sciences Series, Springer Science & Business Media BV*, 2011:353.

Sjöberg, L. E. (2007). The topographic bias by analytical continuation in physical geodesy. *Journal of Geodesy*, 81(5):345–350.

Sjöberg, L. E. (2013). New solutions for the geoid potential w0 and the mean earth ellipsoid dimensions. *Journal of Geodetic Science*, 3(4):258–265.

Sjöberg, L. E. and Bagherbandi, M. (2017). *Gravity inversion and integration*. Springer.

Spada, G., Barletta, V. R., Klemann, V., Riva, R., Martinec, Z., Gasperini, P., Lund, B., Wolf, D., Vermeersen, L., and King, M. (2011). A benchmark study for glacial isostatic adjustment codes. *Geophysical Journal International*, 185(1):106–132.

Sun, A. Y., Scanlon, B. R., Zhang, Z., Walling, D., Bhanja, S. N., Mukherjee, A., and Zhong, Z. (2019). Combining physically based modeling and deep learning for fusing grace satellite data: can we learn from mismatch? *Water Resources Research*, 55(2):1179–1195.

Sun, Y., Riva, R., and Ditmar, P. (2016). Optimizing estimates of annual variations and trends in geocenter motion and j2 from a combination of grace data and geophysical models. *Journal of Geophysical Research: Solid Earth*, 121(11):8352–8370.

Sun, Y. and Riva, R. E. (2020). A global semi-empirical glacial isostatic adjustment (gia) model based on gravity recovery and climate experiment (grace) data. *Earth System Dynamics*, 11(1):129–137.

Swenson, S., Chambers, D., and Wahr, J. (2008). Estimating geocenter variations from a combination of grace and ocean model output. *Journal of Geophysical Research: Solid Earth*, 113(B8).

Swenson, S. and Wahr, J. (2006). Post-processing removal of correlated errors in grace data. *Geophysical Research Letters*, 33(8).

Talpe, M. J., Nerem, R. S., Forootan, E., Schmidt, M., Lemoine, F. G., Enderlin, E. M., and Landerer, F. W. (2017). Ice mass change in greenland and antarctica between 1993 and 2013 from satellite gravity measurements. *Journal of Geodesy*, 91(11):1283–1298.

Tang, J., Cheng, H., and Liu, L. (2012). Using nonlinear programming to correct leakage and estimate mass change from grace observation and its application to antarctica. *Journal of Geophysical Research: Solid Earth*, 117(B11).

Tapley, B. D., Bettadpur, S., Ries, J. C., Thompson, P. F., and Watkins, M. M. (2004a). Grace measurements of mass variability in the earth system. *Science*, 305(5683):503–505.

Tapley, B. D., Bettadpur, S., Watkins, M., and Reigber, C. (2004b). The gravity recovery and climate experiment: Mission overview and early results. *Geophysical research letters*, 31(9).

Tapley, B. D., Watkins, M. M., Flechtner, F., Reigber, C., Bettadpur, S., Rodell, M., Sasgen, I., Famiglietti, J. S., Landerer, F. W., Chambers, D. P., et al. (2019). Contributions of grace to understanding climate change. *Nature climate change*, 9(5):358–369.

Theon, J. S. (1994). The tropical rainfall measuring mission (trmm). *Advances in Space Research*, 14(3):159–165.

Tiwari, V. and Hinderer, J. (2011). Gravity field: Time variations from surface measurements.

Torge, W. (1989). *Gravimetry*. de Gruyter.

Velicogna, I. (2009). Increasing rates of ice mass loss from the greenland and antarctic ice sheets revealed by grace. *Geophysical Research Letters*, 36(19).

Velicogna, I., Mohajerani, Y., Landerer, F., Mouginot, J., Noel, B., Rignot, E., Sutterley, T., van den Broeke, M., van Wessem, M., and Wiese, D. (2020). Continuity of ice sheet mass loss in greenland and antarctica from the grace and grace follow-on missions. *Geophysical Research Letters*, 47(8):e2020GL087291.

Velicogna, I. and Wahr, J. (2013). Time-variable gravity observations of ice sheet mass balance: Precision and limitations of the grace satellite data. *Geophysical Research Letters*, 40(12):3055–3063.

Vestøl, O., Ågren, J., Steffen, H., Kierulf, H., and Tarasov, L. (2019). Nkg2016lu: a new land uplift model for fennoscandia and the baltic region. *Journal of Geodesy*, 93(9):1759–1779.

Vishwakarma, B. D., Horwath, M., Devaraju, B., Groh, A., and Sneeuw, N. (2017). A data-driven approach for repairing the hydrological catchment signal damage due to filtering of grace products. *Water Resources Research*, 53(11):9824–9844.

Vishwakarma, B. D., Zhang, J., and Sneeuw, N. (2021). Downscaling grace total water storage change using partial least squares regression. *Scientific data*, 8(1):1–13.

Wahr, J., Molenaar, M., and Bryan, F. (1998). Time variability of the earth's gravity field: Hydrological and oceanic effects and their possible detection using grace. *Journal of Geophysical Research: Solid Earth*, 103(B12):30205–30229.

Wahr, J. and Zhong, S. (2013). Computations of the viscoelastic response of a 3-d compressible earth to surface loading: an application to glacial isostatic adjustment in antarctica and canada. *Geophysical Journal International*, 192(2):557–572.

Wang, F., Shen, Y., Chen, Q., and Wang, W. (2021). Bridging the gap between grace and grace follow-on monthly gravity field solutions using improved multichannel singular spectrum analysis. *Journal of Hydrology*, 594:125972.

Wang, F., Shen, Y., Chen, T., Chen, Q., and Li, W. (2020). Improved multichannel singular spectrum analysis for post-processing grace monthly gravity field models. *Geophysical Journal International*, 223(2):825–839.

Wang, L., Khan, S. A., Bevis, M., van den Broeke, M. R., Kaban, M. K., Thomas, M., and Chen, C. (2019). Downscaling grace predictions of the crustal response to the present-day mass changes in greenland. *Journal of Geophysical Research: Solid Earth*, 124(5):5134–5152.

Watkins, M. M., Wiese, D. N., Yuan, D.-N., Boening, C., and Landerer, F. W. (2015). Improved methods for observing earth's time variable mass distribution with grace using spherical cap mascons. *Journal of Geophysical Research: Solid Earth*, 120(4):2648–2671.

WCRP Global Sea Level Budget Group, . (2018). Global sea-level budget 1993–present. *Earth System Science Data*, 10(3):1551–1590.

Whitehouse, P. L., Bentley, M. J., and Le Brocq, A. M. (2012). A deglacial model for antarctica: geological constraints and glaciological modelling as a basis for a new model of antarctic glacial isostatic adjustment. *Quaternary Science Reviews*, 32:1–24.

Wouters, B., Chambers, D., and Schrama, E. (2008). Grace observes small-scale mass loss in greenland. *Geophysical Research Letters*, 35(20).

Wouters, B. and Schrama, E. (2007). Improved accuracy of grace gravity solutions through empirical orthogonal function filtering of spherical harmonics. *Geophysical Research Letters*, 34(23).

Yi, S. and Sneeuw, N. (2021). Filling the data gaps within grace missions using singular spectrum analysis. *Journal of Geophysical Research: Solid Earth*, page e2020JB021227.

Yin, W., Hu, L., Zhang, M., Wang, J., and Han, S.-C. (2018). Statistical downscaling of grace-derived groundwater storage using et data in the north china plain. *Journal of Geophysical Research: Atmospheres*, 123(11):5973–5987.

Yu, Z. (2015). Hydrology, floods and droughts— modeling and prediction.

Zhang, Z.-Z., Chao, B., Lu, Y., and Hsu, H.-T. (2009). An effective filtering for grace time-variable gravity: Fan filter. *Geophysical Research Letters*, 36(17).

Zhao, M., Velicogna, I., and Kimball, J. S. (2017). A global gridded dataset of grace drought severity index for 2002–14: comparison with pdsi and spei and a case study of the australia millennium drought. *Journal of Hydrometeorology*, 18(8):2117–2129.

Zotov, L. (2012). Application of multichannel singular spectrum analysis to geophysical fields and astronomical images. *Advances in Astronomy and Space Physics*, (2, Iss. 1):82–84.

Zotov, L. and Shum, C. (2010). Multichannel singular spectrum analysis of the gravity field data from grace satellites. In *AIP Conference Proceedings*, volume 1206, pages 473–479. American Institute of Physics.

Zwally, H. J., Schutz, B., Abdalati, W., Abshire, J., Bentley, C., Brenner, A., Bufton, J., Dezio, J., Hancock, D., Harding, D., et al. (2002). Icesat's laser measurements of polar ice, atmosphere, ocean, and land. *Journal of Geodynamics*, 34(3-4):405–445.

Papers
Associated papers have been removed in the electronic version of this thesis.
For more details about the papers see:
http://urn:nbn:se:hig:diva-39412